Investigating the Unimolecular Breakdown Products and Pyrolysis Products of Short Chain Per/Polyfluorinated Compounds

Angela Radnoff

Thesis submitted to the University of Ottawa in partial fulfillment of the requirements for the Master's degree in Chemistry

Department of Chemistry and Bimolecular Sciences

Faculty of Science

University of Ottawa

© Angela Radnoff, Ottawa, Canada, 2026

Abstract

PFAS or per/polyfluoroalkyl substances are synthetic compounds used in a variety of different products such as in clothing, firefighting foam, and non-stick cookware. PFAS are able to be used in such a variety of products due to their hydrophilic and hydrophobic nature as well as their stability. The strong C−F bond found in PFAS makes them resistant to degradation and thus persistent in the environment. PFAS have therefore been found in soil, atmosphere, ground water, surface water, and wastewater etc. Most industries are turning away from using long chain PFAS since they are starting to be banned in multiple countries. Instead, though short-chain PFAS which are not as researched are being used as replacements. The goal of my research was to determine how PFAS break down using collision induced dissociation (CID) mass spectrometry and pyrolysis.

PFAS have been quantified and detected using tandem mass spectrometry in multiple studies from various matrices. The dissociation of short chain PFAS ions using mass spectrometry has not been explored. In order to do this, negative ion mode triple quadrupole mass spectrometry was used to breakdown five short chain PFAS, 2,2,3,3,3-pentafluoropropionic acid (**1**, m/z 163), 3,3,3-trifluoropropionic acid (**2** m/z 127), 2,2,3,3,3-pentafluoro-1-propanol (**3**, m/z 149), 3,3,3-trifluoro-1-propanol (**4**, m/z 113), and trifluoromethanesulfonic acid (**5**, m/z 149) using CID. Once the products were obtained, density functional theory (DFT), and RRKM kinetic calculations were used to analyse the reactions energetics and rates. **1** loses CO_2 at low lab-frame collision energy. **2** also loses CO_2 to form the 1,1,1-trifluoroethane ion (m/z 83) and 1,2-difluoroethylene to form FCO_2^- (m/z 63). RRKM calculations for the two reactions show that m/z 83 has a higher entropy of activation driving its formation. **3** undergoes the loss of CH_2O to form the pentafluoroethyl

anion (m/z 119) and the loss of HF to form $CF_2CF_2COH^-$ (m/z 129). **4** produced four fragment ions with two primary reactions making CF_3CHCH^- (m/z 95) + H_2O and $CF_2CHCOH_2^-$ (m/z 93) + HF, which go on to dissociate further to produce CF_3^- (m/z 69) + HCCH + H_2O and CF_2CH^- (m/z 63) + CH_2O + HF. At low collision energy, m/z 95 dominates due to a lower energy transition state, but as internal energy increases, m/z 93 takes over as its transition state has a more favourable entropy. **5** produced FSO_3^- (m/z 99), SO_3^- (m/z 80), and CF_3^- (m/z 69). SO_3^- was the most abundant fragment due to its higher electron affinity.

One method of removing PFAS from the environment is by burning them at very high temperatures. The problem with this method is that incomplete degradation occurs, and smaller and persistent fluorinated compounds are left over. To investigate this, a Chen-type microreactor was used as well as imaging photoelectron photoion coincidence spectroscopy to explore the pyrolysis of three short-chain PFCs, 2,2,3,3,3-pentafluoropropionic acid (**1**), 3,3,3-trifluoropropionic acid (**2**), and 2,2,3,3,3-pentafluoro-1-propanol (**3**). The products were ionized with VUV synchrotron radiation at the Swiss Light Source and identified by their mass-selected threshold photoelectron spectra (ms-TPES). The results are compared to literature photoelectron spectra and calculated TPES from Franck-Condon simulations performed at the B3LYP/6-311+G(d,p) level of theory. Thermal degradation leads off with CO_2 loss (**1**,**2**), HF loss (**1,2,3)** and formaldehyde loss (**3**). These result in fluoroethanes, which themselves decompose to form fluoroethenes, and subsequently CF_2. There was evidence for bimolecular processes that form formaldehyde from **1** and **2**, and acetylene from **3**.

Acknowledgements

I would like to thank my partner, friends, and family for their constant support during my studies. My undergraduate and graduate studies taught me resilience, determination, and most importantly how to relax and have fun. I want to give a special thanks to my boyfriend Michael for his constant support, love, and always believing in me when I did not. I want to thank my friends Raquel, Audrey, and Mady for their constant support throughout my studies as well as their kindness and just being awesome friends. I also want to thank my sister Freda for being there for me and always making me laugh. I can't forget about my awesome lab mates, thank you for the guidance and the laughs, you made the lab feel like a fun and positive space. I also want to thank Paul for his support, guidance, and wisdom. Lastly, I want to thank my parents for their support.

I want to dedicate this work to my nonna, grandma, and grandpa who always believed in me but couldn't make it to my graduation. I love you always.

TOC

List of Figures

Table of Abbreviations

Abbreviations	Definition
AC	Activated carbon
ANO	Atomic Natural Orbital
APCI	Atmospheric pressure chemical ionization
cc	Correlation consistent
CI	Chemical ionization
CID	Collision induced dissociation
DBDI-MS	Dielectric barrier discharge ionization mass spectrometry
DFT	Density functional theory
DLLME	Dispersive liquid-liquid microextraction
DSPE	Dispersive solid-phase extraction
E_0	Activation energy
EI	Electron ionization
E_{int}	Internal energy of the ion
E_{neu}	Energy of the neutral
EO	Electrochemical activation
ESI	Electrospray ionization
FTICR-MS	Fourier transform ion cyclotron resonance
FTOH	Fluorotelomer alcohol
GAC	Granular activated carbon
GC	Gas chromatography
h	Planck's constant
HF	Hartree-Fock
HILIC	Hydrophilic interaction chromatography ion exchange column
HPLC	High performance liquid chromatography
HPLC	High-performance liquid chromatography
HRMS	High resolution mass spectrometry
HS-SPME	Headspace SPME
hv	Photon energy

IE_a	Adiabatic ionization energy
IPE	Ion-pair extraction
iPEPICO	Imaging photoelectron photoion coincidence spectroscopy
k(E)	Rate for a unimolecular reaction
E	Energy
K_b	Boltzmann constant
KE_e	Kinetic energy of the electron
LC	Liquid chromatography
LLE	Liquid-liquid extraction
LOD	Limit of detection
MALDI-IMS	Matrix-assisted desorption/ionization imaging mass spectrometry
MERP	Minimum energy reaction pathway
MRM	Multiple reaction monitoring
MRM	Multiple reaction monitoring
MS/MS	Tandem mass spectrometry
ms-TPES	Mass selected threshold photoelectron spectrum
$N^{\ddagger}(E-E_0)$	Sum of states
NCI	Negative ion chemical ionization
NTP	Non-thermal plasma
PAP	Polyfluoroalkyl phosphoric acids
PFAA	Perfluoroalkyl acids
PFAS	Perfluorooctanoic acid
PFBA	Perfluorobutanoic acid
PFBA	Perfluorobutanoic acid
PFBS	Perfluorobutane sulfonic acid
PFC	Per- and polyfluorinated compounds
PFECAs	Perfluoroalkyl ether carboxylic acids
PFOS	Perfluorooctane sulphonic acid
PFPeA	Perfluoropentanoic acid
PFPrA	Perfluoropropionic acid

PLE	Pressurized liquid extraction
PPARα	Peroxisome proliferator-activated receptor-α
Q	Total partition function
QTOF	Quadrupole time of flight
RF	Radio frequency voltage
RO	Reverse osmosis
RRK	Rice-Ramsperger-Kassel
RRKM	Rice-Ramsperger-Kassel-Marcus
sccm	Centimetres per minute
SIM	Selected ion monitoring mode
SLS	Swiss light source synchrotron
SPE	Solid phase extraction
SPME	Solid-phase microextraction
T	Temperature
TFA	Trifluoroacetic acid
TFAN	Trifluoroacetic anhydride
TOF-MS	Time of flight mass spectrometry
TQ	Triple quadruple
U	Average internal energy
UPLC	Ultra-performance liquid chromatography
WAX	Weak anion exchange columns
$\Delta S^{\ddagger}$	Entropy of activation
ρ(E)	Density of states
σ	Reaction degeneracy

Chapter 1: PFAS and their detection and analysis

1.1. What are PFAS?

1.1.1. What are PFAS and why are they important?

PFAS, also known as per/polyfluoroalkyl substances, are a class of man-made chemicals that have been used in industrial applications and consumer products. This is due to their hydrophobic and hydrophilic properties, as well as their amazing stability. Common PFAS include PFOA (perfluorooctanoic acid) and PFOS (perfluorooctane sulphonic acid) and have been largely studied (Figure 1). PFAS have been used in many products, including non-stick cookware, food packaging, and water-resistant clothes. Since PFAS are very stable, they are resistant to degradation, which has led to their persistence in the environment. PFAS not only persist in the environment but can also bioaccumulate, which can impact the health of ecosystems and humans. Long term exposure to PFAS has been shown to cause liver damage, immune suppression, thyroid disorders, and even cancer. PFAS precursors can also have harmful effects, and these compounds include fluorotelomer alcohols (FTOHs) and polyfluoroalkyl phosphoric acids (PAPs). PFAS exposure can come from a variety of sources such as inhaling indoor air and wastewater sludge. Government regulations are focused on detecting PFAS in various environments and by trying to reduce the amount being released into the environment.[1]

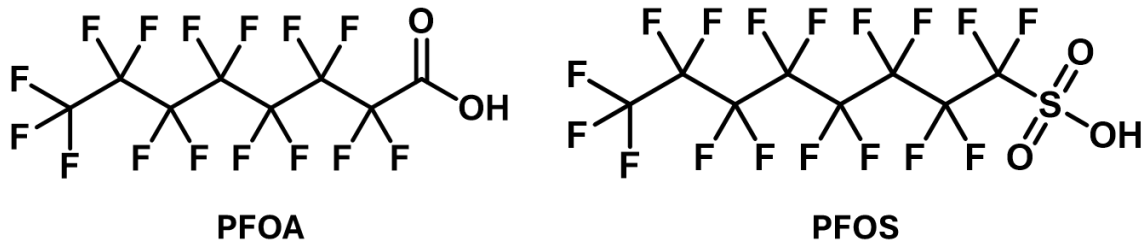

Figure 1: Chemical structures of PFOA and PFOS.

1.1.2 The properties of PFAS.

PFAS contain a carbon backbone saturated with fluorine and a functional group at the end. This structure allows them to be hydrophobic due to the carbon fluorine chain and lipophilic due to the functional group. Long-chain PFAS are in the solid state, while short-chain PFAS (4-6 carbons) are liquid at room temperature. PFAS melting points and boiling points increase when the carbon fluorine chain increases, and their solubility decreases in water with increased salt content. Short-chain PFAS have a higher vapour pressure and are therefore more volatile. PFAS can also aggregate in groundwater at low concentrations due to reacting with granules. All of this means that PFAS can transport through water, air, and soil to cause persistent contamination.[2]

1.1.3 PFAS toxicity.

PFAS have been reported in the blood of a large percentage of the populations of industrialized nations. This is due to their widespread use, and PFAS are mostly found in environmental matrices such as water systems. Studies were conducted that showed how PFAS can transport from soil to plants and leachate, which included long and short-chain PFAS. PFAS are present in the food chain, which is the result of biomagnification due to their low excretion rate from organisms. PFAS can enter organisms through dermal exposure, inhalation, and ingestion (Figure 2). PFAS have been shown to cause reproductive issues, low birth weight, immunotoxicity, and kidney problems (Figure 3).[2]

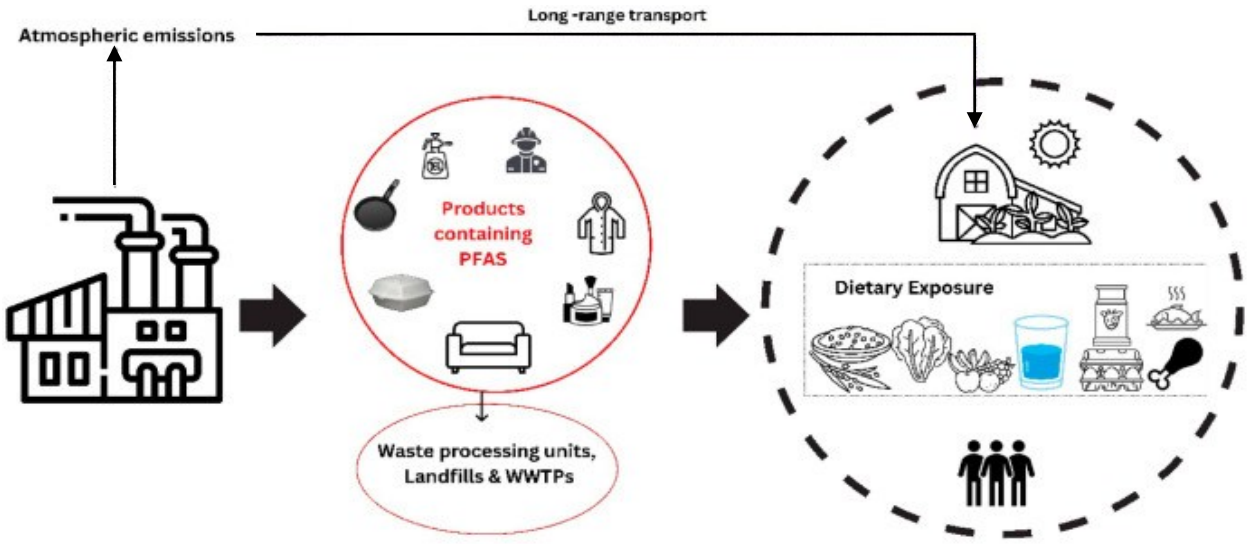

Figure 2: How humans are exposed to PFAS by transportation and emission. Reprinted with permission from Singh et al.[3]

PFAS are mostly absorbed through the gastrointestinal tract and are found in the liver, kidneys, and serum due to their binding affinity for hepatic proteins and albumin. Longer chain PFAS have a higher binding affinity, which makes it harder for the body to eliminate through urine or feces. In addition, their elimination depends on many factors, including the animal species, chemical, sex, and half-life. One of the mechanisms of toxicity that PFAS have in the body includes activation of peroxisome proliferator-activated receptor-α (PPARα), which is a nuclear receptor involved in liver toxicity. This nuclear receptor helps to regulate lipid metabolism, differentiation, and cell growth. When exposed to PFAS, the PPARα pathway changes due to gene expression also changing. For example, in rodents exposed to PFAS, it has caused increased cholesterol in the liver and liver enlargement. PPARα is also found in human embryos as well as rodents, so activation can lead to smaller birth weights, reduced survival, and delayed eye opening. PFAS have been shown to decrease immune function by suppressing B-cells and plasma cells. In addition, PFAS have also been shown to affect the thyroid, but results remain inconclusive. In humans, studies

have shown links to hypothyroidism, but others have linked PFAS exposure to hyperthyroidism, and some show no effect at all. Most of these studies are done with animals exposed to a high concentration of PFAS; in addition, the type of PFAS and the magnitude of exposure need to be considered. In order to diagnose PFAS-linked conditions, local PFAS contamination in the area should be determined, since the first-line treatment is to reduce potential sources of exposure.[4]

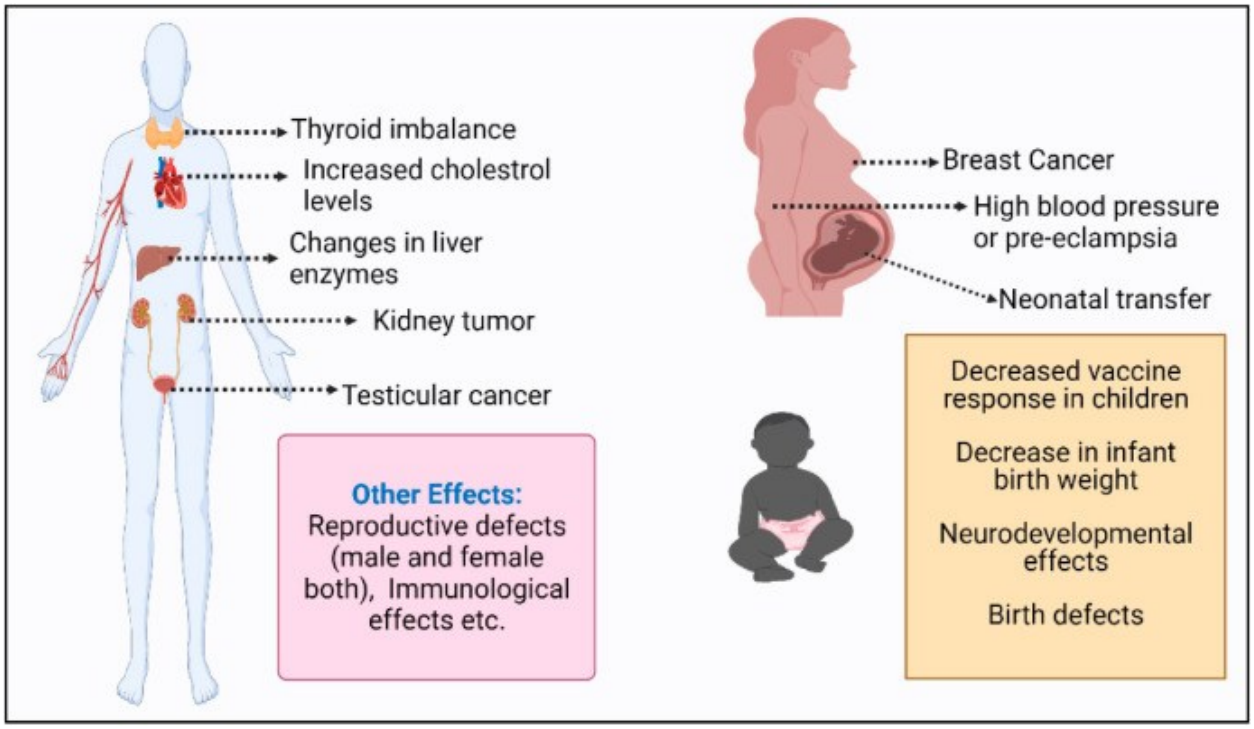

Figure 3: Negative health affects associated with PFAS exposure. Reprinted with permission from Singh et al.[3]

1.1.4 How PFAS are transported and distributed.

PFAS are very persistent in the environment because they don't degrade by hydrolysis, photolysis, or by microbes in the environment. PFAS contaminate the soil and water through a variety of methods of exposure. Firefighting foams are a common way PFAS enter the soil and water during real-life firefighting operations or fire training. Higher levels of PFAS are released

during real-life operations, but firefighting training sites can leak contaminated water and affect drinking water. PFAS can also come from industrial and domestic use and contaminate water sources. For example, fluoropolymer manufacturing facilities, electronic devices, textiles, etc. Examples in domestic use are cosmetics, fabrics, coatings, etc. Industrial effluents also pose a risk and contain higher amounts of PFAS. Wastewater treatment plants, landfills, and dumping sites are other sources of PFAS that can contaminate the soil and water. PFAS found in household waste ends up in municipal facilities and can accumulate into bio-solids. They can also end up in landfill leachate from stain-resistant coatings and consist of long and short-chain PFAS. The landfill leachate can enter groundwater systems and then travel to other environments. PFAS are also found in agricultural effluents due to their presence in crops and soil. This is because fertilizers, atmospheric decomposition, and pesticides are some sources of PFAS. Therefore, agricultural, industrial, domestic effluents, and landfill leachate end up in stormwater with mostly long-chain PFAS present. Studies have also found more short-chain PFAS present in surface water, but the longer-chain PFAS are present in sediments.[2]

Once PFAS are in the soil and water, they can stay through partitioning, sorption, and through complexation reactions. PFAS can partition through hydrophobic interactions with organic material in the soil. Sorption occurs through electrostatic interactions of organic material with charged clay particles. Complexation reactions are the process which leads to PFAS complexed to organic matter. Ultimately, the mobility of PFAS and where they end up depends on their chain length, solubility, and pH. PFAS can also migrate through dispersion, diffusion, and advection. Advection means that the PFAS molecules are being transported in a flow inside air or water that doesn’t reduce concentration. PFAS molecules are moving horizontally to transfer to different medias. Dispersion refers to the downwards or vertical flow of molecules between media. Lastly,

diffusion is the transfer of molecules to different media through a concentration gradient. Diffusion is what leads to the persistence of PFAS in the environment since PFAS can diffuse into bedrock, which can then leach into the groundwater. PFAS can also be deposited from the atmosphere and accumulate in the soil and water through sedimentation and precipitation, respectively. Once PFAS are in the soil, they can leach into surface and ground water when it rains. This then leads to plants absorbing PFAS. Due to the hydrophobic and hydrophilic nature of PFAS, it can affect their surface properties and how they are transported. The hydrophobic C-F tail faces the atmosphere while their hydrophilic head group is dissolved in the water, which results in films that are visible in the water. Therefore, PFAS can accumulate on the surface of water. Some PFAS, like PFAA (perfluoroalkyl acids), can also aggregate in water with their hydrophilic portions pointing outwards and their hydrophobic portions pointing inwards, allowing them to be adsorbed.[2]

Ground water contaminated with PFAS is another method in which PFAS can be distributed into surface water and contaminate drinking water and crops through irrigation. Humans and other animals or plants can then be exposed to PFAS through drinking the water or ingesting the wildlife grown in contaminated waters. PFAAs are in their anionic form and remain in surface waters due to their low pKa, decreased volatility and low sorption coefficients. These PFAS can travel from surface water to groundwater through groundwater recharge and end up later in oceans and can then be distributed globally.[2] All of this demonstrates how much PFAS have permeated into different parts of our ecosystems due to their chemical properties and widespread use.

1.1.5 How PFAS can be removed.

PFAS can be removed in a variety of ways through non-destructive and destructive methods. Examples of non-destructive methods include adsorption using activated carbon,

filtration, and ion exchange resins. These methods don't destroy PFAS and instead separate them, which leads to secondary disposal methods being required. Examples of destructive methods include plasma-based oxidation, ultrasonication, electrochemical treatment, and incineration. Some of these oxidation methods can lead to 100% defluorination but introduces other chemicals in the aquatic environment. There are some challenges, though to remove PFAS from the environment, which include cost and the need for real-time monitoring.[1]

The current preferred method to remove PFAS from water is adsorption since its very effective. PFAS can be absorbed by hydrogen bonding, hydrophobic interactions, and electrostatic interactions. Adsorbents can be modified depending on the types of PFAS that need to be removed. For example, PFAS are generally negatively charged and are attracted to positively charged adsorbents. PFAS are also very electronegative due to their carbon fluorine backbone, and they are also hydrophilic due to their headgroups. Therefore, activated carbon, biochar, and nanoparticle adsorbents can be used to remove PFAS. Activated carbon (AC) is a very good adsorbent for PFAS because of its high specific surface area. AC works by adsorbing PFAS using hydrophobic interactions since the AC is nonpolar and PFAS have a nonpolar backbone structure. Biochar is an adsorbent that can be used to remove PFAS and comes from heating biomass in low-oxygen conditions. Using biochar is more cost-effective than AC, it has better adsorption and is largely available. Using nanomaterials as adsorbents is another method to remove PFAS from the environment due to their increased surface area. One of the mechanisms in which PFAS are adsorbed onto these nanoadsorbents is hydrophobic interactions, since their fluorine carbon backbone is hydrophobic. PFAS are also negatively charged due to the electronegativity of the fluorine group and the negatively charged headgroup, and are attracted to positively charged

nanoparticles. Other ways nanoadsorbents attract PFAS are hydrogen bonding and ion exchange processes.[2]

Filtration is another PFAS removal strategy that is a non-destructive way to remove PFAS from water. Some examples of filtration methods include nano-filtration, reverse osmosis, and membrane filtration. Membrane filtration is common method to remove PFAS since it uses pore size and zeta potential to efficiently remove them. Other contaminants in the water, including salts, organic matter, and co-contaminants, do not hinder the selectivity of these membranes. Different kinds of membranes include porous and dense and can be used to efficiently remove PFAS. Porous membranes can't remove small PFAS but have a high pore strength and can be used in ultrafiltration or microfiltration. Dense membranes can be used in reverse osmosis as well as nanofiltration. Nanofiltration is a method that uses a membrane with very small pore sizes in the range of 0.5-2 nm at 5-40 bar to filter water. PFAS can be removed using this method due size exclusion, electrostatic repulsion, and PFAS affinity to the membrane. The final method of filtration is reverse osmosis (RO), which has been used effectively to remove many water pollutants. This method uses high pressure to push water through a membrane with very small pore sizes and can have pressures reaching 10-100 bar. Overall, reverse osmosis has been shown to be effective in removing PFAS from water.[2]

Ion exchange resins are another non-destructive method to remove PFAS and works best to remove short-chain PFAS more effectively compared to other methods. The types of resins used include polystyrene-divinyl benzene, since it can remove about 90% of PFAS and can be regenerated with NaCl or NH_4Cl. Regenerated resins, though are not effective for longer chain PFAS. In water treatment plants, cationic or anionic polymers are used. Combining different PFAS removal methods can also be useful, for example, by using ion exchange and AC, long and short-chain

PFAS can be removed. Longer chain PFAS are primarily removed from AC while shorter chain PFAS are removed mostly by ion exchange. A disadvantage to this method is that due to the high flux of PFAS, shorter-chain PFAS are not removed as efficiently, and the AC becomes saturated with other contaminants. Nanofiltration with activated carbon and anion exchange is another combined method that removes 99% of PFAS. This method also suffers from the fact that shorter chain PFAS are not removed as efficiently compared to longer chain PFAS due to the AC and anion exchange resin selecting for more hydrophobic molecules.[2]

Plasma is a destructive PFAS technique that induces ionization of gaseous molecules by using electrically charged gas. During water treatment methods, two electrodes form an electrical discharge near the water that produces very reactive oxidative and reductive species. This process increases temperature, creates shockwaves and releases UV light (Figure 4). Instead, non-thermal plasma (NTP) can be used to remove PFAS from water and is preferred because it requires less energy at atmospheric pressure and has higher excitation selectivity. NTP is generated through corona discharge, glow discharge, spark discharge, to name a few. In this process, electrons at a high temperature are produced and are higher than the temperature of the surrounding gas. Therefore, the electrons will collide with the gas atoms to create more electrons, radicals, photons, and ions. The high-energy ions collide with the PFAS on the surface of the water bubbles. It has been found that the most effective way to remove PFAS using plasma is to generate it with argon gas as the surrounding gas. Some advantages to this technique are that it destroys PFAS very well, it requires short treatment time, co-contaminants don't affect the process, and this process can remove both short and long-chain PFAS. A disadvantage to this technique is that contaminants in the water, including organic matter and nitrates, reduce the treatment efficiency by competing with PFAS removal.[5]

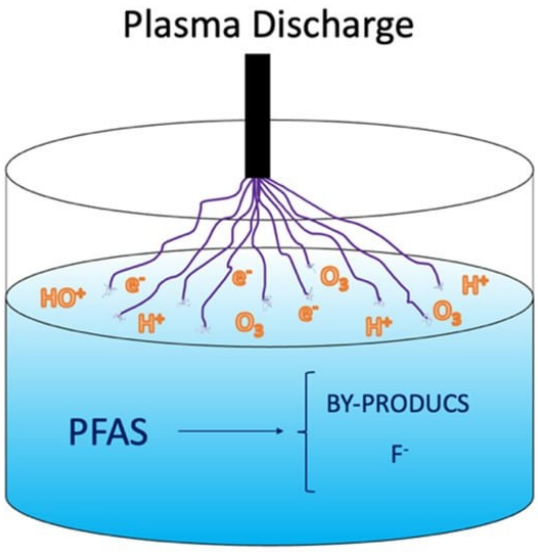

Figure 4: PFAS mineralization by non-thermal plasma reproduced from Meegoda et al.[5]

Sonolysis is another destructive method that uses an acoustic field to cause a chemical reaction in solutions by generating vapour bubbles, which then implode (Figure 5). This method can degrade organic compounds such as PFAS because it occurs at the bubble/water interface, where PFAS are adsorbed onto the surface. The bubbles collapsing is the method in which the organic compounds can pyrolyze and combust. The bubbles that burst produce very high temperatures upwards of 5000 K, and so the water vapour produces H and OH radicals, which then react and degrade organic compounds. If ultrasonic frequencies are used, PFAS degradation can be enhanced, but using a combination of frequencies can also enhance it as well. The advantages of using this method are that it's very effective in PFAS degradation, it can be used to degrade PFAS in soil, and the contaminants in landfill leachate doesn't impact degradation. Therefore, this method causes complete defluorination without any additional chemicals and has a low environmental impact. The disadvantages of this method are that it requires high energy consumption, its high cost, and that these experiments were conducted without field-level concentrations.[5]

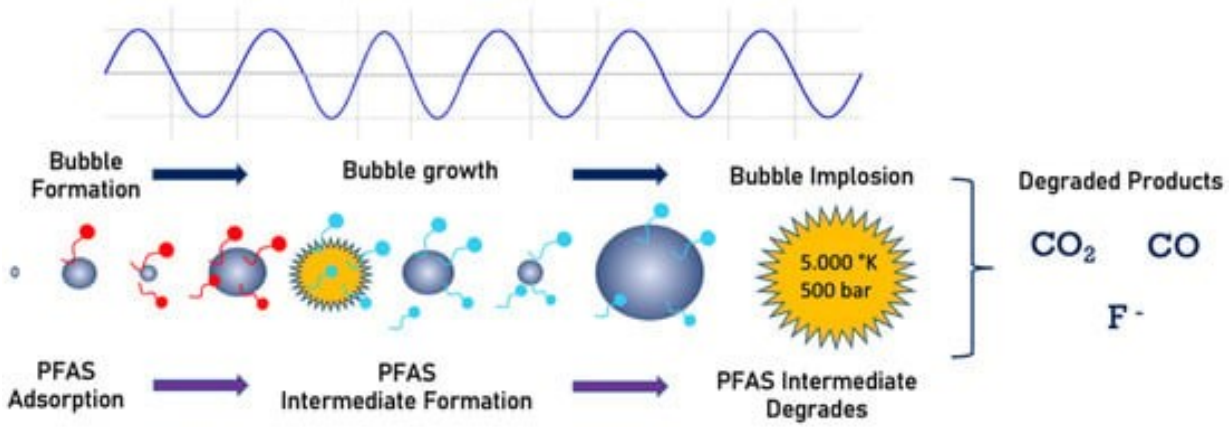

Figure 5: How PFAS are mineralized by sonolysis reproduced from Meegoda et al.[5]

Electrochemical oxidation (EO) is a destructive technique that uses an electric current to oxidize and reduce organic pollutants. An anode and cathode are placed in a conductive solution, which creates the current so that the pollutants are adsorbed and then degraded at the electrode or in the solution (Figure 6). Through an oxidation reaction, electrons transfer from the PFAS to the anode, and this is a direct reaction. The indirect mechanism would be the formation of radicals that oxidize the PFAS. Longer chain PFAS degrade very well using this method, as over 99% are removed. Shorter chain PFAS, though don't degrade as well and sometimes even increase the amount of PFAS since they convert into shorter precursors. This degradation method is used mostly to treat laboratory waste compared to industrial waste, since in a real-world setting, more time and more replacement electrodes are needed to remove PFAS effectively. It has been shown that increasing electrical current densities can increase the efficiency with which PFAS are removed. In order to decrease the time and energy used, other methods can be coupled with EO, like ion exchange or filtration. The advantages of using this method are that it uses low temperatures, no harsh chemicals, lower environmental impact, it destroys PFAS completely and has been shown to effectively remove PFAS in contaminated water. Some disadvantages to this method are that it's a

challenge to scale up due to higher energy consumption and high cost. Another issue is that EO can cause dangerous chemicals produced from the reactions, such as corrosive HF gas, and toxic Cl_2 due to its presence in water.[5]

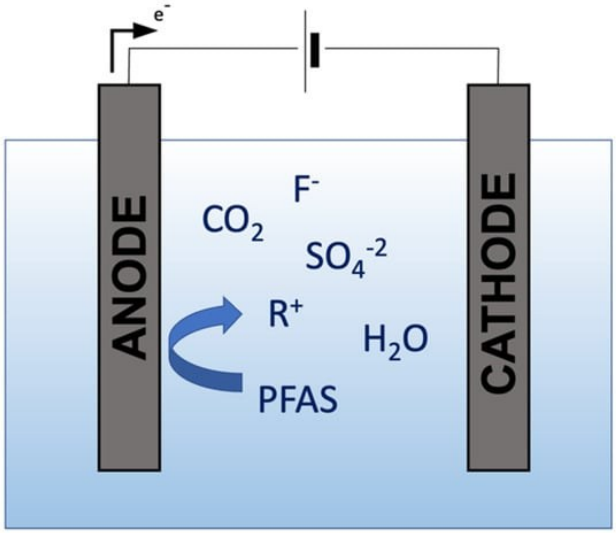

Figure 6: How PFAS are degraded by electrochemical oxidation reproduced from Meegoda et al.[5]

Another destructive PFAS removal strategy includes incineration or thermal degradation. The mechanism of decomposition varies depending on the operating conditions, which include temperature, gases, time, etc (Figure 7). When PFAS are broken down by heat, they release carbon dioxide, carbon monoxide, water, sulphur molecules, and HF. Since PFAS are very stable and resistant to degradation, they require high temperatures for long periods of time for their degradation. Incineration is a method that uses high temperatures in an oxygenated environment for their degradation. Incinerators can reach temperatures between 980-1200 ºC with most organic compounds being degraded from 590-650 ºC. PFAS, though do not degrade completely and form incomplete combustion products, including shorter chain PFAS. There is limited research into the incineration of PFAS, but it has been found that increasing the temperature decreases the amount

of PFAS but not all of the PFAS decreased over time. In fact, the air in these incinerator facilities was found to have high concentrations of PFOA. It's also a concern that the incinerator facilities are not breaking down PFAS and are instead spreading them to the soil and water around them. Incineration facilities burn PFAS-based materials and waste containing PFAS. The US defence department has banned the incineration of PFAS-based materials, and additionally, in 2022, the National Defence Authorization Act stipulates that the military can't incinerate materials with PFAS. This is due to the unknown fate of PFAS during incineration. The incineration studies didn't monitor all PFAS compounds, and the thermal degradation products of PFAS detected during incineration had limited data. This is because of the lack of a good method of emission sampling and analytical detection method for PFAS and their degradation products. The advantages of using incineration include the wide availability of incineration facilities and that they are good at breaking down PFAS. A disadvantage to this method is that bottom ash and gas are produced in this process. The ash contains the non-combusted products, which include inorganic fluorine and PFAS attached to inorganic compounds. The gas contains volatile products and tiny particles, including HF. The gas is usually removed with an electrostatic precipitator, but the tiny volatile fluoride byproducts may not be.[5]

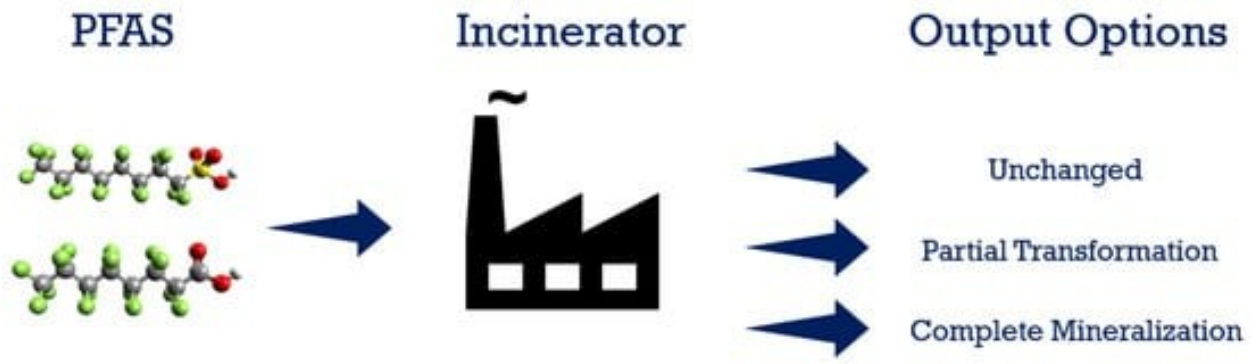

Figure 7: How PFAS are incinerator reproduced from Meegoda et al.[5]

1.2. How are they analyzed and detected?

1.2.1. PFAS Sampling and Sample Preparation

Since PFAS have become widespread due to their usage in many products, they persist in the environment and can be found in various matrices. These matrices include the air, soil, food, products, humans, and aqueous samples. PFAS are present in the air like PFAA particles and volatile FTOHs. PFAS are collected from the air by active and passive air sampling. Active air sampling is divided into two categories, which includes, high volume and low volume sampling instruments. High volume sampling involves using filters made of quartz/glass fibers as well as polyurethane foam inside an XAD resin to collect PFAS. Low volume sampling uses solid phase extraction (SPE) to collect PFAS in indoor environments. Examples of the SPE resins used are divinylbenzene for neutral PFAS and divinylbenzene polymer for neutral and ionized PFAS. Passive air sampling uses PUF disks and is simple and cost-effective to use. Alternatively, polymers like polyethylene sheets are being used to collect neutral and volatile PFAS in indoor air environments. Overall, active sampling is faster and doesn't use an extraction solvent compared to passive sampling methods.[6]

PFAS are also found in different water sources like drinking water, groundwater, wastewater, drinking water, and landfill leachate. Different methods are used to collect water from different sources. For example, surface water, drinking water, and wastewater are sampled by using buckets, autosamplers, and stainless-steel samplers. Groundwater is collected by digging trenches and then collecting water in upper and lower aquifers.[6]

PFAS can also be extracted from dust, sediment, soil, and consumer products. Dust comes from indoor environments and is collected using cleaned brushes or vacuum cleaner bags. Soil samples

are collected from the surface over a selected area using a Van Veen grab and a Ponar grab sampler. For deep soil samples, a Model MC-400 Multi-Corer is used. Consumer products like clothing and food packaging are also tested and are wrapped in aluminum foil when transported to be later frozen.[6]

PFAS have made their way into organisms and plants, which means they are present in a variety of ecosystems. For example, they are found in birds, seafood, humans, and vegetables. These organisms are sampled by purchasing from markets or using traps. Once the samples are obtained, the organs and tissues are collected.[6]

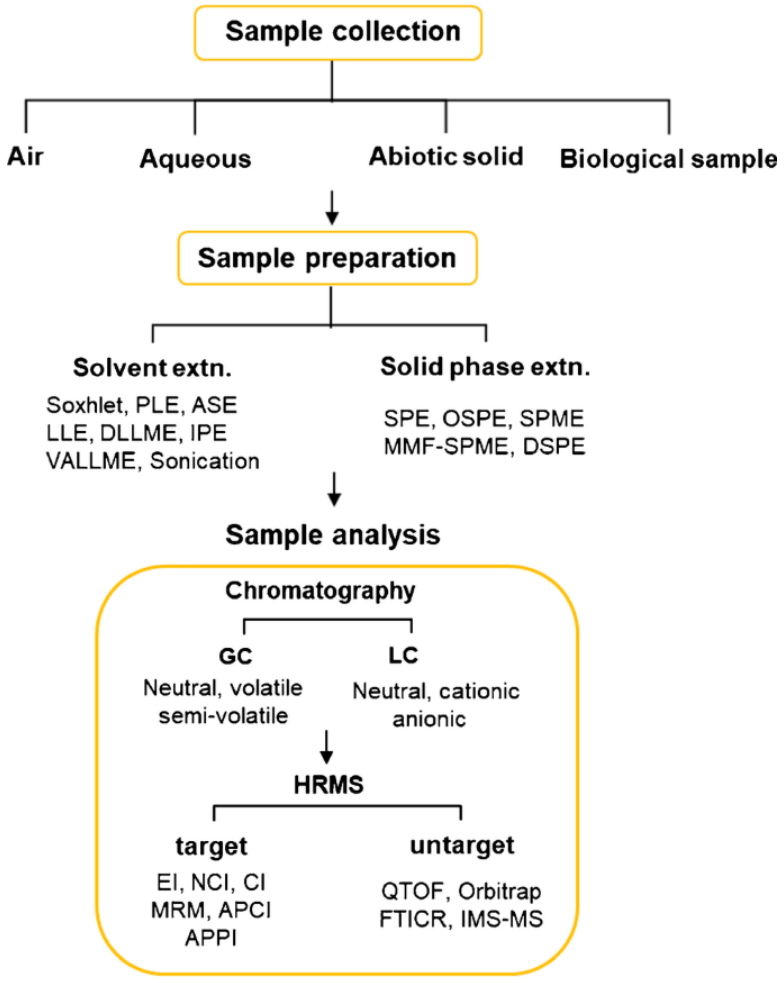

Figure 8: Flowchart of the procedure in which to analyze and detect PFAS in various medias, reproduced with permission from Jia et al.[6]

Once samples have been obtained, PFAS need to be extracted, concentrated, and the matrix interferences need to be removed. The first method is to use solvents to extract PFAS using liquid-liquid extraction (LLE), Soxhlet extraction, pressurized liquid extraction (PLE), ion-pair extraction (IPE), and dispersive liquid-liquid microextraction (DLLME).[6]

LLE is a solvent extraction technique that uses two phases, an aqueous and an organic phase, to separate sample components in order to isolate the target molecules.[7] LLE is a common extraction method when samples contain lots of suspending particles. This technique can efficiently extract shorter chain PFAS, but longer chain PFAS require filtration and other optimization steps.[6]

Soxhlet extraction is another liquid extraction method that places the sample in a thimble, which fills up with extract that is condensed until the thimble overflows (Figure 9). Once this occurs, a siphon removes solvent from the thimble and puts it into the distillation flask. This process is repeated until its completely extracted.[8] The Soxhlet extraction protocol is recommended by the United Nations to extract PFAS. This method is simple but time-consuming and requires lots of solvent. Airborne and solid samples can be extracted using this method using less polar solvents.[6]

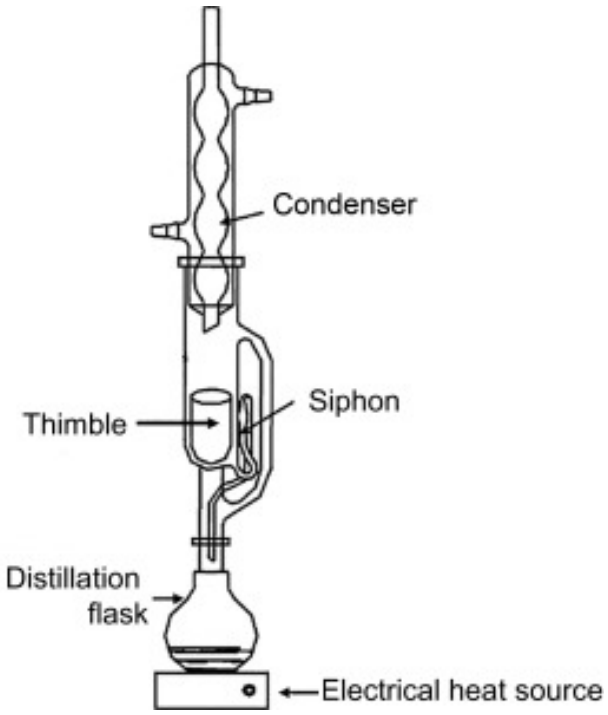

Figure 9: Soxhlet extractor set up, reproduced with permission from López-Bascón et al.[8]

PLE is a liquid extraction technique that uses high pressures and temperatures. This increases mass transfer, decreases solvent surface tension and viscosity. This, in turn, increases the solubility of the analytes, which allows better extraction yields at a faster rate. This process involves adding an extraction solvent to moisten the sample, desorption from the matrix, dissolving the compounds in the extraction solvent, dispersion of the compounds to remove them from the matrix, and diffusion of the compounds to the bulk solvent. This technique, therefore, uses a solvent reservoir connected to a high-pressure pump, which adds the solvent into the system and pushes the extract out. The extraction happens in the extraction cell, where the sample is placed on filter paper. The extraction cell is heated in an oven, and a collecting valve is placed at the end of the system, separated by valves to control the pressure (Figure 10).[9] PLE can also be used to extract organic pollutants and is quicker and more effective than the Soxhlet method. This method can only be used, though, for

samples containing high amounts of PFAS or if the extraction method uses PFAS-free tubing, since low levels of PFAS are present in the equipment used.[6]

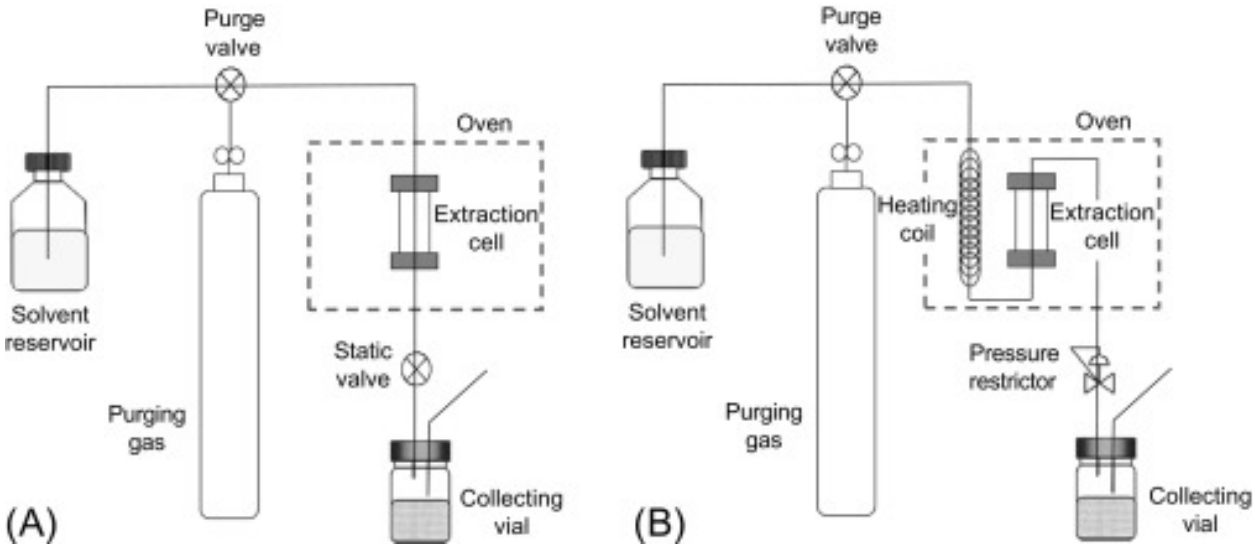

Figure 10: PLE extraction set up, reproduced with permission from Alvarez-Rivera et al.[9]

IPE is another method to extract ionic compounds into an organic phase by using ions of opposite charge. When the compound is dissolved in the aqueous phase, it forms an ion pair with the added counterions so that it can then dissolve into the organic phase.[10] IPE can be used to extract PFAS as well, specifically short-chain PFAS and is good to use for samples with complex matrices with good recoveries. Longer chain PFAS can be extracted using this method as well, but with optimized ion pairs.[6]

DLLME is a technique that extracts analytes by dispersion. A mixture of the extracting and dispersing solvents is made and added into a water sample that contains the analyte of interest. The analyte is then extracted by dissolving it in the extracting solvent. The dispersion is then removed using centrifugation (Figure 11).[11] DLLME utilizes dispersion solvent and extraction solvents like perfluoro-tert-butanol and acetonitrile to isolate PFAS through F-F interactions. This method

works well for longer chain PFAS but not shorter chain PFAS since the perfluoro-tert-butanol is very hydrophobic.[6]

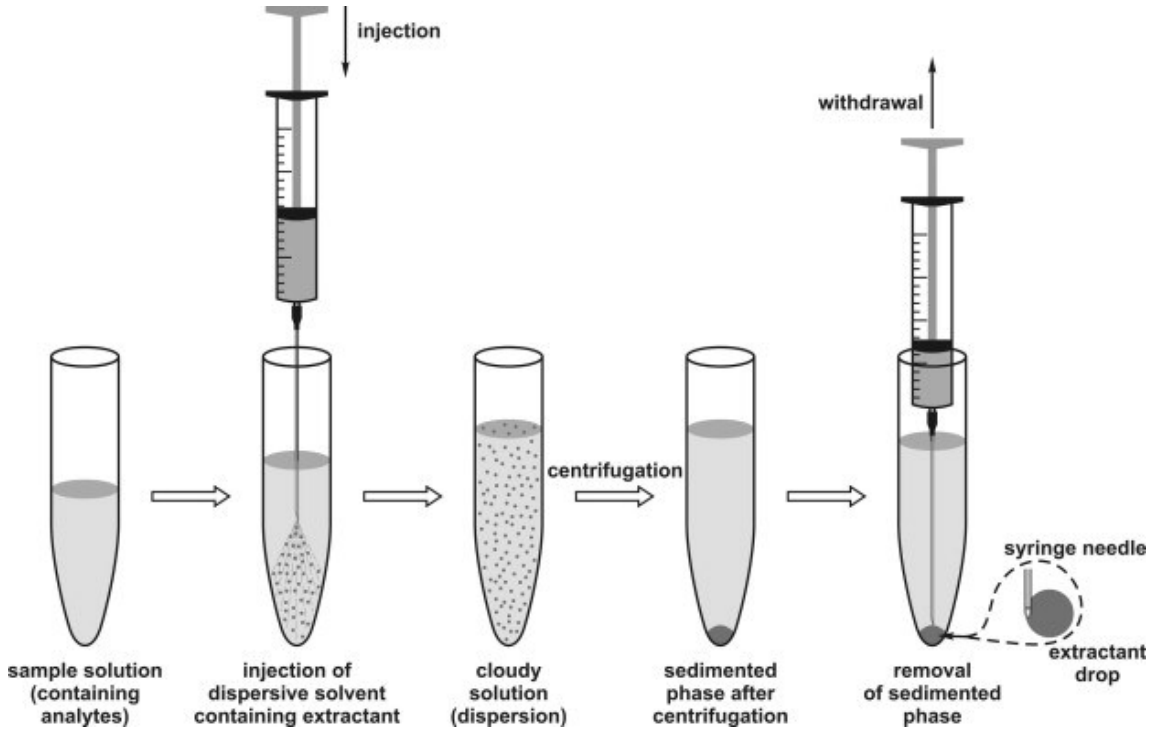

Figure 11: DLLME set up, reproduced with permission from a Zgoła-Grześkowiak et al.[11]

Another PFAS extraction method is to use solid-phase extraction techniques like SPE, dispersive solid-phase extraction (DSPE), and solid-phase microextraction (SPME). SPE works by transferring targeted analytes dissolved in a liquid or gaseous matrix into a solid phase where they are retained. The solid phase is then eluted with solvent to remove the targeted analytes if it's a liquid or thermal desorption if it's a vapour. This method has largely replaced liquid-liquid extractions since it is simple, efficient, and can be applied to different analytes.[12] The SPE method is the most common and popular as there are lots of SPE cartridges available to remove PFAS. For example, WAX cartridges remove charged PFAS and use methanol with an ammonium solution to

elute. For neutral PFAS, ISOLUTE ENV+ can isolate them, and Strata-X cartridges remove different kinds of PFAS. SPE cartridges can also be combined to extract different PFAS in complex matrices.[6]

DSPE is another SPE technique that puts a sorbent into a sample, then it's shaken and centrifuged to isolate the analyte. The sample and the sorbent are in high content with each other, which means equilibrium is reached fast. This method is quick and efficient and requires low amounts of sorbents and solvents.[13] DSPE can extract PFAS from complex sample matrices and is high throughput, can detect PFAS at trace levels, requires less sample handling, and has high extraction recovery.[6]

SPME is another method in which SPE is done under high pressures so that there are smaller pore sizes on the solid adsorbent. This increases efficiency and decreases the sample volumes required.[14] SPME is another solid phase extraction method that doesn't use solvents and instead uses a fused silica fiber to extract PFAS. This method extracts volatile compounds or semi-volatile compounds and can be used as an on-line SPME method to detect PFAS. An open tubular fused-silica capillary column is used so that PFAS are extracted and then detected using high performance liquid chromatography (HPLC). For gas chromatography, a headspace SPME (HS-SPME) method is used for analysis. These methods allow for automation, shorter analysis time, and better precision and accuracy.[6]

1.2.2. LC-MS and GC-MS Methods

Once samples have been collected and PFAS have been extracted, they are usually analyzed by chromatography coupled with mass spectrometry. Chromatography techniques include gas chromatography (GC), liquid chromatography (LC), ultra-performance liquid chromatography

(UPLC), and high-performance liquid chromatography (HPLC). Different mass spectrometry techniques include time of flight mass spectrometry (TOF-MS), multiple reaction monitoring (MRM), an orbitrap MS, triple quadrupole (TQ), and Fourier transform ion cyclotron resonance (FTICR-MS).[6]

Chromatography methods separate samples into its matrix components and analytes of interest. PFAS can have different carbon backbones and functional groups, so it's important that different types of PFAS are separated within the same samples, which also includes isomers.[6] Neutral and volatile PFAS, like FTOH, can be analyzed using GC-MS with WAX columns[6] (WAX columns are weak anion exchange columns[15]) being used for their separation. More commonly, LC-MS is used for the separation and detection of PFAS and more specifically, reversed-phase LC is used for ionic and neutral PFAS.[6] C18 columns are used to separate different PFAS with a polar mobile phase that usually contains water, methanol, and acetonitrile with a salt like ammonium hydroxide or acetate. A gradient program is used for the mobile phase, and additionally, guard columns are used to retain charged PFAS using ion exchange. This allows for samples with multiple PFAS present to be separated adequately. One problem with this method is that ultrashort-chain PFAS that have 1-3 carbons are not retained on the column. This is because they are very small polar compounds that can only be retained and separated using a hydrophilic interaction chromatography ion exchange column (HILIC). Alternative methods for non-targeted analysis include 2D-GC or 2D-LC so that PFAS that elute together can be separated in the second dimension (Figure 12).[6]

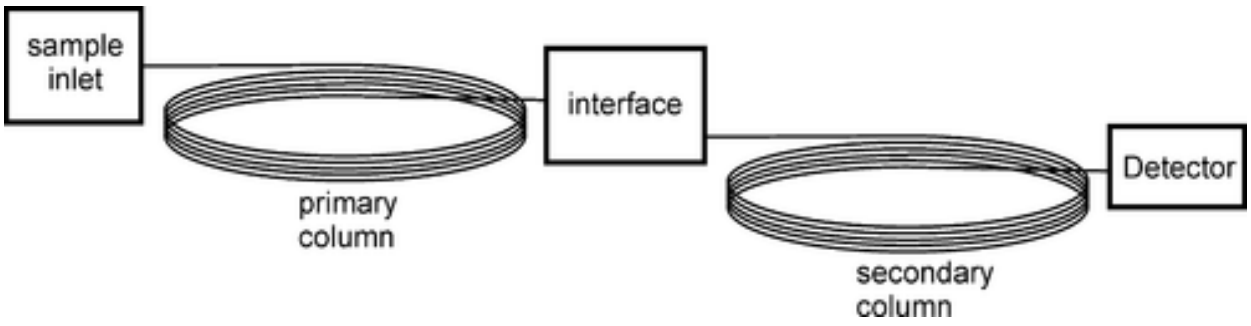

Figure 12: 2D-GC set up, reproduced with permission from Seeley et al.[16]

Once PFAS in a sample have been separated, they are analyzed with high resolution mass spectrometry (HRMS) techniques, which can detect trace PFAS in different sample matrices with a good limit of detection (LOD) and high accuracy. GC-MS is used to detect neutral PFAS and ionizes them using one of the following three methods: electron ionization (EI), atmospheric pressure chemical ionization (APCI), negative ion chemical ionization (NCI), and chemical ionization (CI). The mode in which these ions are analyzed is in selected ion monitoring mode (SIM) in order to target specific PFAS analytes at a time. Neutral and ionic PFAS can be detected using HPLC combined with tandem mass spectrometry (MS/MS). This method requires electrospray ionization (ESI) in negative or positive mode. MRM mode is used to monitor PFAS in various samples and selects for certain analytes with a higher relative abundance. LC-TQ-MS methods and UPLC/MS/MS methods have been used to detect PFAS at trace levels. In order to quantify the PFAS found in samples collected, calibration curves with known standards are prepared. The method of standard addition can also be used for samples with complex matrices to account for matrix effects.[6]

In complex biological studies, matrix-assisted desorption/ionization imaging mass spectrometry (MALDI-IMS) can be used since it can detect and quantify PFAS in complex biological samples. Another method to analyze ionized PFAS in complex aqueous samples uses dielectric barrier

discharge ionization mass spectrometry (DBDI-MS) to remove sample preparation and separation using chromatography. This method works by generating pulses to ionize molecules and reduces background noise, which then increases the signal.[6]

Non-targeted analysis of PFAS is a common identification method, with HRMS being used in order to detect trace levels of PFAS. Various studies have developed automated data analysis methods to detect PFAS using available databases that contain different PFAS structures and transformation products with their MS/MS data. These workflows aid in the identification of unknown PFAS in complex biological samples. The first step in these workflows is to use HRMS to detect all ions in a sample, then suspected PFAS features are selected, and then these features are confirmed using databases. An example of this workflow would be the following: An HRMS method is selected that detects PFAS in full-scan modes include quadrupole time of flight (QTOF), FTICR, and orbitrap. These methods are used due to their high resolving power and high mass accuracy. Once the data is collected, it needs to be filtered for PFAS features by using software's like MZmine or XCMS to remove background signals, set an intensity threshold, and group isotope or adduct peaks together. Additional filtering methods include looking for mass defects, neutral loss, homologous series, or diagnostic fragments. Once features have been selected, the m/z ratio can help determine the molecular formula of the compound. This is where software and databases can be used to determine the PFAS present in the sample based on mass, MS/MS spectra, and elemental composition.[6]

1.2.3. Short Chain PFAS

More recently, shorter chain PFAS are replacing longer chain ones like PFOA and PFOS. These shorter chain PFAS, like perfluorobutane sulfonic acid (PFBS), or perfluorobutanoic acid (PFBA),

are more persistent in the environment, even though they have lower acute toxicity and less bioaccumulation compared to longer chain PFAS. There has been an increased focus lately on their removal since long-chain PFAS are being phased out. Certain removal methods like electrochemical treatment or oxidation can be used to remove short-chain PFAS, but these processes produce byproducts that are more toxic. This can especially be a problem for short-chain PFAS since they are already toxic.[17]

There are other alternative ways to remove short-chain PFAS, some of which have been discussed previously, but this research will focus on an alternative method.

1.3. Goals of this Research

The purpose of my research project is to study how short-chain PFAS degrade using different techniques. Since shorter-chain PFAS are replacing longer-chain ones, there is an increased need to study how they degrade. The first method selected five short-chain PFAS to undergo degradation using collision induced dissociation on a triple quadrupole mass spectrometer. These included: 2,2,3,3,3-pentafluoropropionic acid, 3,3,3-trifluoropropionic acid, 2,2,3,3,3-pentafluoro-1-propanol, 3,3,3-trifluoro-1-propanol, and trifluoromethanesulfonic acid. This method also determines how to detect these shorter-chain PFAS using mass spectrometry. The second method focused on pyrolytic degradation of three short-chain perfluorinated compounds, 3,3,3-trifluoropropionic acid, 3,3,3-trifluoro-1-propanol, and 2,2,3,3,3-pentafluoro-1-propanol. The work was carried out with a Chen-type microreactor on the VUV beamline of the Swiss Light Source synchrotron facility. The unimolecular reaction for the ion dissociation and neutral pyrolysis of these short-chain PFAS was then investigated.

1.4. Chapter 1 References

(1) Yaghoobian, S.; Ramirez-ubillus, M. A.; Zhai, L.; Hwang, J. A Perspective of Emerging Trends in Integrated PFAS Detection and Remediation Technologies with Data Driven Approaches. *Chem. Sci.* **2025**, *16* (30), 13564–13573. https://doi.org/10.1039/d5sc01624j.

(2) Sharma, N.; Kumar, V.; Sugumar, V.; Umesh, M.; Sondhi, S.; Chakraborty, P.; Kaurf, K.; Thomas, J.; Kamaraj, C.; Maitra, S. S. A Comprehensive Review on the Need for Integrated Strategies and Process Modifications for Per- and Polyfluoroalkyl Substances (PFAS) Removal: Current Insights and Future Prospects. *Case Stud. Chem. Environ. Eng.* **2024**, *9* (100623), 1–17. https://doi.org/10.1016/j.cscee.2024.100623.

(3) Singh, K.; Kumar, N.; Kumar, A.; Singh, R.; Kumar, K. Per-and Polyfluoroalkyl Substances (PFAS) as a Health Hazard : Current State of Knowledge and Strategies in Environmental Settings across Asia and Future Perspectives. *Chem. Eng. J.* **2023**, *475* (145064), 1–29. https://doi.org/10.1016/j.cej.2023.145064.

(4) Brake, H. D.; Langfeldt, A.; Kaneene, J. B.; Wilkins, M. J. Current Per- and Polyfluoroalkyl Substance (PFAS) Research Points to a Growing Threat in Animals. *J. Am. Vet. Med. Assoc.* **2023**, *261* (7), 1–7. https://doi.org/10.2460/javma.22.12.0582.

(5) Meegoda, J. N.; Souza, B. B. De; Casarini, M. M.; Kewalramani, J. A. A Review of PFAS Destruction Technologies. *Int. J. Environ. Res. Public Health* **2022**, *19* (24), 16397. https://doi.org/10.3390/ijerph192416397.

(6) Jia, S.; Dos Santos, M. M.; Li, C.; Snyder, S. A. Recent Advances in Mass Spectrometry Analytical Techniques for Per- and Polyfluoroalkyl Substances (PFAS). *Anal. Bioanal.*

Chem. **2022**, *414*, 2795–2807. https://doi.org/10.1007/s00216-022-03905-y.

(7) Cantwell, F. F.; Losier, M. Chapter 11 Liquid—Liquid Extraction. In *Comprehensive Analytical Chemistry*; Elsevier, 2002; pp 297–340. https://doi.org/10.1016/S0166-526X(02)80048-4.

(8) López-Bascón, M. A.; Luque de Castro, M. D. Chapter 11 - Soxhlet Extraction. In *Handbooks in Separation Science, Liquid-Phase Extraction*; Poole, C. F., Ed.; Elsevier, 2020; pp 327–354. https://doi.org/10.1016/B978-0-12-816911-7.00011-6.

(9) Alvarez-Rivera, G.; Bueno, M.; Ballesteros-Vivas, D.; Mendiola, J. A.; Ibañez, E. Chapter 13 - Pressurized Liquid Extraction. In *Handbooks in Separation Science, Liquid-Phase Extraction*; Poole, C. F., Ed.; Elsevier, 2020; pp 375–398. https://doi.org/10.1016/B978-0-12-816911-7.00013-X.

(10) B.-A. Persson. LIQUID CHROMATOGRAPHY | Ion Pair. In *Encyclopedia of Analytical Science (Second Edition)*; Worsfold, P., Townshend, A., Poole, C., Eds.; Elsevier, 2005; pp 157–164. https://doi.org/10.1016/B0-12-369397-7/00325-3.

(11) Zgoła-Grześkowiak, A.; Grześkowiak, T. Dispersive Liquid-Liquid Microextraction. *TrAC Trends Anal. Chem.* **2011**, *30* (9), 1382–1399. https://doi.org/10.1016/j.trac.2011.04.014.

(12) Poole, C. F. New Trends in Solid-Phase Extraction. In *TrAC Trends in Analytical Chemistry*; Elsevier, 2003; pp 362–373. https://doi.org/10.1016/S0165-9936(03)00605-8.

(13) Piotr, Ś.; Kosobucki, P. Recent Materials Developed for Dispersive Solid. *Molecules* **2020**, *25* (21), 4869. https://doi.org/10.3390/molecules25214869.

(14) Lockwood, T. E.; Talebi, M.; Minett, A.; Mills, S.; Doble, P. A.; Bishop, D. P. Micro Solid-Phase Extraction for the Analysis of per- and Polyfluoroalkyl Substances in Environmental Waters. *J. Chromatogr. A* **2019**, *1604*, 460495. https://doi.org/10.1016/j.chroma.2019.460495.

(15) Iannone, A.; Carriera, F.; Fiore, C. Di; Avino, P. Poly- and Perfluoroalkyl Substance (PFAS) Analysis in Environmental Matrices : An Overview of the Extraction and Chromatographic Detection Methods. *Analytica* **2024**, *5* (2), 187–202. https://doi.org/10.3390/analytica5020012.

(16) Seeley, J. V; Seeley, S. K. Multidimensional Gas Chromatography: Fundamental Advances and New Applications. *Anal. Bioanal. Chem.* **2012**, *85* (2), 557–578. https://doi.org/10.1021/ac303195u.

(17) Valencia, A.; Ordonez, D.; Sadmani, A. H. M. A.; Reinhart, D.; Chang, N.-B. Comparing the Removal and Fate of Long and Short Chain Per- and Polyfluoroalkyl Substances (PFAS) during Surface Water Treatment via Specialty Adsorbents. *J. Water Process Eng.* **2023**, *56*, 104345. https://doi.org/10.1016/j.jwpe.2023.104345.

Chapter 2: Techniques

2.1. Introduction to the techniques used

In order to investigate the degradation products of short-chain PFAS, collision induced dissociation on a triple quadrupole mass spectrometer was done to investigate the ion chemistry. The next method used pyrolytic degradation with iPEPICO at the Swiss Light Source to investigate the neutral products. Once the degradation products were obtained using both methods, their unimolecular dissociation and rates were determined using computational techniques.

2.2. Triple quadrupole mass spectrometry

2.2.1. Techniques

Triple quadrupole mass spectrometry was a technique used to study the breakdown of five short-chain PFAS using CID. Triple quadrupole mass spectrometry is a mass analysis technique that uses three quadrupoles to separate and detect ions (Figure 13). The sample is injected into the instrument sample inlet, where nitrogen curtain gas is passed through. The ions then enter a lower-pressure orifice and then enter the skimmer. This part of the system is kept under vacuum by a rotary pump. The skimmer then allows ions to enter an rf (radio frequency voltage) only region, which is Q0 and then enter a prefilter that is kept under vacuum by a turbo pump. Once past the prefilter, the ions enter Q1, which is the first quadrupole that allows for mass selection. Mass selected ions in Q1 then enter Q2, which is the collision cell and only has rf mode as well and is kept under vacuum by a turbo pump. In Q2, ions collide with collision gas to dissociate into fragments, which are then mass resolved in Q3 and then are detected.[1]

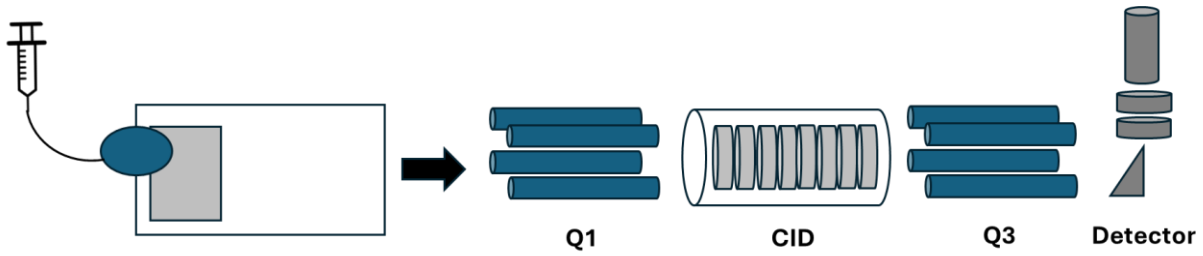

Figure 13: Schematic of a triple quadrupole mass spectrometer.

The triple quadrupole instrument used for this research was the Micromass Quatro Ultima, which can do direct injection with a syringe pump and perform MS/MS analyses on targeted molecules. The instrument is under vacuum using two rotary pumps and two turbomolecular pumps. The rotary pumps are used for the ion source and the first ion tunnel. The turbomolecular pumps are for the analyzer and ion transfer region. When the sample is injected, it gets ionized at atmospheric pressure, and there are two ionization methods, which include atmospheric pressure chemical ionization and electrospray ionization using a Z-spray source (Figure 14). These experiments were conducted with electrospray ionization, which involved using a strong electric field being applied to the sample flow coming out of the nebulizer. This then produces an aerosol that contains charged droplets that undergo ion evaporation. This phenomenon occurs when the droplets reduce in size as the solvent evaporates, which causes the sample's charge density to increase, which then allows the sample ions to be ejected from the surface of the droplet. The ions are sent through a series of orifices (ion tunnels) before entering the prefilter.[2]

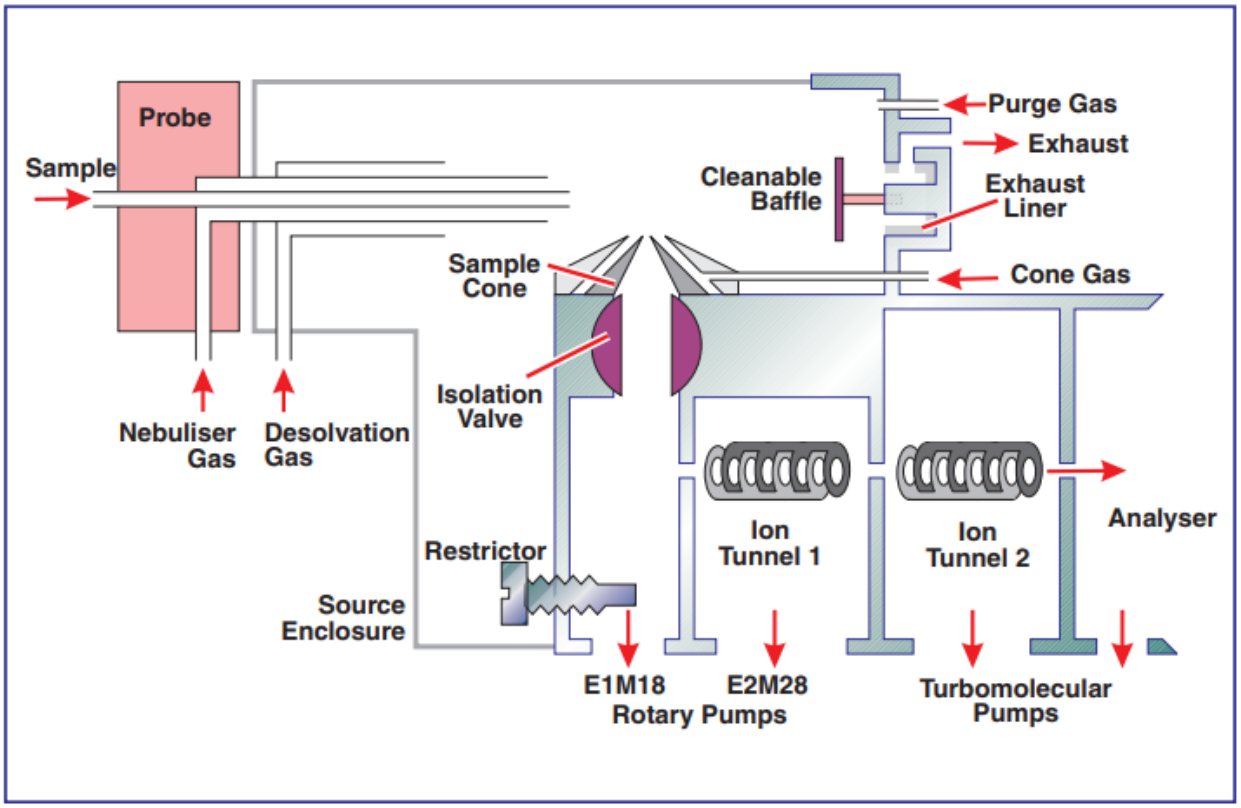

Figure 14: Waters Micromass Quattro Ultima Z-spray ESI source diagram.[2]

The triple quadrupole mass spectrometer can operate in a variety of different modes. In Q1 mode, the first quadrupole is used as a mass filter and resolves all the masses of the molecules in a sample. The ions pass through Q2 and Q3 without fragmentation and mass filtering (RF only mode). In MS/MS mode, one of the advantages of using a triple quadrupole mass spectrometer is that there are a variety of experiments you can do depending on what masses you are trying to analyze and isolate (Figure 15). For example, a product ion scan selects a parent mass in Q1, then sends them to Q2 for collision induced dissociation (CID), finally all the products are detected in Q3. The precursor ion scan, scans for all mases in Q1, they all undergo CID in Q2, and only a selected mass is detected in Q3. Multiple reaction monitoring (MRM) is when a parent mass is selected in Q1, CID is preformed in Q2, and a specific mass is selected in Q3. The final mode is a constant

neutral loss scan, Q1 and Q3 are scanning in sync for all mass. Q2 is used to fragment the sample ions and the data in Q3 is analyzed for a neutral loss fragment from a fragmentation pathway. Once ions have been mass selected, they are detected using a photomultiplier detection system.[2]

MS-MS Operating Modes	Q1	Q2 (CID)	Q3
Product Ion Scan	Precursor Mass Selection	RF only	Scanning Mode
Precursor Ion Scan	Scanning Mode		Product Mass Selection
Multiple Reaction Monitoring	Precursor Mass Selection		Product Mass Selection
Neutral Loss Scan	Scanning Mode		Scanning Mode

Figure 15: Waters Micromass Quattro Ultima MS-MS operating modes.[2]

2.2.2. Method Selection and Data Processing

Short-chain PFAS, 2,2,3,3,3-pentafluoropropionic acid, 3,3,3-trifluoropropionic acid, 2,2,3,3,3-pentafluoro-1-propanol, 3,3,3-trifluoro-1-propanol, and trifluoromethanesulfonic acid were analyzed using the Waters Micromass Quattro Ultima triple quadrupole mass spectrometer. The daughter ion scan mode was used in order to select for the parent mass, and CID was used to fragment it into products. All the products were then selected in Q3 and identified. The purpose of

this experiment was to determine the unimolecular reaction dynamics involved in transforming the parent molecules into their daughter fragments.

MS/MS analysis is commonly used for structure identification and to analyze complex mixtures since it has high selectivity. MS/MS was initially done with sector instruments at collision energies of keV. It was later discovered that MS/MS with CID could be performed at lower energies, around 10-100 eV. This leads to the triple quadrupole mass spectrometer, which can mass select ions, fragment them, and selectively detect the products. The CID cell (Q2) contains an inert gas at pressures around 10^{-4} to 10^{-2} torr. The inert gas collides with the ions and transfers translational energy, which becomes internal energy in the ion. The excited ions then fragment through unimolecular reactions to form product ions, which are mass analyzed in Q3.[1]

A coordinate system is an easy model for the collision between a neutral gas and an ion that contains a center of mass. This is referred to as the center of mass coordinate system and can be used to explain what happens when a fast-moving ion hits a stationary molecule. The system assumes that the ion and neutral have equal and opposite momentum. After the collision, the ion and neutral gas molecule have new equal and opposite momentum. The angle between the final velocity vectors is the center of mass scattering angle (Figure 16). This collision is inelastic as some of the translation energy is converted into internal energy. In the laboratory frame of reference model, the ion has an initial velocity, while the inert gas has none. Therefore, this initial velocity is added to the velocity vector of the ion in the center of mass frame. This also means that the scattering angle in this case influences the collision velocity vector of the ion in the lab frame.[1]

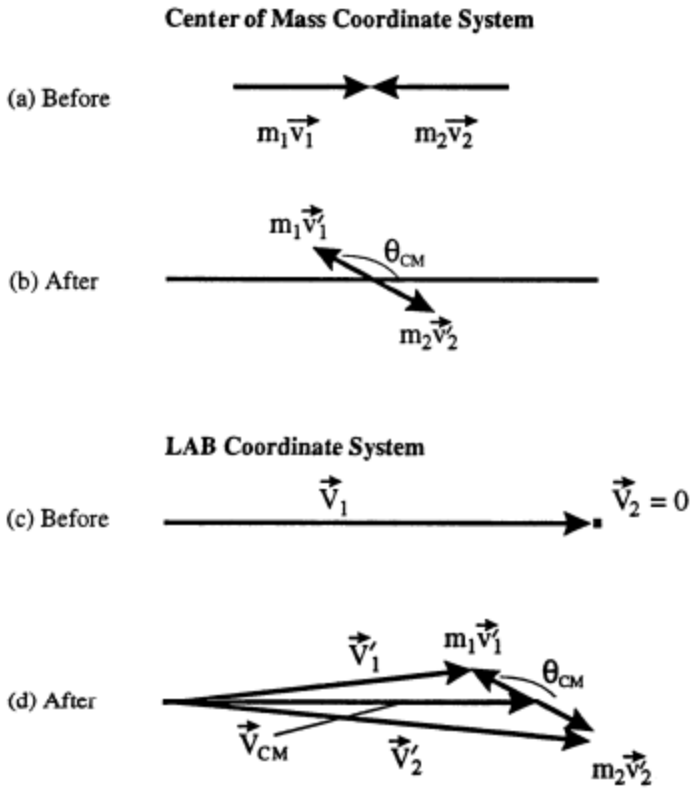

Figure 16: Schematic of the center of mass coordinate system model and lab coordinate system model to analyze the collision between an ion and inert gas during CID reproduced with permission from D.J. Douglas.[1]

Using the lab frame model, the total energy that is transferred into the internal energy of the target molecules represents the energy of the ion and neutral in the center of mass system. Therefore, the center of mass energy is only converted into internal energy due to conservation of energy and momentum. This can be represented by the following formula.[1]

$$E_{com} = \frac{m_2}{M} E_{Lab}\,, M = m_1 + m_2 \quad (2.1)$$

This formula is adapted to the experimental work described in this thesis as:

$$E_{com} = \left(\frac{m_{Ar}}{m_{Ar}+m_{PFAS}}\right) E_{lab} \quad (2.2)$$

Where m_{Ar} and m_{PFAS} are the masses of argon and the ion being investigated. Therefore, once the five short-chain PFAS were fragmented using CID, the parent and fragment molecule abundances were recorded and plotted as a function of E_{com}. This allowed for the creation of breakdown diagrams that showed how the parent molecule decreased over time and the products increased over time as the collision energy varied.

2.3. Imaging Photoelectron Photoion Coincidence Spectroscopy (iPEPICO)

2.3.1. Theory and Technique

Imaging photoelectron photoion coincidence spectroscopy (iPEPICO) was used to study the pyrolysis of three short-chain PFAS (2,2,3,3,3-pentafluoropropionic acid, 3,3,3-trifluoropropionic acid, and 2,2,3,3,3-pentafluoro-1-propanol) and took place at the Swiss light source synchrotron (SLS) (Figure 17). The pyrolysis setup used at the SLS was as follows: The volatile liquid sample is injected and diluted with argon gas to ensure unimolecular reactions occur. It then enters a cooling chamber to ensure all the instrument parts are protected from the heat. Then the vapour enters a Si:C heating block where pyrolysis occurs. This process forms neutral products from unimolecular reactions. Then a molecular beam forms and gets ionized by synchrotron radiation, which ionizes it to form a molecular ion with a respective electron (equation 2.3). The ions are detected at the TOF detector perpendicular to the molecular beam. The ejected electrons hit a detector opposite to the TOF detector. The ions and electrons are accelerated in opposite directions due to an extraction potential that is placed across the ionization region. The electrons hit the detector first since they travel faster, and then the ions hit the TOF detector last. This process is referred to as a coincidence event. Electrons that hit the detector at the center have zero kinetic energy electrons, while electrons that don't hit the center of the detector are referred to as hot electrons.

$$M \xrightarrow{h\nu} M^+ + e^- \text{ (2.3)}$$

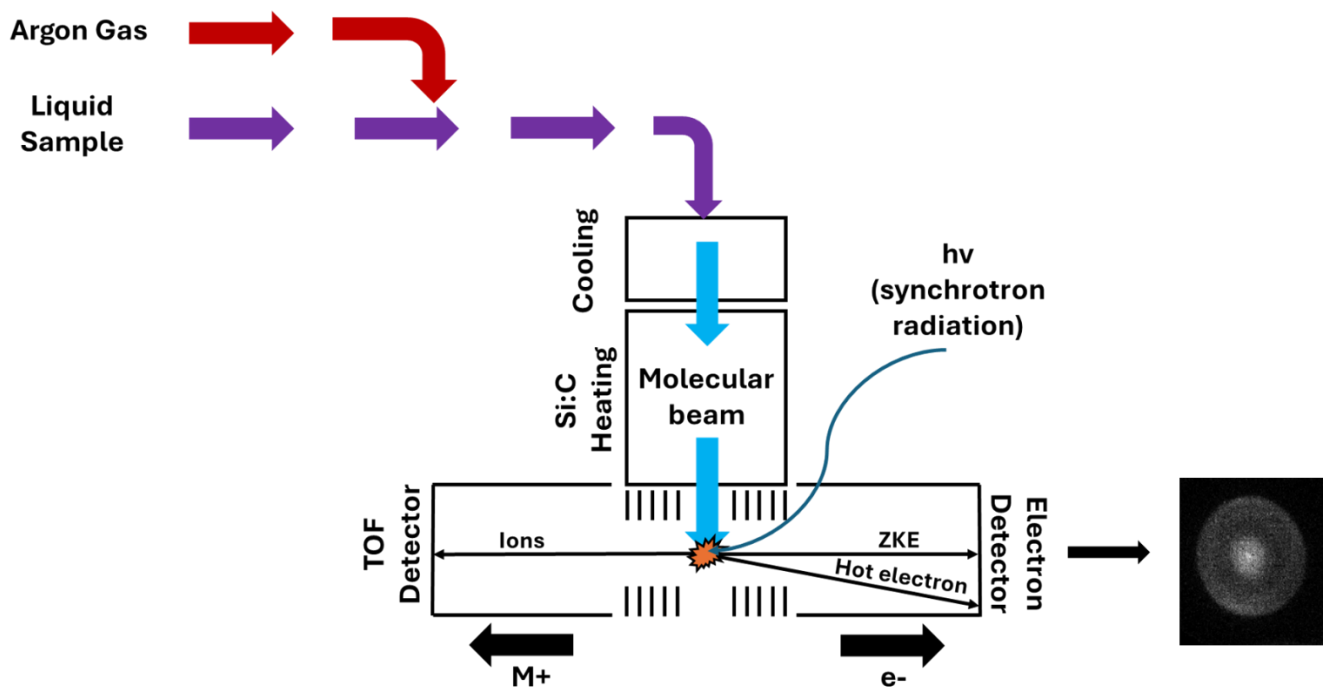

Figure 17: Schematic of the pyrolysis set up at the SLS.

These hot electrons have kinetic energy and hit the detector off-center. This kinetic energy can be explained by equation (2.4), where the photon energy (hv) is equal to the adiabatic ionization energy (IE_a) minus the energy of the neutral (E_{neu}), plus the internal energy of the ion (E_{int}), and plus the kinetic energy of the electron (KE_e).

$$h\nu = E_{int} - E_{neu} + IE_a + KE_e \text{ (2.4)}$$

Since only zero kinetic energy electrons are considered, this term is equal to zero, and the new equation becomes the following:

$$h\nu = E_{int} - E_{neu} + IE_a \text{ (2.5)}$$

Therefore, the ionization energy can be determined during the data extraction process. Hot electrons, though, can still end up hitting the center of the detector to account for all hot electrons. The electron intensity for zero kinetic energy electrons is obtained by isolating the center spot on the detector and subtracting the circle around it in the i2PEPICO software (Figure 18).

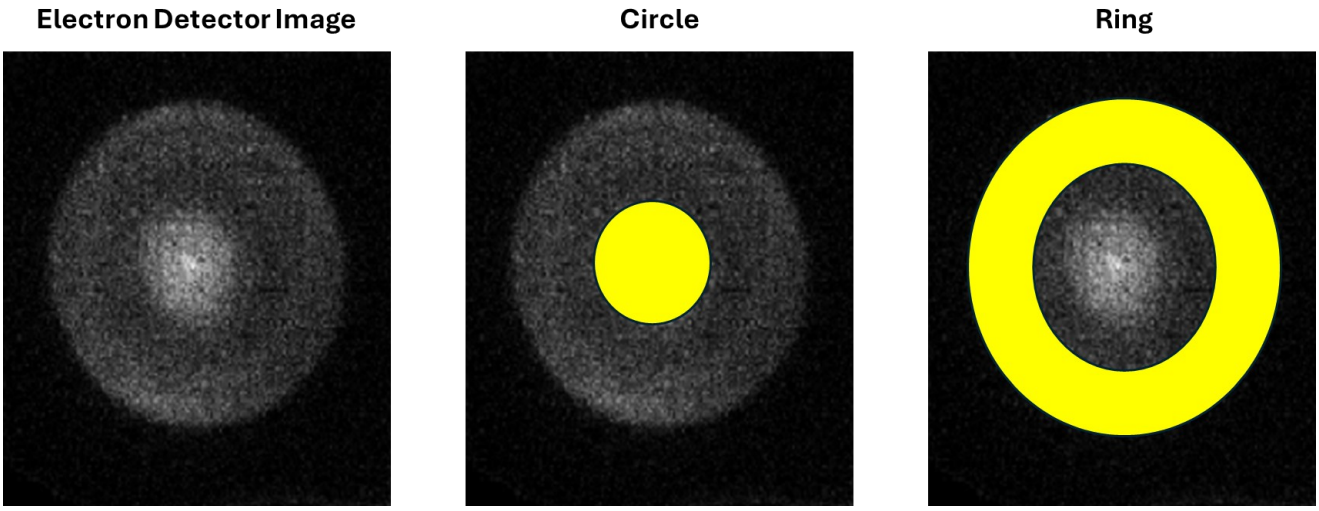

Figure 18: Schematic of the electron image detector with the hot electrons being isolated for removal in the i2PEPICO software.

2.3.2. Data Processing

Once iPEPICO data is obtained for the three short-chain PFAS, the data needs to be processed and analyzed for the pyrolysis products. From the i2PEPICO software, the ion intensities from the center spot and ring, along with the photon energies and acquisition time, are obtained for each pyrolysis product. The first step to process this data is to subtract the ring intensity from the center intensity and multiply by a multiplication factor like 0.7. Then this value is divided by the acquisition time to obtain the electron signal as a function of photon energy. In order to obtain a mass selected threshold photoelectron spectrum (ms-TPES), mass selected ion intensities are

subtracted but one is multiplied by a multiplication factor. The intensities of all ions are plotted as a function of photon energy.

ms-TPES show the vibrational structure of the ion due to the Franck-Condon principle. This principle states that when ionization occurs, the nuclei are fixed and therefore the electrons transition into higher similar excited vibrational states and results in higher intensity bands (Figure 19).[3] In order to calculate this, density functional theory (DFT) on the Guassian 16 platform is used to create a FC simulations to verify the structure of the products produced (will be discussed more in the next section of this chapter). This is a combination of matching ionization energies ensures that the predicted products match their ms-TPES and can be confirmed as pyrolysis products that formed from the unimolecular reactions of the three short chain PFAS.

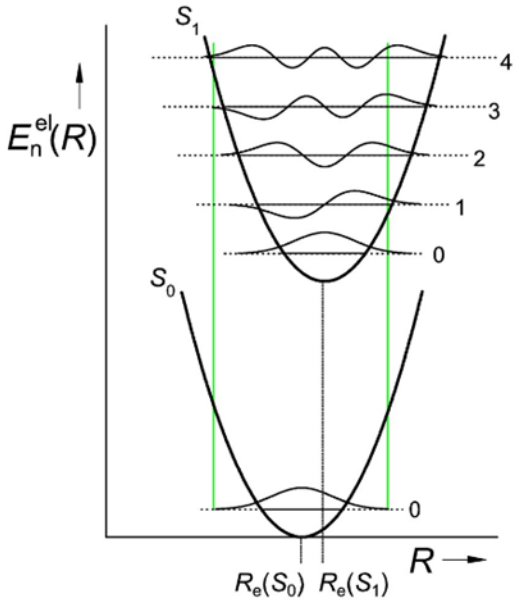

Figure 19: Schematic of Franck-Condon principle for a diatomic molecule reprinted with permission from Heinz Mustroph .[3]

2.4. Computational Methods and Statistical Modelling

2.4.1 Rice-Ramsperger-Kassel-Marcus (RRKM) Theory

The Rice-Ramsperger-Kassel-Marcus (RRKM) Theory helps estimate the rate of the unimolecular reactions determined through the CID and pyrolysis experiments. A unimolecular reaction is one in which one reactant is transformed into a product due to a chemical reaction caused by thermal activation, inelastic collisions, photoactivation, etc. In this case, a certain amount of energy known as the activation energy is required for the molecule to have a certain amount of internal energy to react. The rate of a reaction is usually determined by the speed at which the concentrations of reactants are consumed and products formed over time. The RRK (Rice-Ramsperger-Kassel) model, though, suggests that the molecule is in a system of identical hormonic oscillators, each with a respective frequency. These oscillators are loosely coupled and only allow for energy to flow between them. A key feature of this model is that if a molecule gains enough energy to react, that energy needs to be distributed across all modes of motion before concentrating on a bond critical for the reaction to take place. RRKM theory accounts for the molecular structure of the reactant as well as the addition of a transition state to calculate the rate of reaction.[4]

The RRKM equation is as follows:[5]

$$k(E) = \frac{\sigma N^{\ddagger}(E-E_0)}{h\rho(E)} \quad (2.6)$$

Equation 2.6 shows that the rate for a reaction, k(E), depends on a given energy E and the activation energy E_0. The reaction degeneracy is represented by σ, *h* is Planck's constant, the transition state sum of states is represented by $N^{\ddagger}(E-E_0)$, and ρ(E) is the density of states of the reactant. The density of states refers to the vibrational degrees of freedom of the reactant at a specific internal

energy. The sum of states is the number of ways that the energy can divide itself among a certain number of oscillators. It also represents the number of ways in which you can pass through a transition state barrier. A key difference between RRKM and RRK theory is that in RRKM, each oscillator is not treated as the same but instead corresponds to a different vibrational frequency. There is a critical coordinate in the transition state where energy is needed in order for the reactant to transform into the product. The energy required to reach this transition state barrier is E_0. The rest of the energy, $E-E_0$, goes into the product vibrational modes. Another additional factor to consider is that some energy goes into the translational modes of the product ions, thus the internal energy that goes into the product vibrational modes is $E-E_0-\varepsilon$. This is all shown in Figure 20, where E_0 is required to reach the transition state, and E is the energy provided to the system, and finally $E-E_0-\varepsilon$ is the energy remaining in the products.[5]

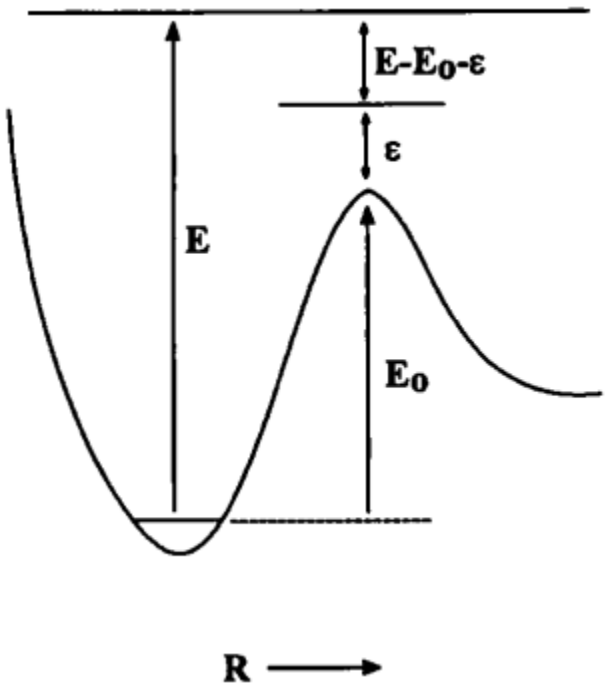

Figure 20: Reaction coordinate diagram for dissociation of a molecule with its transition state barrier and the relationship between E and E_0 reprinted from Baer et al.[5]

Another variable to consider is the entropy of activation, $\Delta S^{\ddagger}$, which can be used to describe the rate of the reaction. This is because the reacting ion and transition state vibrational frequencies can be used to determine $\Delta S^{\ddagger}$. The entropy of activation is used in this case to describe the type of unimolecular reaction that is occurring. Positive entropies mean that the transition states are less ordered than the reactant. A less ordered transition state is referred to as a loose transition state and represents bond cleavage reactions. Negative entropies mean that the transition states are more ordered than the reactant. A more ordered transition state is referred to as a tight transition state and represents a rearrangement reaction. The entropy of activation can be determined by the following equation:[5]

$$\Delta S^{\ddagger} = k_B \ln \frac{Q^{\ddagger}}{Q} + \frac{U^{\ddagger} - U}{T} \quad (2.7)$$

In equation 2.7, Q is the total partition function, K_b is the Boltzmann constant, T is the temperature in Kelvin, and U is the average internal energy. E_0 and $\Delta S^{\ddagger}$ affect the rate constant of a reaction since E_0 affects the magnitude, while $\Delta S^{\ddagger}$ affects the slope. Therefore, the rate of a reaction can be determined by plotting the rate as a function of E, with the slope being represented by $\Delta S^{\ddagger}$. Tight transition states have gradual slopes while loose transition states have steep slopes (Figure 21).[5]

Entropy of activation was calculated on select unimolecular reactions in this work to determine why certain reactions were more favourable than others. This was done through ab initio calculations by determining the transition state and its vibrational frequencies. Therefore, the vibrational frequencies of the reactant and transition state are used to calculate the entropy of activation for competing reactions.[5]

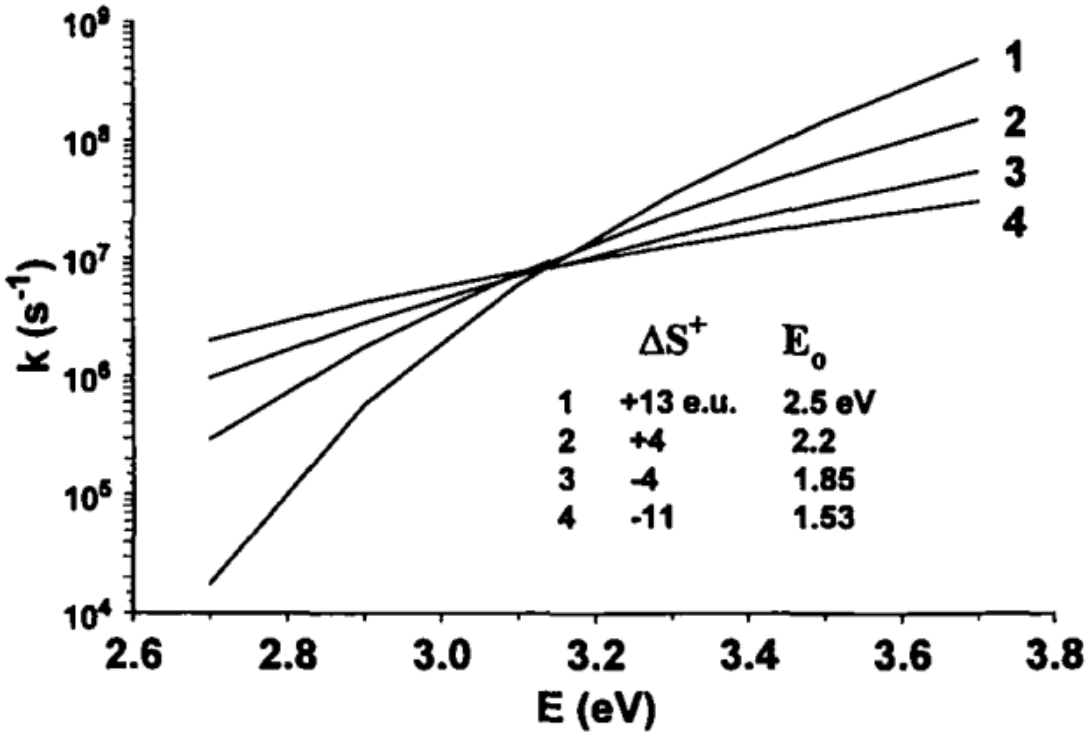

Figure 21: This figure shows the effect $\Delta S^{\ddagger}$ has on the rate of a reaction from ·CH3 loss from 2-butene ions reprinted from Baer et al.[5]

2.4.2 Basis Sets and Correlation Methods

In order to calculate the transition states with their respective energies for the unimolecular reactions that occur in CID or pyrolysis experiments, computational methods are used. The platform that was used in this work was Gaussian 16, which does quantum chemical calculations using Gaussian basis sets to do molecular calculations. Ab initio as well as DFT are calculations that are trying to solve the electronic Schrödinger equation.[6]

Two methods are used to "solve" the Schrödinger equation in systems with more than 1 electron which are Hartree-Fock (HF) and DFT. The problem with the HF method is that it uses single particle wavefunctions, and it's too complex to include correlation corrections. DFT has overcome

these problems by modelling interactions between particle densities within the system and external forces. Therefore, it uses density functions to approximate the solutions. DFT uses the Kohn-Sham system of fictitious orbitals, which is a set of Hartree single particle equations, in order to solve the equation.[7]

Using DFT, the method is the expansion of the electron wavefunction or it's using the exchange-correlation functional. The basis set is the expansion of one-electron orbitals. Gaussian basis sets are made up of basis functions, and a linear combination of basis functional is done to create one functional like the following:[6]

$$\varphi = \sum_i n_i \chi_i \quad (2.8)$$

Equation 2.8 represents the contracted wavefunction equation, where χ_i, is the contracted wavefunction and n_i is the contraction coefficient. There are multiple methods in which the n and the exponents in the contracted wavefunction χ_i can be optimized into a basis set.[8] Basis sets are optimized depending on what the calculations are being used for. Gaussian orbitals can be classified based on the functions used. For example, minimal basis sets have functions that are only required to keep the electrons in an atom, like s and p functions. This method though, has no electron correlation feature. In order to improve upon this method, the number of functions can be doubled or tripled, referred to as double zeta or triple zeta basis sets. Usually, basis sets use functions in which the valence electrons are increased in zeta, which are known as split valence basis sets. In order to achieve higher accuracy, angular momentum functions are added in systems in which electrons in the neutral atom are not in that state. For example, adding d functionals for Neon. This method is referred to as polarization functions or correlation functions.[6]

Atomic Natural Orbital (ANO) Basis Sets make up the basis of most basis sets in order to reduce contraction error, which is the energy difference between contracted and uncontracted basis calculations. This led to the development of a contraction coefficient that can be used in many different kinds of basis sets. Correlation consistent (cc) basis sets were developed in order to solve systems with lots of functions in the ANO basis sets that have high angular momentum. The cc basis sets are lower in energy and use contractions for occupied orbital functions. Diffuse functions are small exponent functions in a basis set that allow for long-range wavefunctions.[6]

DFT methods have been increasing since they have replaced HF methods due to accounting for electron correlation effects.[9] B3LYP is an exchange correlation functional, which is a hybrid functional that mixes DFT with HF and is a semi-empirical method.[10] It stands for Becke, 3-parameter, Lee-Yang-Parr.[11] B3LYP is a basis set that has been developed using DFT, since there is reduced computational cost with accurate results. This basis set is used for calculations involving gas-phase organic molecules.[9] In this work, B3LYP was combined with 6-311++G(d,p), which means that a triple zeta split valence basis set that includes a diffuse function and polarization functions (Figure 22).[12]

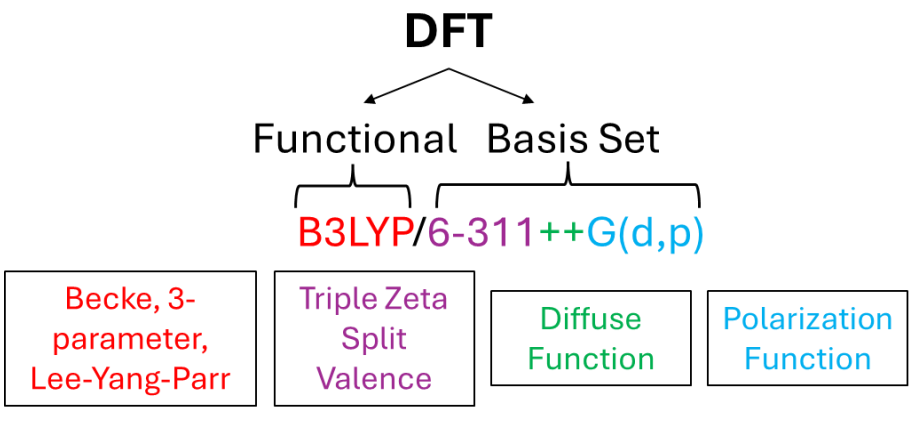

Figure 22: Schematic showing the DFT functional and basis set used for the computational analysis of organic molecules.

The other level of theory that was used in this research was CBS-QB3, which is a Complete Basis Set model that uses multiple levels of theory. This model has a huge computational cost due to it using higher level calculations which expands the basis set to the limit and has higher degrees of correlation. The first step of CBS-QB3 is geometry optimization at the B3LYP level, followed by a frequency calculation, and then it's followed by three single-point calculations: CCSD(T), MP4SDQ, and MP2 levels. The final energies are then obtained from CBS extrapolation. In this research, B3LYP/6-311++G(d,p)was used to determine the optimized geometries, frequencies, transition states and Franck-Condon simulations. Then, CBS-QB3 was used to determine the ionization energies.[13]

2.5 References

(1) Douglas, D. J. Applications of Collision Dynamics in Quadrupole Mass Spectrometry. *J Am Soc Mass Spectrom 9* **1998**, *9*, 101–113. https://doi.org/10.1016/S1044-0305(97)00246-8.

(2) *Quattro Ultima User's Guide*; Micromass UK Limited: Wythenshawe, UK.

(3) Mustroph, H. Potential-Energy Surfaces, the Born–Oppenheimer Approximations, and the Franck–Condon Principle: Back to the Roots. *ChemPhysChem* **2016**, 2616–2629. https://doi.org/10.1002/cphc.201600243.

(4) Giacomo, F. Di. A Short Account of RRKM Theory of Unimolecular Reactions and of Marcus Theory of Electron Transfer in a Historical Perspective. *J. Chem. Educ.* **2014**, *92* (3), 476–481. https://doi.org/10.1021/ed5001312.

(5) Baer, T.; Mayer, P. M. Statistical Rice-Ramsperger-Kassel-Marcus Quasiequilibrium Theory Calculations in Mass. *J. Am. Soc. Mass Spectrom. 8* **1997**, *8*, 103–115. https://doi.org/10.1016/S1044-0305(96)00212-7.

(6) Hill, J. G. Gaussian Basis Sets for Molecular Applications. *Int. J. Quantum Chem.* **2013**, *113*, 21–34. https://doi.org/10.1002/qua.24355.

(7) Amusia, M. Y.; Msezane, A. Z.; Shaginyan, V. R. Density Functional Theory versus the Hartree – Fock Method : Comparative Assessment. *Phys. Scr.* **2003**, *68* (6), 133–140. https://doi.org/10.1238/Physica.Regular.068aC0133.

(8) Clementi, E.; Davis, D. . Electronic Structure of Large Molecular Systems. *J. Comput.*

Phys. **1966**, *1* (2), 223–244. https://doi.org/10.1016/0021-9991(66)90004-0.

(9) Tirado-rives, J.; Jorgensen, W. L. Performance of B3LYP Density Functional Methods for a Large Set of Organic Molecules. *J. Chem. Theory Comput.* **2008**, *4* (2), 297–306. https://doi.org/10.1021/ct700248k.

(10) Paier, J.; Marsman, M.; Kresse, G. Why Does the B3LYP Hybrid Functional Fail for Metals? *J. Chem. Phys.* **2007**, *127* (2), 024103. https://doi.org/10.1063/1.2747249.

(11) Gill, P. M. W.; Johnson, B. G.; Pople, J. A.; Frisch, M. J. The Performance of the Becke-Lee-Yang-Parr with Various Basis Sets (B-LYP) Density Functional Theory. *Chem. Phys. Lett.* **1992**, *197* (4–5), 499–505. https://doi.org/10.1016/0009-2614(92)85807-M.

(12) Wiberg, K. B. Basis Set Effects on Calculated Geometries : 6-311++ G ** vs . Aug-Cc-PVDZ. *J. Comput. Chem.* **2004**, *25* (11), 1342–1346. https://doi.org/10.1002/jcc.20058.

(13) Pokon, E. K.; Liptak, M. D.; Feldgus, S.; Shields, G. C. Comparison of CBS-QB3 , CBS-APNO , and G3 Predictions of Gas Phase Deprotonation Data. *J. Phys. Chem. A* **2001**, *105* (45), 10483–10487. https://doi.org/10.1021/jp012920p.

Chapter 3: Determining the Unimolecular Breakdown Products of Short Deprotonated Per- and Poly-Fluorinated Acids and Alcohols

3.1. Published Contributions

A. Radnoff, S. Charpentier-St-Pierre, and P. Mayer, " On the Unimolecular Breakdown Products of Short Deprotonated Per- and Poly-Fluorinated Acids and Alcohols," *Journal of Mass Spectrometry* 60, no. 10 (2025): e5175, https://doi.org/10.1002/jms.5175.

Department of Chemistry and Biomolecular Sciences, University of Ottawa, Ottawa K1N 6N5, Canada

3.2. Abstract

The strong C−F bond found in per- and poly-fluorinated alkyl substances (PFAS) makes them resistant to degradation and thus persistent in the environment. One of the most common methods for quantifying PFAS in environmental matrices is to use tandem mass spectrometry. However, the dissociation of ions made by deprotonating PFAS alcohols and acids has only been qualitatively explored. In this study, we investigated the breakdown of deprotonated 2,2,3,3,3-pentafluoropropionic acid (**1**, m/z 163), 3,3,3-trifluoropropionic acid (**2**, m/z 127), 2,2,3,3,3-pentafluoro-1-propanol (**3**, m/z 149), 3,3,3-trifluoro-1-propanol (**4**, m/z 113), and trifluoromethanesulfonic acid (**5**) by energy-resolved collision-induced dissociation (CID) tandem mass spectrometry and density functional theory (B3LYP/6-311+G(d,p)). **1** loses CO_2 at low lab-frame collision energy. **2** also loses CO_2 to form the 1,1,1-trifluoroethane ion (m/z 83) and 1,2-difluoroethylene to form FCO_2^- (m/z 63). RRKM calculations for the two reactions show that m/z 83 has a higher entropy of activation driving its formation. **3** undergoes the loss of CH_2O to form the pentafluoroethyl anion (m/z 119) and the loss of HF to form $CF_2CF_2COH^-$ (m/z 129). **4** produced four fragment ions with two primary reactions making CF_3CHCH^- (m/z 95) + H_2O and $CF_2CHCOH_2^-$ (m/z 93) + HF, which go on to dissociate further to produce CF_3^- (m/z 69) + HCCH

+ H_2O and CF_2CH^- (m/z 63) + CH_2O + HF. At low collision energy, m/z 95 dominates due to a lower energy transition state, but as internal energy increases, m/z 93 takes over as its transition state has a more favourable entropy. **5** produced FSO_3^- (m/z 99), SO_3^- (m/z 80), and CF_3^- (m/z 69). SO_3^- was the most abundant fragment due to its higher electron affinity.

3.3. Introduction

Per- and poly-fluoroalkyls substances, PFAS, are compounds that have been used in many products, including nonstick coatings, water-resistant clothes, and food packaging.[1] The C–F bond found in PFAS is strong and resistant to degradation in the environment, which can lead to bioaccumulation.[1] PFAS are a diverse class of compounds that vary in their carbon backbone as well as functional groups. The acidic functional groups can be sulfonic, carboxylic, and phosphonic acids. Recently, shorter chain PFAS have been introduced to prevent bioaccumulation, but recent studies show that these shorter chain PFAS are just as toxic and very mobile in the environment.[2] These shorter-chain PFAS are also harder to detect and therefore make their removal challenging.[2]

PFAS with acidic head groups, like carboxylic and sulfonic acids, are usually analyzed by liquid chromatography-tandem mass spectrometry (LC-MS/MS) in negative mode.[3] The mechanisms for the formation of the observed fragment ions in MS/MS experiments have not been explored in detail (but more recently, the dissociation of deprotonated tri- and penta-fluoropropionic acid ions has been investigated).[4] To investigate these pathways, five short-chain PFAS: 2,2,3,3,3-pentafluoropropionic acid (**1**H), 3,3,3-trifluoropropionic acid (**2**H), 2,2,3,3,3-pentafluoro-1-propanol (**3**H), 3,3,3-trifluoro-1-propanol (**4**H), and trifluoromethanesulfonic acid (**5**H) were

selected. Their deprotonated forms are shown in Figure 23. The unimolecular chemistry of each of these deprotonated ions was explored with tandem mass spectrometry and theory.

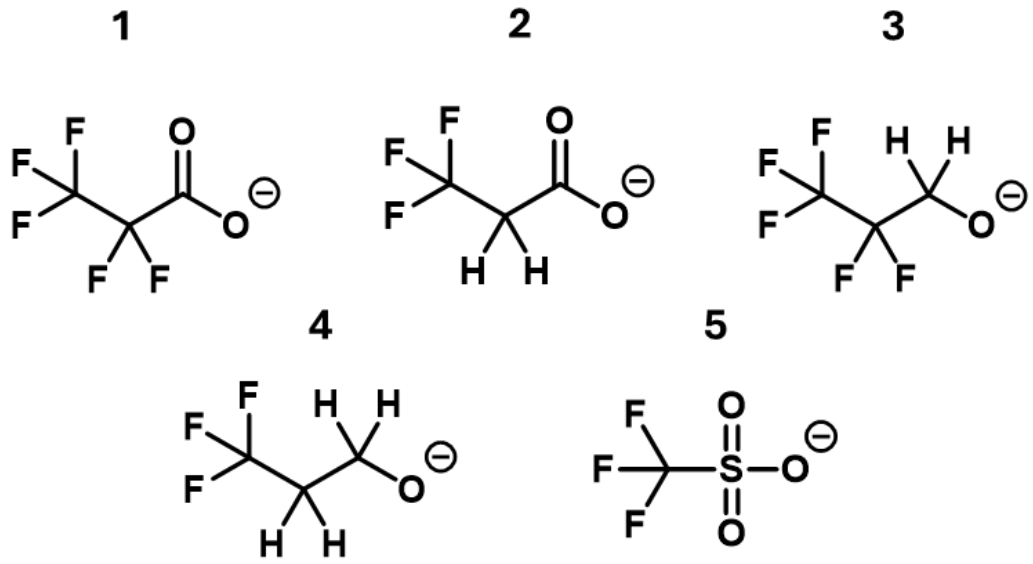

Figure 23: The deprotonated anions of the five short-chain PFAS 2,2,3,3,3-pentafluoropropionic acid (**1**), 3,3,3-trifluoropropionic acid (**2**), 2,2,3,3,3-pentafluoro-1-propanol (**3**), 3,3,3-trifluoro-1-propanol (**4**), and trifluoromethanesulfonic acid (**5**).

3.4. Methods

3.4.1. Mass Spectrometer Method

2,2,3,3,3-Pentafluoropropionic acid (97%, Sigma-Aldrich, Oakville, Ontario, CA), 3,3,3-trifluoropropionic acid (98%, Sigma-Aldrich, Oakville, Ontario, CA), 2,2,3,3,3-pentafluoro-1-propanol (97%, Sigma-Aldrich, Oakville, Ontario, CA), 3,3,3-trifluoro-1-propanol (Sigma-Aldrich, Oakville, Ontario, CA) and trifluoromethanesulfonic acid (Reagent grade, 98%, Sigma-Aldrich, Oakville, Ontario, CA) were purchased and prepared in five individual solutions at a concentration of 1 ppm with a mixture of 9:1 water (Optima, ≥99.9%, Fisher Scientific, Fair Lawn, NJ, USA), and methanol (Optima, Fisher Scientific, Fair Lawn, NJ, USA). Product ion scans were

performed on a Micromass Quattro Ultima triple quadrupole mass spectrometer with a Z-Spray ion source and the MassLynx operating software. The samples were introduced into the electrospray ionization (ESI) source using a syringe pump with a flow rate of ~ 30 μL/min. The desolvation gas used was nitrogen (244 L/h), the collision gas was argon, and all solutions were analyzed in negative ion mode. The source and desolvation temperatures were 100ºC and 150ºC, respectively. For each compound, the collision energy was varied from 0-30 eV (E_{lab}). Breakdown curves were generated by plotting the relative abundance of precursor and fragment ions as a function of centre-of-mass collision energy, which was derived from the lab-frame collision energy by equation 1.

$$E_{com} = \left(\frac{m_{Ar}}{m_{Ar}+m_{PFAS}}\right) E_{lab} \qquad (3.1)$$

Where m_{Ar} and m_{PFAS} are the masses of argon and the ion in question.

3.4.2. Computational Calculations

Optimized structures (minima and transition states) and vibrational frequencies were obtained using the B3LYP/6-311+G(d,p) level of density functional theory (DFT)[5] with the Gaussian 16 suite of programs.[6] Transition states were confirmed with the intrinsic reaction coordinate method.[6] Rice-Ramsperger-Kassel-Marcus (RRKM) theory was used to determine the microcanonical rate constants, *k(E)*, of the unimolecular reactions using the following equation.[7,8]

$$k(E) = \frac{\sigma N^{\ddagger}(E - E_0)}{hp(E)}$$

where σ is the reaction degeneracy, h is Planck's constant, E_0 is the 0 K activation energy of the reaction, $N^{\ddagger}$ is the number of vibrational states for the transition state, and $p(E)$ the density of

vibrational states for the reactant, both calculated using the Beyer and Swinhart direct count algorithm.[9]

3.5. Results and Discussion

The breakdown diagrams and representative CID mass spectra for ions **1**-**5** are shown in Figure 24. **1** was found to lose only 44 Da, corresponding to CO_2, forming the $CF_3CF_2^-$ anion (m/z 119), Figure 24A. The modest E_{com} for this process is consistent with the facile loss of CO_2 found from thermal degradation studies of perfluorooctanoic acid.[1] **2** had two breakdown products, m/z 83 and m/z 63 (Figure 24B). The former is loss of CO_2 to form $CF_3CH_2^-$, while m/z 63 is FCO_2^- (loss of CF_2CH_2). Alternatively, m/z 63 could result from HF loss from m/z 83, but the breakdown diagram is not consistent with a sequential reaction, but rather two competing parallel reactions from the precursor ion having similar energy onsets. The relative abundance of the two channels is reversed from that found by Lee et al.[4] presumably due to a different collision energy regime.

3 forms a major product with m/z 119, but there is a discernible signal with m/z 129 in the spectra (Figure 24C). The fragment ion with m/z 119 can only be the $CF_3CF_2^-$ anion, resulting from the loss of formaldehyde (CH_2O) from the precursor ion, while m/z 129 must be due to loss of HF. Interestingly, the production of CH_2O from neutral PFAS has also been found in the gas phase kinetics literature.[10] **4** produces the most complex unimolecular behaviour featuring four fragment ions with m/z 95, 93, 69 and 63 (Figure 24D). Loss of water can lead to CF_3CHCH^- (m/z 95) and loss of HF to $CF_2CHCOH_2^-$ (m/z 93). CF_3^- (m/z 69) and CF_2CH^- (m/z 63) appear to be sequential reaction products (based on their higher onset energies) that likely originate by loss of C_2H_2 from m/z 95 and CH_2O from m/z 93. **5** formed FSO_3^- (m/z 99), SO_3^- (m/z 80), and CF_3^- (m/z 69)

(Figure 24E). The removal of SO_3 has also been shown from perfluorooctane sulfonate due to an oxidation breakdown method.[1]

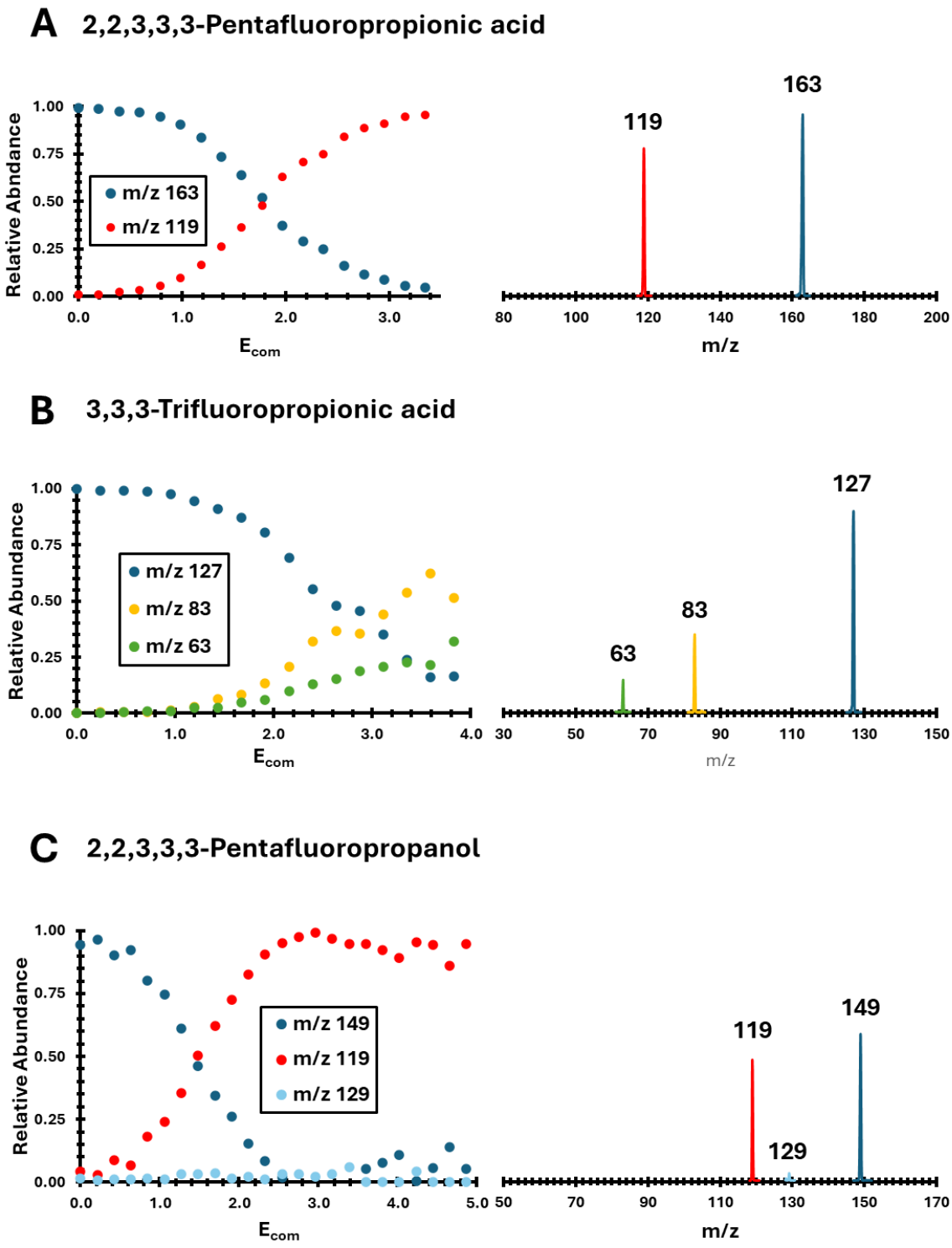

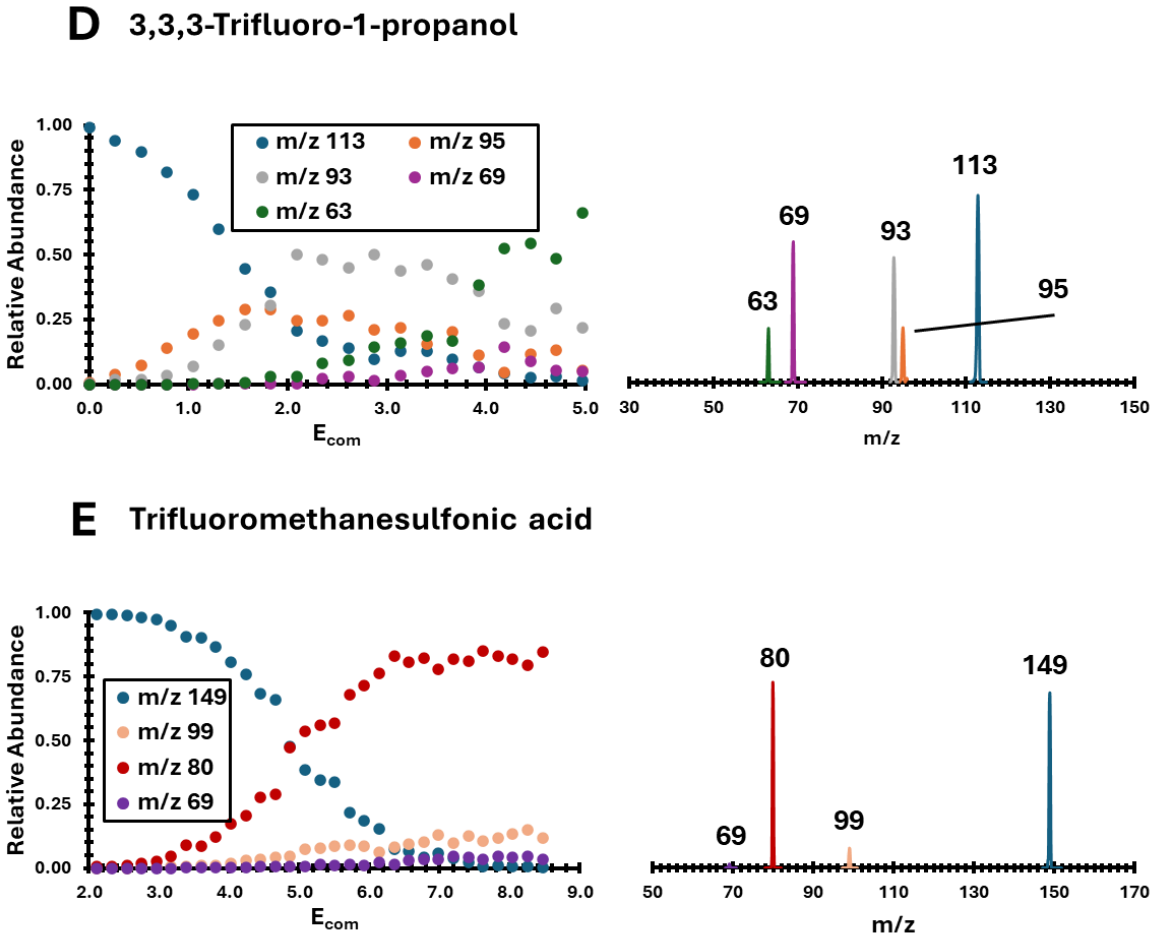

Figure 24: Breakdown curves and representative mass spectra for 1 - 5. The representative mass spectra were acquired at E_{lab}=9 eV (A), E_{lab}=10 eV (B), E_{lab}=7 eV (C), E_{lab}=11 eV (D), E_{lab}=24 eV (E).

Each of these systems has been computationally explored to derive minimum energy reaction pathways (MERPs). The reaction pathway for the loss of CO_2 from **1** (Figure 25) shows a reaction with no reverse barrier and an endothermicity of 1.39 eV.

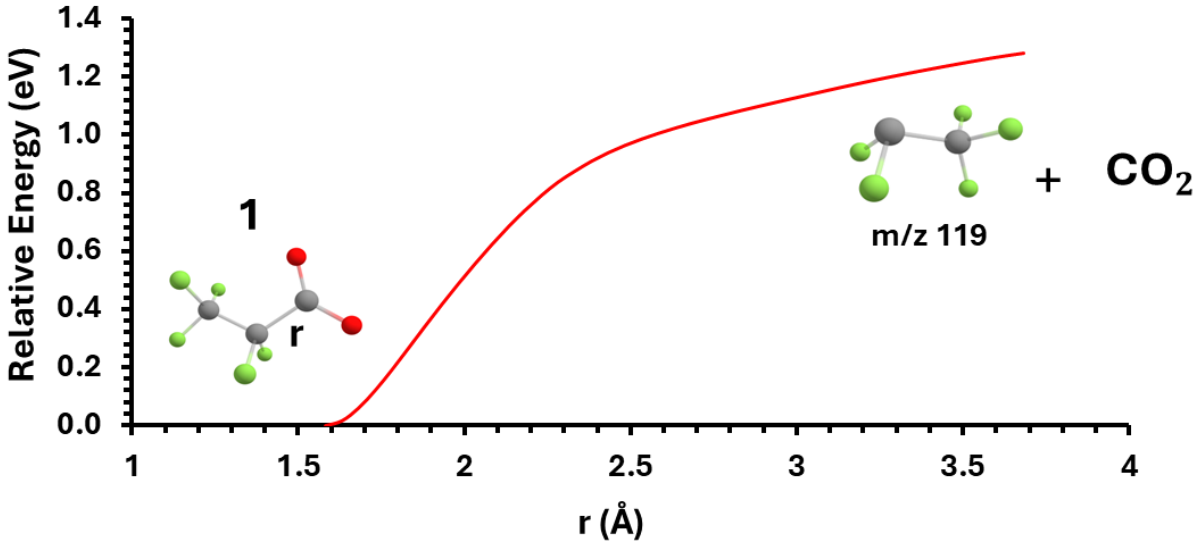

Figure 25: Energy pathway showing the dissociation of 1 into CO_2 and the pentafluoroethyl anion.

The calculated MERPs for **2** are shown in Figure 26. Again, loss of CO_2 was found to have no reverse energy barrier, and the calculated threshold was 1.49 eV. The assignment of m/z 63 to FCO_2^- is supported by the competitive reaction leading to F-transfer, Figure 26, and previous IRMPD experiments.[4] The sequential loss of HF from m/z 83 is too high in energy (Figure 26). The competition between forming m/z 83 and m/z 63 is governed by their relative activation entropies ($\Delta^{\ddagger}S$ (m/z 83) = 64 J K^{-1} mol^{-1} compared to 32 J K^{-1} mol^{-1} for m/z 63), Figure 26B. Lee et al. employed a linear ion trap and found m/z 63 to be the dominant fragment ion,[4] which is only consistent with their experiment accessing lower internal energy ions than the current one.

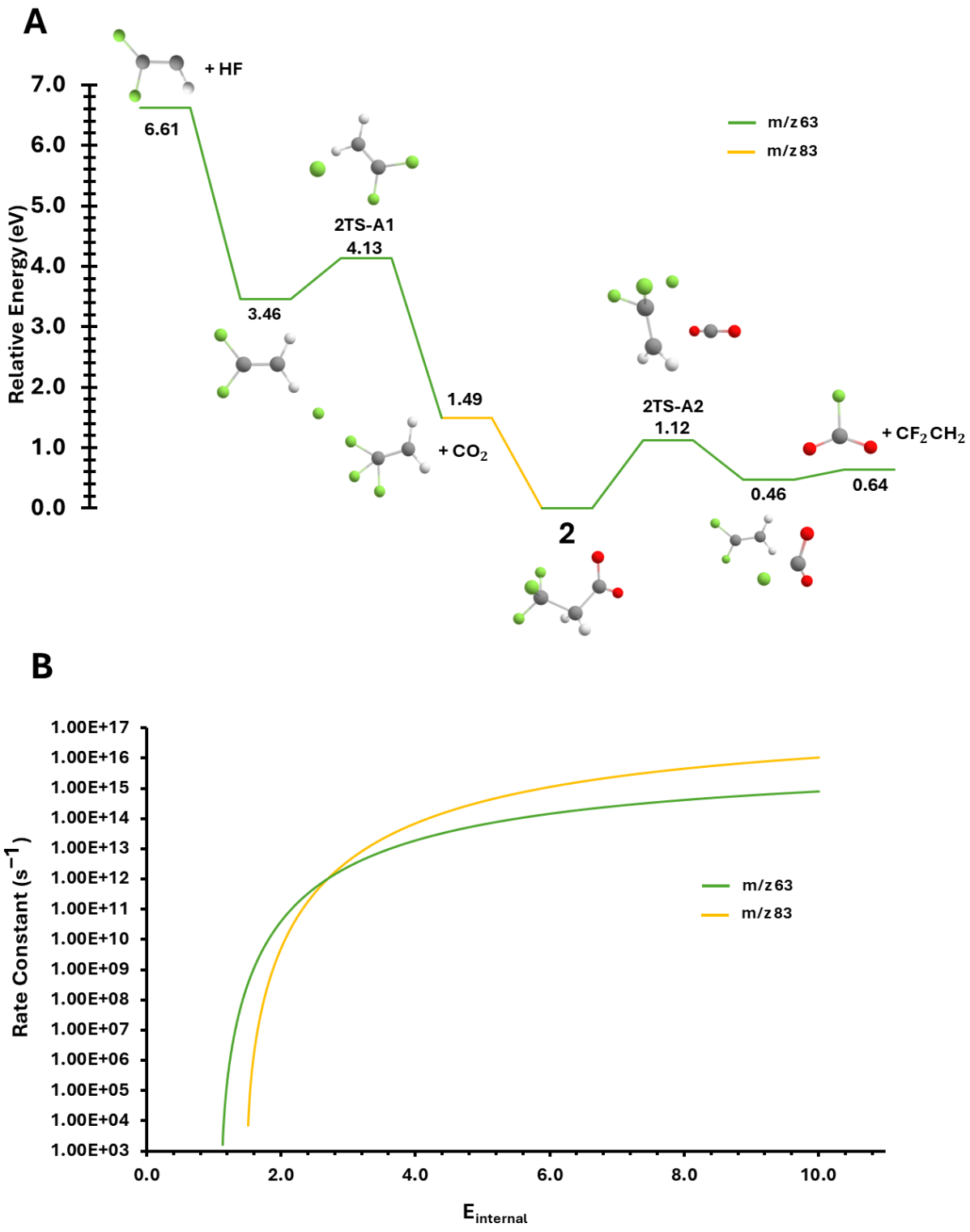

Figure 26: A) Minimum energy reaction pathway for the dissociation of **2** and B) the RRKM *k*(E) vs *E* curves for forming m/z 63 and m/z 83. The greater $\Delta^{\ddagger}S$ for m/z 83 means this channel becomes predominant with increasing internal (and thus collision) energy.

3 loses HF in a minor process to form CF_3CFCHO^- (m/z 129) and CH_2O to form $CF_3CF_2^-$ (m/z 119), Figure 27, the dominant product observed in Figure 24C. The lower energy HF-loss products are formed over the high-energy transition state 3TS-A1.

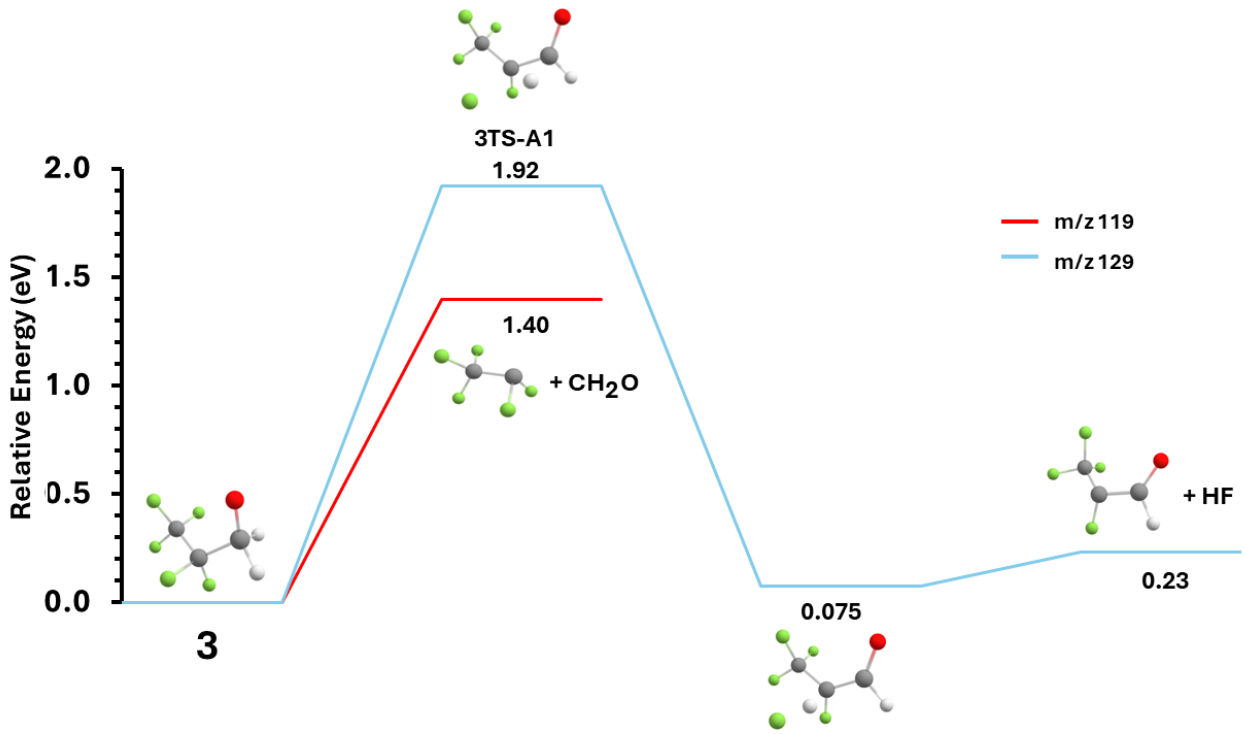

Figure 27: Energy pathway showing the dissociation of **3**.

The MERPs for **4** are shown in Figure 28. Water loss to form m/z 95 (Figure 28B, orange) is preceded by a 1,3-H transfer to the O atom, followed by a 1,2-H shift leading to H_2O. Competing with this reaction at low E_{com} is HF loss (making m/z 93), Figure 28A (grey). The fact that m/z 95 and 93 are formed competitively, but with m/z 95 at a higher abundance at lower collision energy, is due to the lower relative energy of 4TS-B1. 4TS-A1 is less entropically hindered, though, so as internal energy increases, the rate constant for forming m/z 93 outcompetes that for m/z 95, and the former ion becomes the dominant reaction observed in the CID BD.

Subsequent reaction can form CF_3^- (m/z 69) + C_2H_2 (Figure 28B, purple) from m/z 95. CF_2CH^- (m/z 63) can be formed by CH_2O loss from m/z 93 (Figure 28A, green).

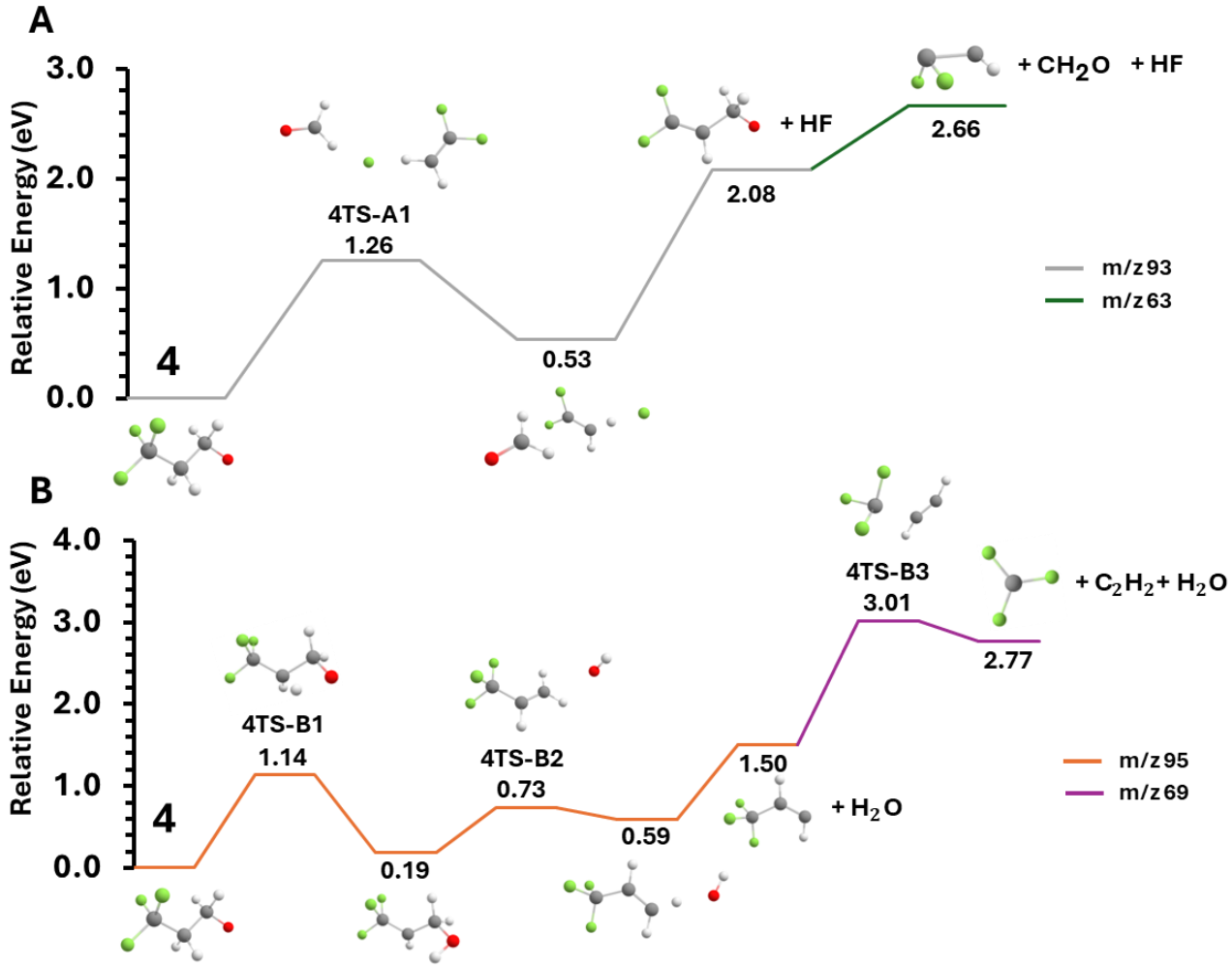

Figure 28: Energy pathways showing the dissociation of **4**.

5 formed FSO_3^- (m/z 99), SO_3^- (m/z 80), and CF_3^- (m/z 69), Figure 29, all requiring ~ 3 eV or greater to be formed, which is consistent with the higher E_{com} needed to observe these reactions compared to the other four precursor ions (Figure 24E). SO_3^- (m/z 80) and CF_3^- (m/z 69) represent the same bond cleavage reaction, with the charge preferentially residing on the product with higher electron affinity (2.064 eV[11] for $SO_3^{\bullet}$ and 1.82 eV[13] for $CF_3^{\bullet}$). FSO_3^- (m/z 99) is also observed in

low abundance, due to the lower $\Delta^{\ddagger}S$ for this reaction caused by the F-transfer transition state 5TS-B1.

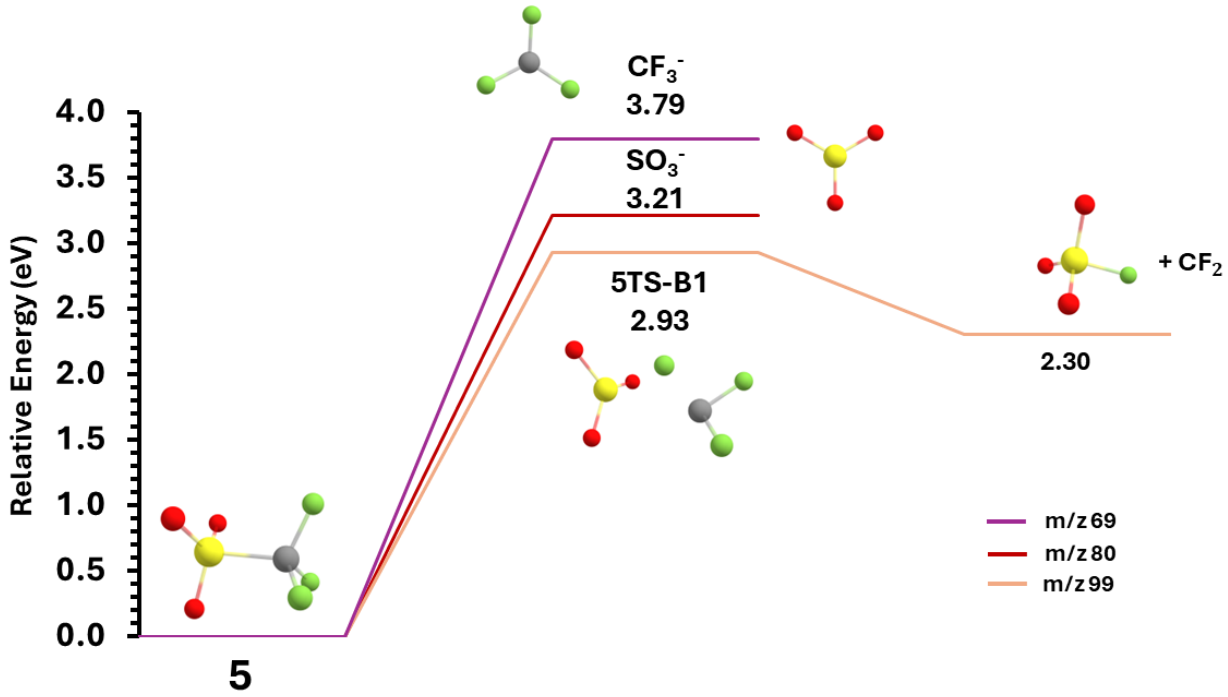

Figure 29: Energy pathway showing the dissociation of **5**.

3.6. Conclusions

The four oxygenated PFAS anions **1**-**4** exhibited the reactions of CO_2, HF, and CH_2O loss, similar to what has been observed in the thermal degradation of such species.[1,12] There was qualitative agreement between the observed E_{com} onset energies for fragmentation of the ions and the corresponding calculated energy requirements. For the acids, increasing hydrogen content increased the number of competing reactions beyond simple CO_2 loss. This was also true for the alcohols, with the pentafluorinated **3** primarily losing formaldehyde, whereas the trifluorinated **4** exhibited two major dissociation channels, producing HF and water. Thus, it may be possible to

gain insight into thermal degradation processes and products of PFAS by examining the tandem mass spectra of the corresponding anions.

3.7. References

(1) Etz, B. D.; Shukla, M. K. Per- and Polyfluoroalkyl Substances Chemical Degradation Strategies: Insights into the Underlying Reaction Mechanisms. *Curr. Opin. Chem. Eng.* **2023**, *42*, 100956. https://doi.org/10.1016/j.coche.2023.100956.

(2) Rehman, A. U.; Crimi, M.; Andreescu, S. Current and Emerging Analytical Techniques for the Determination of PFAS in Environmental Samples. *Trends Environ. Anal. Chem.* **2023**, *37* (e00198), e00198. https://doi.org/10.1016/j.teac.2023.e00198.

(3) Stramenga, A.; Tavoloni, T.; Stecconi, T.; Galarini, R.; Giannotti, M.; Siracusa, M.; Ciriaci, M.; Bacchiocchi, S.; Piersanti, A. Perfluoroalkyl and Polyfluoroalkyl Substances (PFASs): An Optimized LC-MS/MS Procedure for Feed Analysis. *J. Chromatogr. B Anal. Technol. Biomed. Life Sci.* **2021**, *1186* (July), 123009. https://doi.org/10.1016/j.jchromb.2021.123009.

(4) Lee, A. E.; Featherstone, J.; Martens, J.; McMahon, T. B.; Hopkins, W. S. Fluorinated Propionic Acids Unmasked: Puzzling Fragmentation Phenomena of the Deprotonated Species. *J. Phys. Chem. Lett.* **2024**, *15* (11), 3029–3036. https://doi.org/10.1021/acs.jpclett.3c03400.

(5) Lee, C.; Yang, W.; Parr, R. G. Development of the Colic-Salvetti Correlation-Energy Formula into a Functional of the Electron Density. *Phys. Rev. B* **1988**, *37* (2), 785–789. https://doi.org/10.1103/PhysRevB.37.785?_gl=1*1f4d6wj*_gcl_au*MTI4NDIxMjA4OC4xNzM2Njk3NjU3*_ga*MTQzNjI2MzY0MC4xNzM2Njk3NjU2*_ga_ZS5V2B2DR1*MTczNjcwMzQ3MS4yLjEuMTczNjcwMzk5MS42MC4wLjQ4NzY0MTEwMQ..

(6) Frisch, M. J.; Trucks, G. W.; Schlegel, H. B.; Scuseria, G. E.; Robb, M. A.; Cheeseman, J.

R.; Scalmani, G.; Barone, V.; Petersson, G. A.; Nakatsuji, H.; Li, X.; Caricato, M.; Marenich, A. V.; Bloino, J.; Janesko, B. G.; Gomperts, R.; Mennucci, B.; Hratchian, H. P.; Ortiz, J. V.; Izmaylov, A. F.; Sonnenberg, J. L.; Williams-Young, D.; Ding, F.; Lipparini, F.; Egidi, F.; Goings, J.; Peng, B.; Petrone, A.; Henderson, T.; Ranasinghe, D.; Zakrzewski, V. G.; Gao, J.; Rega, N.; Zheng, G.; Liang, W.; Hada, M.; Ehara, M.; Toyota, K.; Fukuda, R.; Hasegawa, J.; Ishida, M.; Nakajima, T.; Honda, Y.; Kitao, O.; Nakai, H.; Vreven, T.; Throssell, K.; Montgomery, J. A., Jr.; Peralta, J. E.; Ogliaro, F.; Bearpark, M. J.; Heyd, J. J.; Brothers, E. N.; Kudin, K. N.; Staroverov, V. N.; Keith, T. A.; Kobayashi, R.; Normand, J.; Raghavachari, K.; Rendell, A. P.; Burant, J. C.; Iyengar, S. S.; Tomasi, J.; Cossi, M.; Millam, J. M.; Klene, M.; Adamo, C.; Cammi, R.; Ochterski, J. W.; Martin, R. L.; Morokuma, K.; Farkas, O.; Foresman, J. B.; Fox, D. J. GAUSSIAN 16 *Gaussian Inc.* Wallingford CT 2016.

(7) Baer, T.; Mayer, P. M. Statistical Rice-Ramsperger-Kassel-Marcus Quasiequilibrium Theory Calculations in Mass Spectrometry. *J. Am. Soc. Mass Spectrom.* **1997**, *8* (2), 103–115. https://doi.org/https://doi.org/10.1016/S1044-0305(96)00212-7.

(8) Baer, T.; Hase, W. L. *Unimolecular Reaction Dynamics: Theory and Experiments*; Oxford University Press on Demand: New York, 1996.

(9) Beyer, T.; Swinehart, D. F. Algorithm 448: Number of Multiply-Restricted Partitions. *Commun. ACM* **1973**, *16* (6), 379. https://doi.org/10.1145/362248.362275.

(10) Joudan, S.; Orlando, J. J.; Tyndall, G. S.; Furlani, T. C.; Young, C. J.; Mabury, S. A. Atmospheric Fate of a New Polyfluoroalkyl Building Block, C3F7OCHFCF2SCH2CH2OH. *Environ. Sci. Technol.* **2022**, *56* (10), 6027–6035.

https://doi.org/10.1021/acs.est.0c07584.

(11) Rudny, E. B.; Sidorov, L. N.; Voyk, O. M. Heterolytic Dissociation of Potassium Sulfate in the Gas Phase and Heats of Formation for Trioxosulfate(1-), Tetraoxosulfate(1-), and Potassium Sulfate(KSO4-) Ions. *High Temp.* **1985**, *23*, 238.

(12) Deyerl, H.; Alconcel, L. S.; Continetti, R. E. Photodetachment Imaging Studies of the Electron Affinity of CF3. *J. Phys. Chem. A* **2001**, *105* (3), 552–557. https://doi.org/10.1021/jp003137k.

Chapter 4: Determination of the pyrolysis products and decomposition mechanisms of per/polyfluorinated compounds using imaging photoelectron photoion coincidence spectroscopy (iPEPICO)

4.1. Published Contributions

Angela S. Radnoff,[a] Maxi Burgos Paci,[b] Andras Bodi[c] and Paul M. Mayer[a*]

[a] Department of Chemistry and Biomolecular Sciences, University of Ottawa, Ottawa, Canada K1N 6N5
[b] INFIQC – CONICET, Departamento fisicoquímica, Universidad Nacional de Córdoba, Córdoba, Argentina
[c] Laboratory for Synchrotron Radiation and Femtochemistry, Paul Scherrer Institute, 5232 Villigen, Switzerland

4.2. Abstract

To remove per- and polyfluorinated compounds (PFCs) from the environment, thermal treatment is often preferred, but incomplete degradation occurs. This creates small, volatile fluorinated compounds that can impact the environment. To investigate this, we employed a Chen-type microreactor and imaging photoelectron photoion coincidence spectroscopy to explore the pyrolysis of three short-chain PFCs, 2,2,3,3,3-pentafluoropropionic acid (**1**), 3,3,3-trifluoropropionic acid (**2**), and 2,2,3,3,3-pentafluoro-1-propanol (**3**). The products were ionized with VUV synchrotron radiation at the Swiss Light Source and identified by their mass-selected threshold photoelectron spectra (ms-TPES). The results are compared to literature photoelectron spectra and calculated TPES from Franck-Condon simulations performed at the B3LYP/6-311+G(d,p) level of theory. Thermal degradation leads off with HF loss (CO_2 loss competes at high internal energy) (**1**,**2**) and formaldehyde loss (**3**). These result in fluoroethenes, which themselves decompose to form CF_2. There was evidence for bimolecular processes that form formaldehyde from **1** and **2**, and acetylene from **3**.

4.3. Introduction

Per- and polyfluorinated substances (PFAS) have been produced since the 1950s and are used in a variety of products, including non-stick cookware, firefighting foams, and paint additives. They contain fluorinated alkyl chains, which are hydrophobic, and often a hydrophilic terminus, such as a carboxyl or sulfonate group. The C−F bond has a high dissociation energy, making these molecules resistant to environmental degradation. Many traditional waste removal treatment methods are ineffective in removing PFAS.[1,2] Thermal degradation can break the strong C−F bond present in PFAS, but can lead to persistent, smaller perfluorinated products.[3] Khan et al.[4] have shown that pyrolysis of the commonly used perfluorinated octanoic acid (PFOA) initiates with HF loss via two different pathways to form perfluoro-hexyl-2-oxiranone and perfluoro-1-heptene. It also loses CO_2 and FCO_2H in two separate pathways.[4] A pyrolysis study of perfluoropentanoic acid (PFPeA) [5] generated a variety of products including HF, CF_2, CF_3, C_2F_5, CO_2, C_2F_4, and CF_3H. This study also found that the product distribution changes with temperature. For example, between 800-850 K, PFPeA lost HF followed by CO. As the temperature increased, CO_2 and CF_2 formation also increased. At temperatures above 1200 K, products like C_2F_4, CF_4, and CHF_3 became significant.[5]

Since short-chain PFAS are replacing long-chain PFAS, recent research is investigating how they thermally degrade as well. In one study, Alinezhad and co-workers[6] heated perfluoroalkyl ether carboxylic acids (PFECAs) and short-chain perfluoroalkyl carboxylic acids adsorbed onto granular activated carbon (GAC) up to 500 ^oC. They found that the PFECAs degraded into short-chain fluorinated compounds like perfluorobutanoic acid (PFBA), trifluoroacetic acid (TFA), and perfluoropropionic acid (PFPrA). These compounds resulted from the scission of weak C−C bonds followed by F-atom loss. Short-chain perfluoroalkyl carboxylic acids degraded by similar cleavage

reactions.[6] We recently studied the pyrolysis of TFA and trifluoroacetic anhydride (TFAN) and identified the products CO, CO_2, CF_2, and CF_2O (and CF_3 for TFAN), and calculated the reaction pathways for their formation.[7] This study will focus on the pyrolytic degradation of three short-chain perfluorinated compounds, 2,2,3,3,3-pentafluoropropionic acid (**1**), 3,3,3-trifluoropropionic acid (**2**), and 2,2,3,3,3-pentafluoro-1-propanol (**3**), Figure 30. The work is carried out with a Chen-type microreactor on the VUV beamline of the Swiss Light Source synchrotron facility, and fills a gap between long-chain acids and TFA.

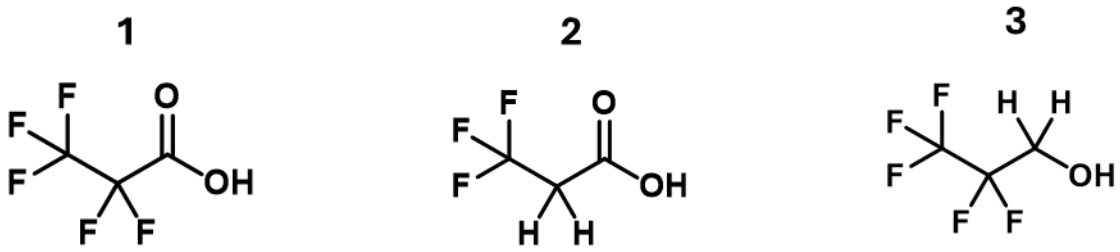

Figure 30: The three short-chain PFAS used were 2,2,3,3,3-pentafluoropropionic acid (**1**), 3,3,3-trifluoropropionic acid (**2**), and 2,2,3,3,3-pentafluoro-1-propanol (**3**).

4.4. Experimental Methods

4.4.1. iPEPICO

2,2,3,3,3-Pentafluoropropionic acid (97%, Sigma-Aldrich, Oakville, Ontario, CA), 3,3,3-trifluoropropionic acid (98%, Sigma-Aldrich, Oakville, Ontario, CA), 2,2,3,3,3-pentafluoro-1-propanol (97%, Sigma-Aldrich, Oakville, Ontario, CA) were purchased and used without further purification. Imaging photoelectron photoion coincidence (iPEPICO) spectroscopy was performed at the Swiss Light Source (SLS, Paul Scherrer Institut, Villigen, Switzerland). The VUV beamline was used and described in previous literature.[8,9] The scheme that shows how the experimental data was collected has also been reported.[10] Pyrolysis was done using the high-temperature pyrolysis

microreactor for the endstation.[11] Synchrotron radiation with 5 meV resolution was dispersed using a 150 grooves per mm grating. A differentially pumped gas filter filled with 9 mbar of Ne:Ar mixture was used to filter the higher harmonics over a 10 cm optical length. The resulting monochromatic VUV radiation photoionizes molecules in a 2x2 mm^2 interaction region, and the photoions and photoelectrons produced were velocity-mapped on imaging RoentDek delay line detectors. Threshold photoelectrons (initially zero kinetic energy electrons) are detected at the center of the electron detector. Non-zero-kinetic-energy electrons (hot electrons) are only detected based on their off-axis momentum. Correction is made for hot electrons that hit the centre spot by subtracting the mass spectrum in coincidence with electrons in a ring around the centre.[12] Photoion mass-selected threshold photoelectron spectrum (ms-TPES) can then be created by plotting the peak intensity for each product m/z ratio as a function of photon energy.[13]

For the pyrolysis experiment, argon gas, at a pressure of 1 bar and with a flow rate of 1 standard cubic centimetres per minute (sccm), was passed over the sample vials containing the compounds, which were at room temperature. All three have a vapour pressure of approximately 4.5 kPa at 20ºC.[14] The sample mixture was diluted with 20 sccm of argon to produce a beam with about 0.22% of the sample. The sample stream passed through a 200 μm pinhole into a 3 cm long, 1 mm internal diameter SiC pyrolysis microreactor. The microreactor is heated, and its surface temperature can be measured using a type C thermocouple and calculated using equation (4.1):

$$T/^{o}C = P/W \times 14.268 + 303.18 \qquad (4.1)$$

where T is the reactor temperature and P is the heating power. The reactor temperature also represents the gas temperature inside the reactor within 100ºC.[15] The temperature used for the compounds in this research was between 800−1000ºC. The pressure in the reactor is between 10-40 mbar, and the time in the pyrolysis reactor is 100 μs.[15,16] The molecular beam leaving the

pyrolysis reactor passes through the 2 mm diameter skimmer into the detection chamber. Due to the low pre-expansion pressure at the reactor nozzle[15] there is a limited rovibrational cooling in the expansion of the microreactors.[17] The ionization signal that is detected is due to the cooled molecular beam and the collisional cooled compounds, which occurred in the ionization chamber. This causes an "effective temperature" which relates to the internal energy distribution of the sample.

Previous studies with these types of reactors suggest that the ratio of unimolecular vs. bimolecular reactions is molecule-dependent. Pyrolysis of 0.2% propionic acid in argon and 0.3% furfural in helium followed primarily unimolecular chemistry,[18,19] while benzaldehyde (at similar concentrations) displayed bimolecular chemistry,[18] as did acetone pyrolysis experiments.[20] Our previous work on the pyrolysis of alkyl and chloroformates did not show evidence of a significant amount of bimolecular reactions.[21,22]

We estimated the relative amounts of the observed products by normalizing the most intense peak in each ms-TPES with the measured photoionization cross-section. For those molecules not listed in the database,[23] the cross-sections for the fully-hydrogenated analogues were used, Table S2.

4.4.2 Computational Methods

Optimized structures (minima and transition states) and vibrational frequencies were obtained using the B3LYP/6-311+G(d,p) level of density functional theory (DFT)[24,25] in the Gaussian 16 suite of programs.[26] CBS-QB3 single-point energy calculations were also done to determine ionization energies. Transition states were confirmed with the intrinsic reaction coordinate method.[26] Franck–Condon simulations utilizing the double harmonic approximation

were calculated with Gaussian 16. Rice-Ramsperger-Kassel-Marcus (RRKM) theory was used to determine the *k(E)* for selected reactions using equation,[27,28]

$$k(E) = \frac{\sigma N^{\ddagger}(E - E_0)}{h\rho(E)}$$

where σ is the reaction degeneracy, h is Planck's constant, E_0 is the 0 K activation energy of the reaction, $N^{\ddagger}$ is the number of vibrational states for the transition state, and ρ the density of vibrational states for the reactant, both calculated using the Beyer and Swinhart direct count algorithm.[29]

4.5. Results and Discussion

2,2,3,3,3-Pentafluoropropionic acid (1)

We observed three pyrolysis products from **1** represented by their respective ms-TPES at *m/z* 64, 50, and 44, Figure 31. Based on ionization energies (Table S1) and Frank-Condon simulations, these represent the neutral pyrolysis products difluoroethylene, $C_2H_2F_2$ (64 Da),[30] difluoromethylene, CF_2 (50 Da),[31] and CO_2 (44 Da).[32] The ms-TPES for m/z 64 is best represented by the FC-simulation for 1,1-difluoroethene, but we cannot rule out a mixture of 1,1- and 1,2-difluoroethene. There was some limited evidence for the formation of fluoroformic acid, FCO_2H, also at *m/z* 64, but low statistics data do not lead to a definitive assignment (Figure S1).

We computationally explored four primary reactions from **1**, losses of HF (as commonly reported in the literature for PFAS acids), CO_2, and FCO_2H. The results are shown in Figure 32a. The lowest energy barrier is for HF loss at 2.39 eV, ultimately forming CF_2CF_2 after HF and CO_2 loss. CF_2CF_2 can then form CF_2. Competing with this reaction is the initial loss of CO_2, which forms CF_3CF_2H, but it was not observed in the iPEPICO data. In a TPEPICO study of CF_3CF_2H,

Zhou et al.[33] found that all valence states of the radical cation are dissociative, and it is not observed at any photon energy. Thus, we would not observe an ms-TPES for this neutral. Copeland et al.[34] explored the thermal decomposition of CF_3CF_2H from 600-1600ºC and found that at temperatures below 1000ºC, the dominant observed reactions are the formation of C_2F_4 + HF, followed by C_2F_4 breaking apart to form $2CF_2$ (Figure 32a). Above 1000ºC, the reaction forming CF_2 + CF_3H starts to compete, and as the temperature increases, CF_3H increases in abundance. Thus, at the temperatures of our current study (800-1000ºC), we expect the direct dissociation of CF_3CF_2H to CF_2 + CF_3H to be a minor process, with most of the pentafluoroethane formed by the initial loss of CO_2 going on to make C_2F_4, HF (beyond the photon energy range of the current experiment) and subsequently CF_2 (observed). This is also the dominant reaction found from high-pressure pyrolysis in a turbulent-flow reactor.[35] Both of these pathways ultimately lead at the same products of $2CF_2$, CO_2, and HF (Figure 32a). For comparison, the formation of CF_3CF and FCO_2H is also shown in Figure 3a, but the 3.47 eV transition state means it cannot compete with CO_2 loss and would at best be a very minor reaction (as evident from Figure S1). Since there is only one hydrogen atom in **1**, $C_2H_2F_2$ must be formed in bimolecular processes, presumably H-atom abstraction by $C_2F_2H^{\bullet}$ radicals.

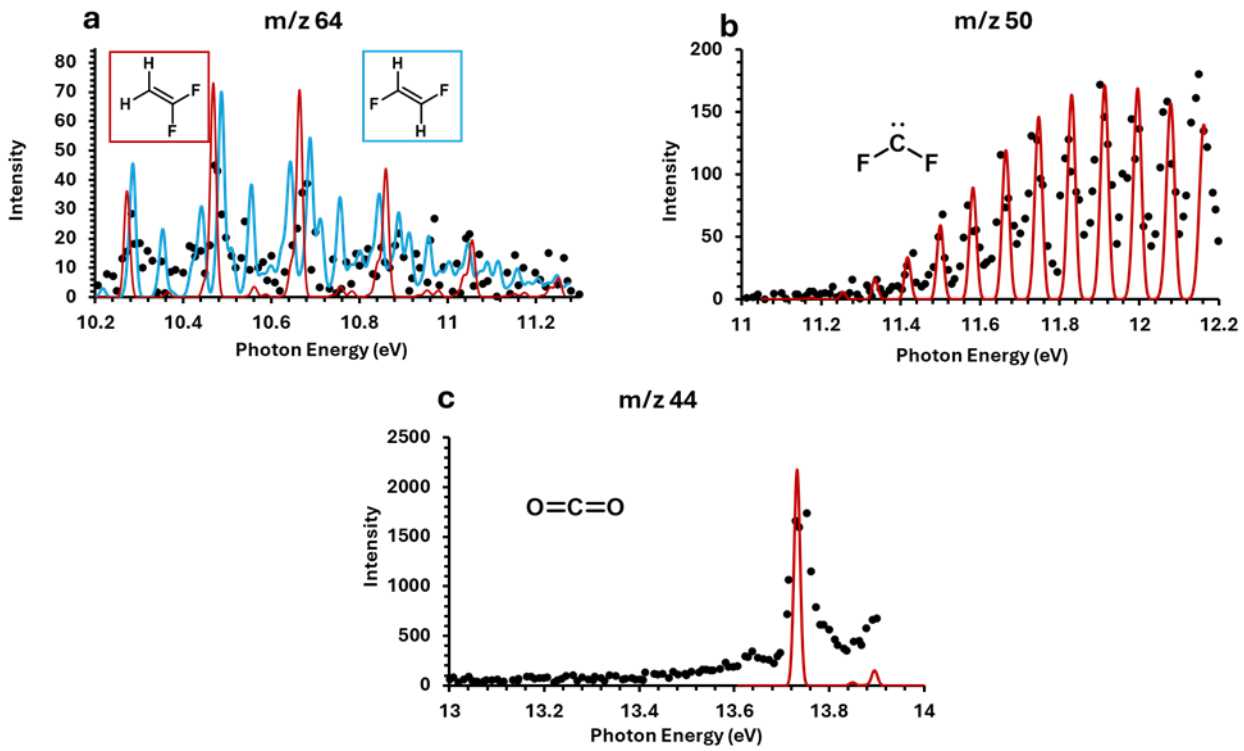

Figure 31: ms-TPES for the pyrolysis products of **1** (symbols) with overlaid Franck-Condon simulations (coloured lines).

We plotted the *k*(E) vs E curves for the first step leading out from **1** to each set of products (Figure 32b). Initial loss of HF is the kinetic winner at lower internal energies, with initial CO_2 loss starting to compete with this reaction above 10 eV due to a more favourable entropy of activation, $\Delta^{\ddagger}S$. Both reactions lead to CO_2 being formed below the initial transition state energies, which results in CO_2 being the main observed product, Table S2.

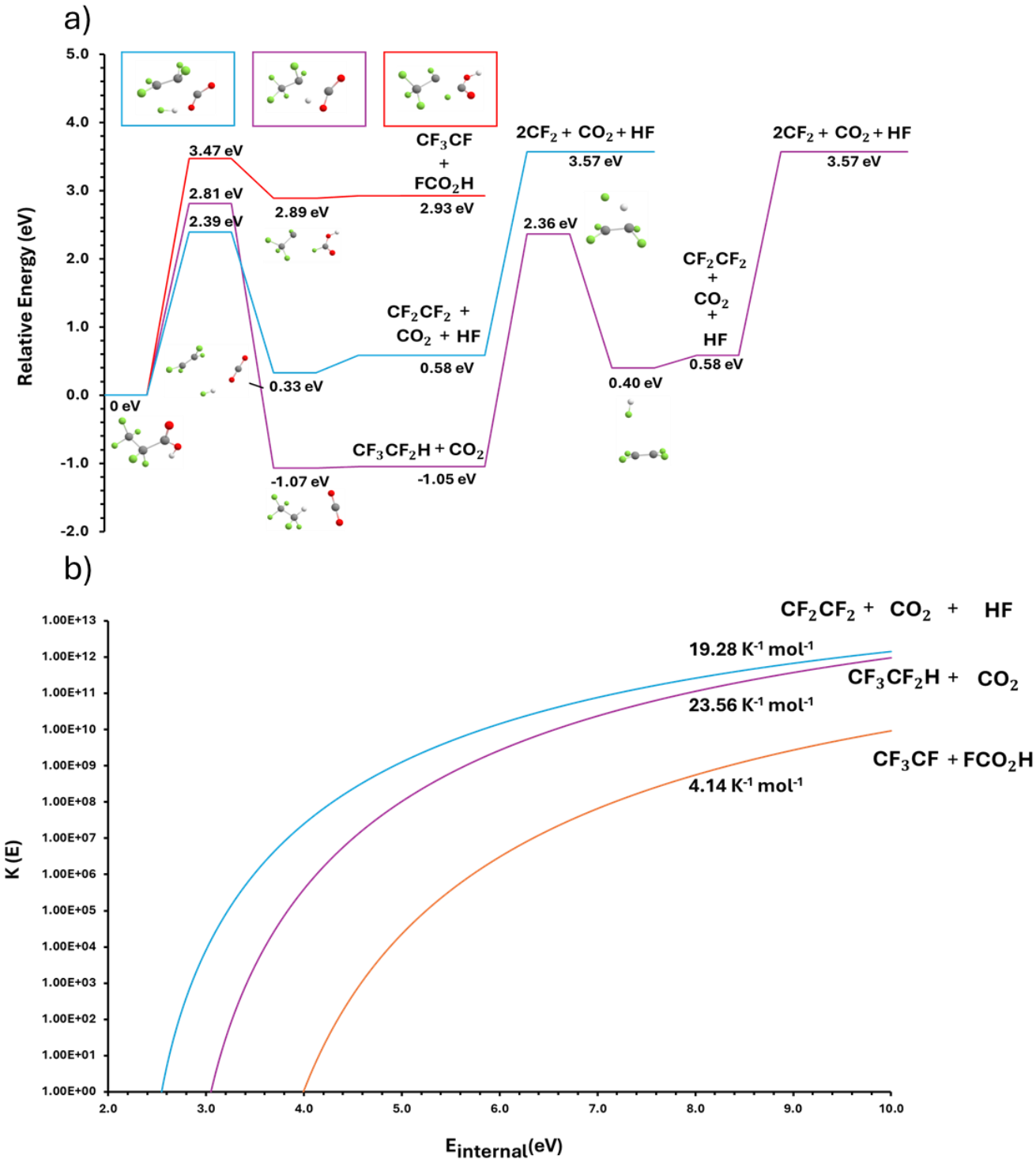

Figure 32*:* a) MERP of **1** showing the formation of CO_2, HF, CF_2CF_2, and FCO_2H, b) RRKM curve of **1** showing the competing reactions forming CO_2, HF, and FCO_2H. $\Delta^{\ddagger}S$ values for each reaction are shown.

On the Ionization of 2,2,3,3,3,-Pentafluoroethane

The formation of pentafluoroethane is a step in the MERP of **1,** but it does not have an ms-TPES in the pyrolysis data. The IE_a of CF_3CF_2H was measured by Copeland et al. to be 12.7 ± 0.05 eV, while the vertical value was determined to be 13.76 ± 0.05.[34] The IE_a value derived from the current B3LYP calculations is 13.22 eV, while CBS-QB3 gives a much lower value of 11.74 eV and a vertical value of 13.06 eV. Copeland et al.[34] calculated the adiabatic and vertical *IE* at 18 levels of theory and concluded that the best average IE_a is 12.26 ± 0.02 eV and IE_v = 14.051 ± 0.059 eV, both much higher than the current CBS-QB3 calculated values. Apparent from the spread in *IE* values is that it is difficult to observe the true adiabatic *IE*. Experimentally, the ion is not observed until above 12.7 eV, which is closer to the vertical value. Copeland et al.[34] calculated the structure of neutral and ionized CF_3CF_2H, and the largest geometry change is elongation of the C−C bond from 1.5 Å to over 2 Å upon ionization, and indeed the lowest energy ion dissociation reaction is cleavage of this bond to form $CF_2H^+ + {}^{\bullet}CF_3$.[34]

3,3,3-Trifluoropropionic acid (2)

We measured six ms-TPES for **2** at *m/z* 100, 64, 50, 44, 28 and 26 (Figure 33). Based on ionization energies (Table S1) and Frank-Condon simulations, these represent the neutral pyrolysis products of 2,2,2-trifluoroethanol (100 Da),[36] $C_2H_2F_2$ (64 Da),[30] CF_2 (50 Da),[31] CO_2 (44 Da),[32] CO (28 Da)[37] and HC≡CH (26 Da),[38] Figure 33. As with **1**, the ms-TPES of *m/z* 64 appears to be more consistent with CF_2=CH_2 than with CFH=CFH, but a mixture cannot be ruled out. CO_2 loss forms 1,1,1-trifluoroethane. While the photoelectron spectrum of trifluoroethane has been recorded,[39] we do not observe its ms-TPES (Figure S1) for the same reason we do not see the ms-TPES of pentafluoroethane; the valence states of the radical cation are dissociative.[40] 1,1,1-Trifluoroethane

was observed to lose HF upon pyrolysis to form 1,1-difluoroethene,[41] which goes on to form CF_2.[42] Alternatively, like with **1**, an initial loss of HF from **2** could form a species that, after loss of CO_2, forms CF_2CH_2 directly, without going through 1,1,1-trifluoroethane.

CO loss can form 2,2,2-trifluoroethanol, CF_3CH_2OH. C_2H_2 could be made by F_2 loss from CHF=CHF, but we found that the F_2 elimination transition state is very high in energy at 6.71 eV. Thus, we expect acetylene also to be made in a bimolecular reaction sequence.

We calculated the MERPs for the formation of the unimolecular reaction products of **2**, Figure 34a. The lowest energy process is the formation of HF (blue), which produces CF_2CH_2 and CO_2. The barrier to CO_2 loss (purple) is competitive with the initial step for CO formation (yellow, shown in Figure S2), but both are higher in energy than HF loss. When the $k(E)$ vs E curves are compared (Figure 34b), HF and CO_2 are the most favourable products at all internal energies. The fact that CO is observed as a significant product suggests an alternative mechanism may be at play in its formation.

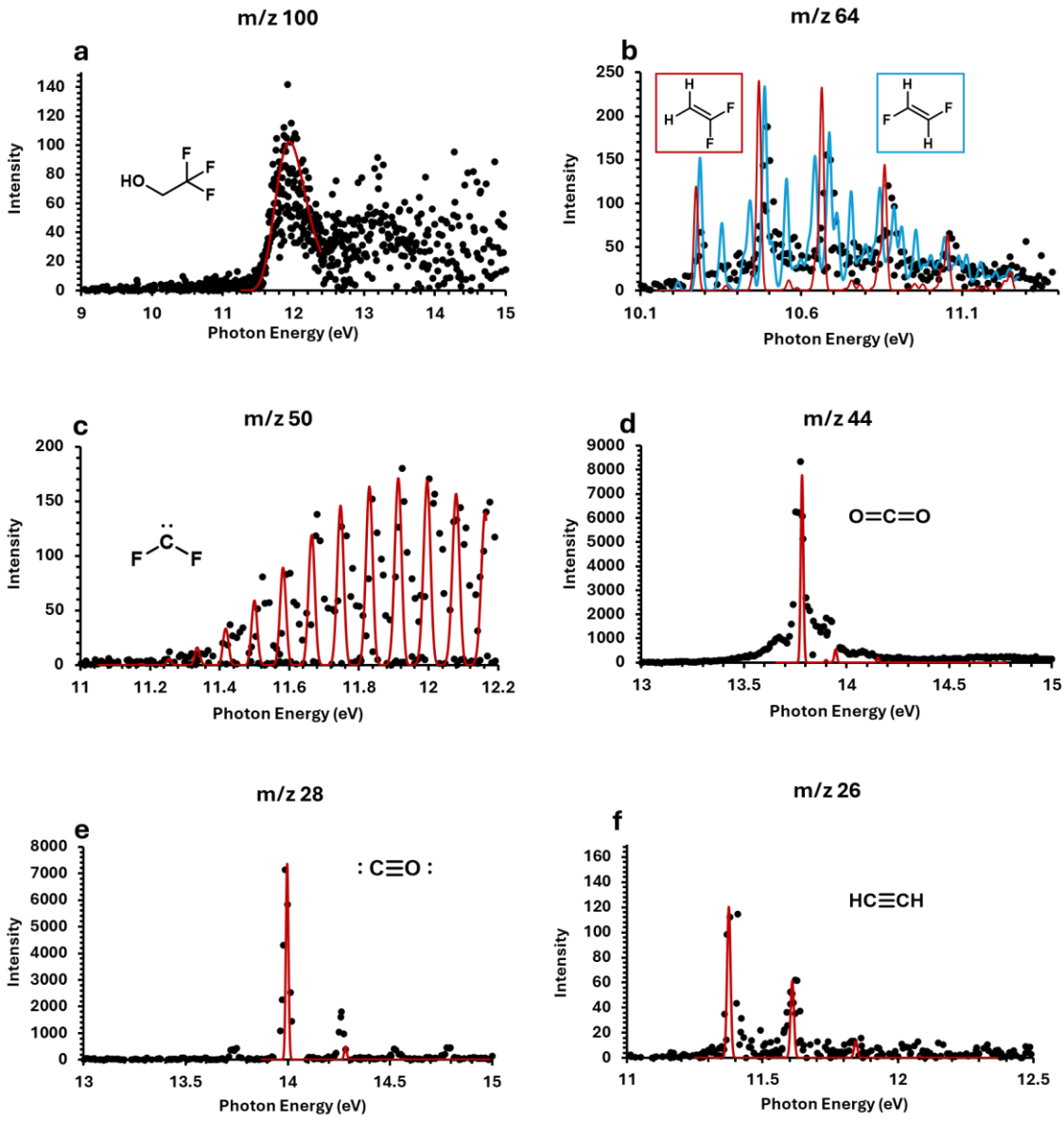

Figure 33: ms-TPES for the pyrolysis products of **2** (symbols) with overlaid Frank-Condon simulations (coloured lines).

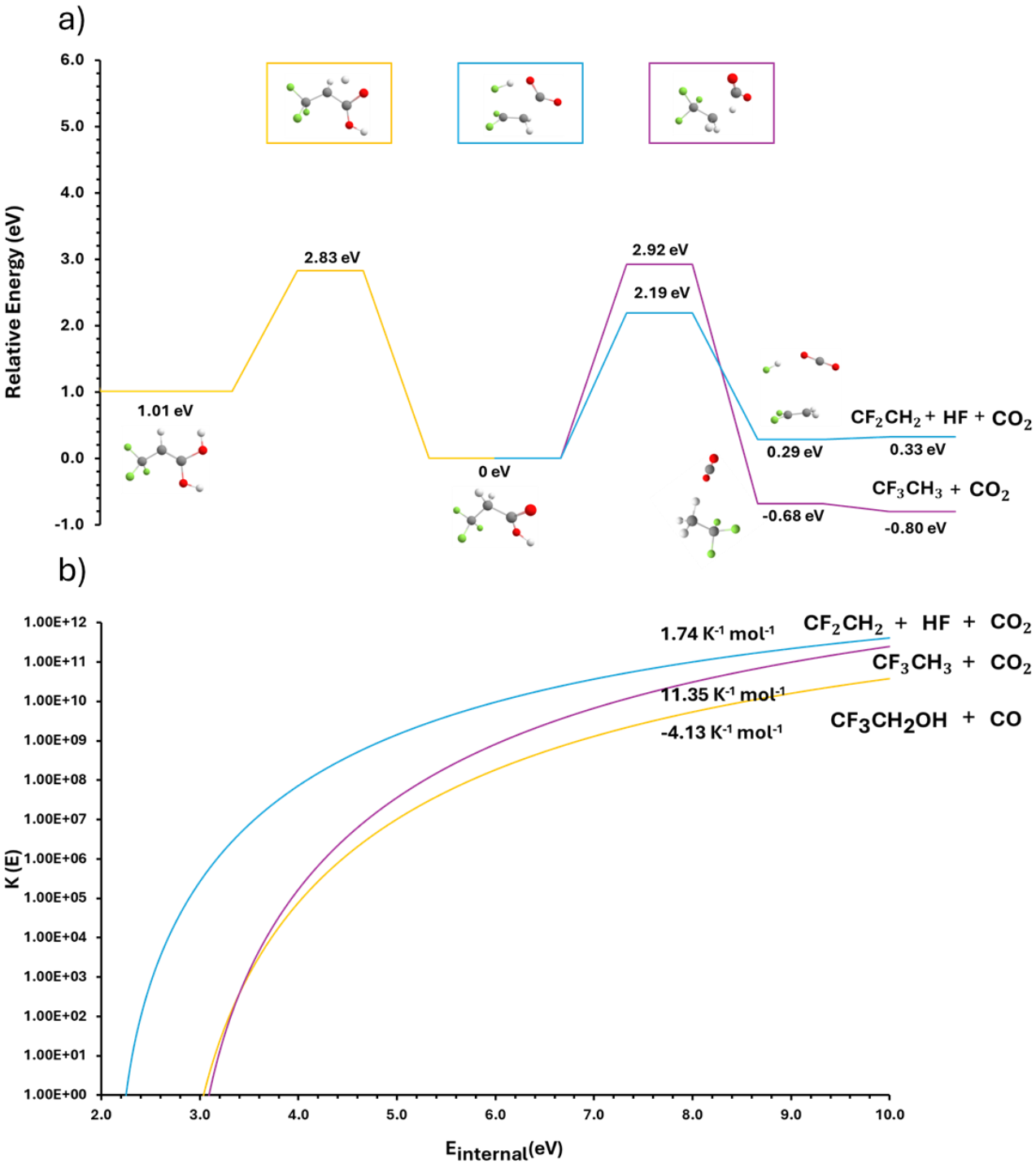

Figure 34*:* a) MERP of **2** showing the formation of 2,2,2-trifluoroethanol, CO_2, CO, HF, and H_2CO, b) RRKM curves for **2** showing the competing reactions forming CO_2, HF, and CO. $\Delta^{\ddagger}S$ values for each reaction are shown.

2,2,3,3,3-Pentafluoro-1-propanol (3)

We identified four ms-TPES from the pyrolysis of **3**, *m/z* 82, 64, 50 and 30, corresponding to CF_2CFH (82 Da),[30] $C_2H_2F_2$ (64 Da),[30] CF_2 (50 Da)[31] and CH_2O (30 Da),[43] Figure 35. The primary dissociation starts with CH_2O loss to form pentafluoroethane (Figure 36), which then proceeds to dissociate at our experimental temperatures to C_2F_4 + HF, followed by C_2F_4 breaking apart to form $2CF_2$.[34] The high energy of the F_2 loss transition state from pentafluoroethane suggests CF_2=CFH and CF_2=CH_2 are formed from bimolecular reactions.

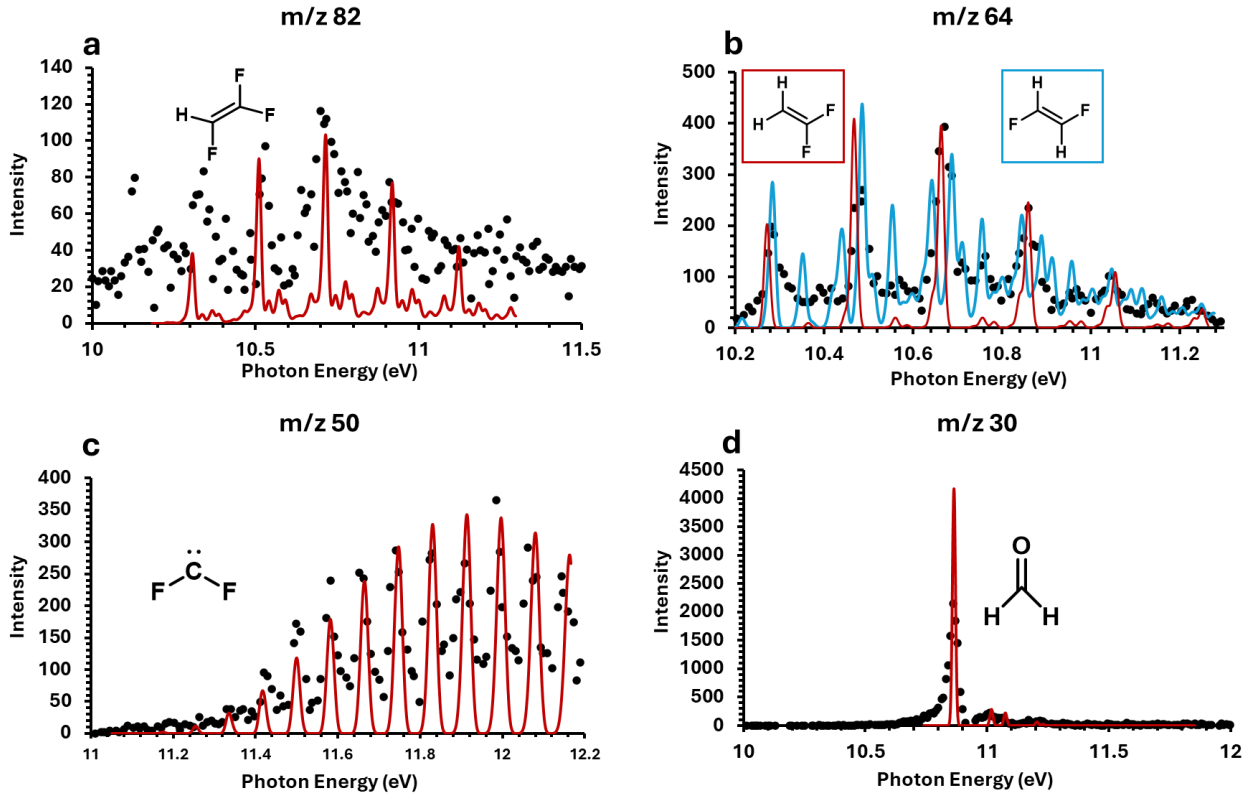

Figure 35: ms-TPES for the pyrolysis products of 3 (black dots) with overlaid Franck-Condon simulations (red).

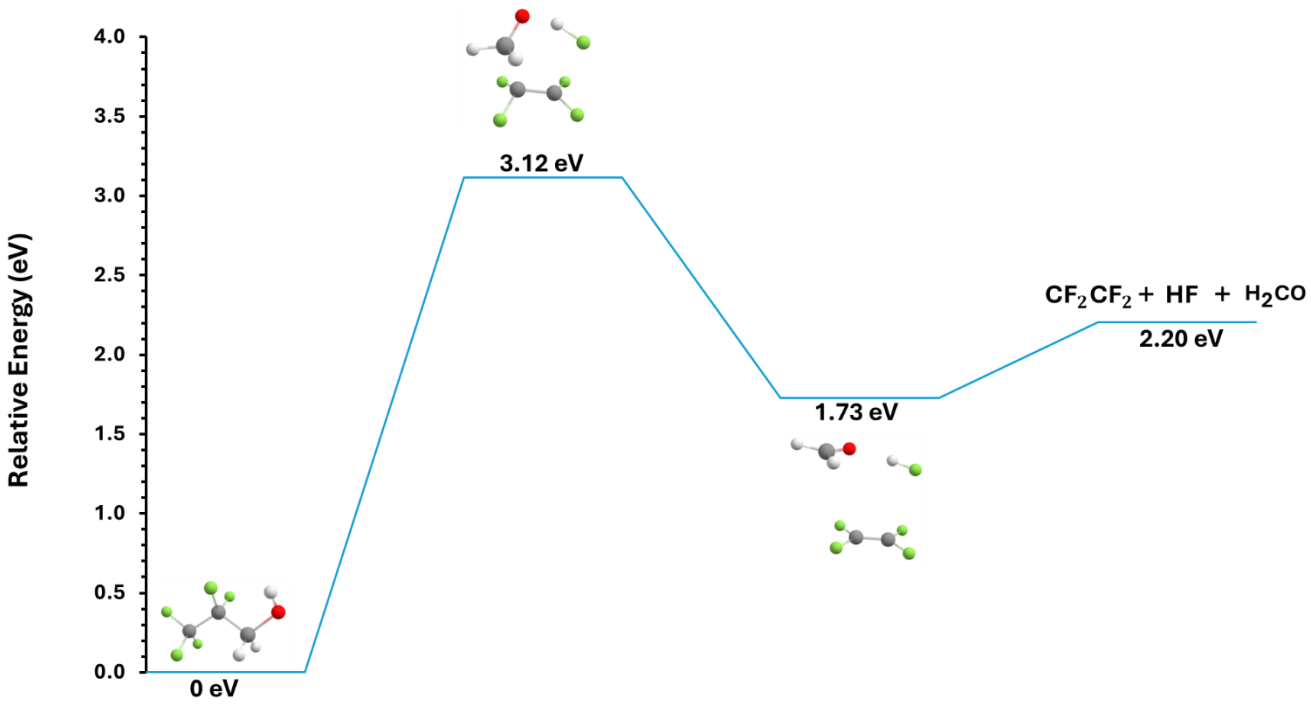

Figure 36: MERP of **3** showing the formation of CH_2O, HF, and CF_2CF_2.

4.6. Conclusion

The pyrolysis of three short-chain PFCs, 2,2,3,3,3-pentafluoropropionic acid (**1**), 3,3,3-trifluoropropionic acid (**2**), and 2,2,3,3,3-pentafluoro-1-propanol (**3**), was explored with photoelectron photoion coincidence spectroscopy and the products were determined by their mass-selected TPES. The two acids preferentially undergo concerted loss of HF and CO_2 to form a fluorinated ethene, which then decomposes to CF_2. Directed CO_2 loss is competitive at high internal energies. Similarly, **3** loses both HF and formaldehyde in a concerted reaction to again form the fluorinated ethene, which goes on to make CF_2.

4.7. References

(1) Leung, S. C. E.; Shukla, P.; Chen, D.; Eftekhari, E.; An, H.; Zare, F.; Ghasemi, N.; Zhang, D.; Nguyen, N.-T.; Li, Q. Emerging Technologies for PFOS/PFOA Degradation and Removal: A Review. *Sci. Total Environ.* **2022**, *827* (153669), 1–34. https://doi.org/10.1016/j.scitotenv.2022.153669.

(2) Paultre, C. B.; Mebel, A. M.; O'Shea, K. E. Computational Study of the Gas-Phase Thermal Degradation of Perfluoroalkyl Carboxylic Acids. *J. Phys. Chem. A* **2022**, *126* (46), 8753–8760. https://doi.org/10.1021/acs.jpca.2c06437.

(3) Blotevogel, J.; Joyce, J. P.; Hill, O. L.; Rappé, A. K. Headgroup Dependence and Kinetic Bottlenecks of Gas-Phase Thermal PFAS Destruction. *ACS ES T Eng.* **2025**, *5* (4), 910–921. https://doi.org/10.1021/acsestengg.4c00726.

(4) Khan, M. Y.; Song, J.; Narimani, M.; da Silva, G. Thermal Decomposition Mechanism and Kinetics of Perfluorooctanoic Acid (PFOA) and Other Perfluorinated Carboxylic Acids : A Theoretical Study. *Environ. Sci. Process. Impacts* **2022**, *24* (12), 2475–2487. https://doi.org/10.1039/d2em00259k.

(5) Altarawneh, M.; Almatarneh, M. H.; Dlugogorski, B. Z. Thermal Decomposition of Perfluorinated Carboxylic Acids: Kinetic Model and Theoretical Requirements for PFAS Incineration. *Chemosphere* **2022**, *286* (131685), 1–15. https://doi.org/10.1016/j.chemosphere.2021.131685.

(6) Alinezhad, A.; Shao, H.; Litvanova, K.; Sun, R.; Kubatova, A.; Zhang, W.; Li, Y.; Xiao, F. Mechanistic Investigations of Thermal Decomposition of Perfluoroalkyl Ether

Carboxylic Acids and Short-Chain Perfluoroalkyl Carboxylic Acids. *Environ. Sci. Technol.* **2023**, *57* (23), 8796–8807. https://doi.org/10.1021/acs.est.3c00294.

(7) Cardona, A. L.; Salas, J.; Lesniak, L.; Mommers, A. A.; Mayer, P. M.; Burgos, M. A. Pyrolysis of Trifluoroacetic Acid and Trifluoroacetic Anhydride Studied with Mass Spectrometry and Synchrotron Radiation : Decomposition and Free Radical Formation. *ChemistrySelect* **2023**, *8* (1), e202202897. https://doi.org/10.1002/slct.202202897.

(8) Bodi, A.; Hemberger, P.; Gerber, T.; Sztáray, B. A New Double Imaging Velocity Focusing Coincidence Experiment: I2PEPICO. *Rev. Sci. Instrum.* **2012**, *83* (083105), 1–8. https://doi.org/10.1063/1.4742769.

(9) Sztáray, B.; Voronova, K.; Torma, K. G.; Covert, K. J.; Bodi, A.; Hemberger, P.; Gerber, T.; Osborn, D. L. CRF-PEPICO: Double Velocity Map Imaging Photoelectron Photoion Coincidence Spectroscopy for Reaction Kinetics Studies. *J. Chem. Phys.* **2017**, *147* (1), 1–10. https://doi.org/10.1063/1.4984304.

(10) Bodi, A.; Hemberge, P.; Pérez-Ramírez, J. Photoionization Reveals Catalytic Mechanisms. *Nat. Catal.* **2022**, *5* (10), 850–851. https://doi.org/10.1038/s41929-022-00847-7.

(11) Hemberger, P.; Custodis, V. B. F.; Bodi, A.; Gerber, T.; Bokhoven, J. A. Van. Understanding the Mechanism of Catalytic Fast Pyrolysis by Unveiling Reactive Intermediates in Heterogeneous Catalysis. *Nat. Commun.* **2017**, *8* (15946), 1–9. https://doi.org/10.1038/ncomms15946.

(12) Sztáray, B.; Baer, T. Suppression of Hot Electrons in Threshold Photoelectron Photoion Coincidence Spectroscopy Using Velocity Focusing Optics. *Rev. Sci. Instrum.* **2003**, *74*

(8), 3763–3768. https://doi.org/10.1063/1.1593788.

(13) Hemberger, P.; Bodi, A.; Bierkandt, T.; Köhler, M.; Kaczmarek, D.; Kasper, T. Photoelectron Photoion Coincidence Spectroscopy Provides Mechanistic Insights in Fuel Synthesis and Conversion. *Energy Fuels* **2021**, *35* (20), 16265–16302. https://doi.org/10.1021/acs.energyfuels.1c01712.

(14) Stephenson, R. M.; Malanowski, S.; Amrose, D. *Handbook of the Thermodynamics of Organic Compounds*; Elsevier Science Publishing: New York, 1987. https://doi.org/10.1007/978-94-009-3173-2.

(15) Guan, Q.; Urness, K. N.; Ormond, T. K.; David, D. E.; Barney Ellison, G.; Daily, J. W. The Properties of a Micro-Reactor for the Study of the Unimolecular Decomposition of Large Molecules. *Int. Rev. Phys. Chem* **2014**, *33* (4), 447–487. https://doi.org/10.1080/0144235X.2014.967951.

(16) Grimm, S.; Baik, S.-J.; Hemberger, P.; Bodi, A.; Kempf, A. M.; Kasper, T.; Atakan, B. Gas-Phase Aluminium Acetylacetonate Decomposition: Revision of the Current Mechanism by VUV Synchrotron Radiation. *Phys. Chem. Chem. Phys* **2021**, *23* (28), 15059–15075. https://doi.org/10.1039/D1CP00720C.

(17) Hemberger, P.; Wu, X.; Pan, Z.; Bodi, A. Continuous Pyrolysis Microreactors: Hot Sources with Little Cooling? New Insights Utilizing Cation Velocity Map Imaging and Threshold Photoelectron Spectroscopy. *J. Phys. Chem. A* **2022**, *126* (14), 2196–2210. https://doi.org/10.1021/acs.jpca.2c00766.

(18) Vasiliou, A. K.; Kim, J. H.; Ormond, T. K.; Piech, K. M.; Urness, K. N.; Scheer, A. M.; Robichaud, D. J.; Mukarakate, C.; Nimlos, M. R.; Daily, J. W.; Guan, Q.; Carstensen, H.-

H.; Ellison, G. B. Biomass Pyrolysis: Thermal Decomposition Mechanisms of Furfural and Benzaldehyde. *J. Chem. Phys.* **2013**, *139* (10), 104310. https://doi.org/10.1063/1.4819788.

(19) Rogers, C. O.; Lockwood, K. S.; Nguyen, Q. L. D.; Labbe, N. J. Diol Isomer Revealed as a Source of Methyl Ketene from Propionic Acid Unimolecular Decomposition. *Int. J. Chem. Kinet.* **2021**, *53* (12), 1272–1284. https://doi.org/10.1002/kin.21532.

(20) Zaleski, D. P.; Sivaramakrishnan, R.; Weller, H. R.; Seifert, N. A.; Bross, D. H.; Ruscic, B.; Moore, K. B.; Elliott, S. N.; Copan, A. V; Harding, L. B.; Klippenstein, S. J.; Field, R. W.; Prozument, K. Substitution Reactions in the Pyrolysis of Acetone Revealed through a Modeling, Experiment, Theory Paradigm. *J. Am. Chem. Soc.* **2021**, *143* (8), 3124–3142. https://doi.org/10.1021/jacs.0c11677.

(21) Lowe, B.; Cardona, A. L.; Salas, J.; Bodi, A.; Paci, M. A. B.; Mayer, P. M. Probing the Pyrolysis of Methyl Formate in the Dilute Gas Phase by Synchrotron Radiation and Theory. *J. Mass Spectrom.* **2022**, *57* (6), e4868. https://doi.org/10.1002/jms.4868.

(22) Lowe, B.; Cardona, A. L.; Bodi, A.; Mayer, P. M.; Paci, M. A. B. The Unimolecular Chemistry of Methyl Chloroformate Ions and Neutrals: A Story of Near-Threshold Decomposition. *J. Am. Soc. Mass Spectrom.* **2023**, *34* (12), 2831–2839. https://doi.org/10.1021/jasms.3c00334.

(23) Li, Y.; Yang, J.; Cheng, Z. *Photonionization Cross Section Database (Version 2.0)*; Yang, J., Team, C., Eds.; China, 2017.

(24) Becke, A. D. Thermochemistry. III. The Role of Exact Exchange. *J. Chem. Phys.* **1993**, *98* (December 1992), 5648–5652. https://doi.org/https://doi.org/10.1063/1.464913.

(25) Lee, C.; Yang, W.; Parr, R. G. Development of the Colic-Salvetti Correlation-Energy Formula into a Functional of the Electron Density. *Phys. Rev. B* **1988**, *37* (2), 785–789. https://doi.org/https://doi.org/10.1103/PhysRevB.37.785?_gl=1*1f4d6wj*_gcl_au*MTI4NDIxMjA4OC4xNzM2Njk3NjU3*_ga*MTQzNjI2MzY0MC4xNzM2Njk3NjU2*_ga_ZS5V2B2DR1*MTczNjcwMzQ3MS4yLjEuMTczNjcwMzk5MS42MC4wLjQ4NzY0MTEwMQ..

(26) Frisch, M. J.; Trucks, G. W.; Schlegel, H. B.; Scuseria, G. E.; Robb, M. A.; Cheeseman, J. R.; Scalmani, G.; Barone, V.; Petersson, G. A.; Nakatsuji, H.; Li, X.; Caricato, M.; Marenich, A. V.; Bloino, J.; Janesko, B. G.; Gomperts, R.; Mennucci, B.; Hratch, D. J. . Gaussian 16. Gaussian Inc.: Wallingford CT 2016.

(27) Baer, T.; Mayer, P. M. Statistical Rice-Ramsperger-Kassel-Marcus Quasiequilibrium Theory Calculations in Mass Spectrometry. *J. Am. Soc. Mass Spectrom.* **1997**, *8* (2), 103–115. https://doi.org/https://doi.org/10.1016/S1044-0305(96)00212-7.

(28) Baer, T.; Hase, W. L. *Unimolecular Reaction Dynamics: Theory and Experiments*; Oxford University Press on Demand: New York, 1996.

(29) Beyer, T.; Swinehart, D. F. Algorithm 448: Number of Multiply-Restricted Partitions. *Commun. ACM* **1973**, *16* (6), 379. https://doi.org/10.1145/362248.362275.

(30) Sell, J. A.; Kuppermann, A. Variable Angle Photoelectron Spectroscopy of the Fluoroethylenes. *J. Chem. Phys.* **1979**, *71* (11), 4703–4715. https://doi.org/10.1063/1.438254.

(31) Innocenti, F.; Eypper, M.; Lee, E. P. F.; Stranges, S.; Mok, D. K. W.; Chau, F. tim; King, G. C.; Dyke, J. M. Difluorocarbene Studied with Threshold Photoelectron Spectroscopy

(TPES): Measurement of the First Adiabatic Ionization Energy (AIE) of CF2. *Chem. - A Eur. J.* **2008**, *14*, 11452–11460. https://doi.org/10.1002/chem.202004513.

(32) West, J. B.; Hayes, M. A.; Siggel, M. R. F.; Dehmer, J. L.; Dehmer, P. M.; Parr, A. C.; Hardis, J. E. Vibrationally Resolved Photoelectron Angular Distributions and Branching Ratios for the Carbon Dioxide Molecule in the Wavelength Region 685-795 Å. *J. Chem. Phys.* **1996**, *104* (11), 3923–3934. https://doi.org/10.1063/1.471249.

(33) Zhou, W.; Seccombe, D. P.; Tuckett, R. P.; Thomas, M. K. Fragmentation of Valence Electronic States of CHF2CF3 + Studied by Threshold Photoelectron – Photoion Coincidence (TPEPICO) Techniques in the Photon Energy Range 12 – 25 EV. *Chem. P* **2002**, *283* (3), 419–431. https://doi.org/10.1016/S0301-0104(02)00790-5.

(34) Copeland, G.; Lee, E. P. F.; Dyke, J. M.; Chow, W. K.; Mok, D. K. W.; Chau, J. F. T. Study of Pentafluoroethane and Its Thermal Decomposition Using UV Photoelectron Spectroscopy and Ab Initio Molecular Orbital Calculations. *J. Phys. Chem. A* **2010**, *114* (10), 3540–3550. https://doi.org/10.1021/jp1000607.

(365) Takahashi, K.; Harada, A.; Horigome, S.; Cho, R.; Inomata, T. Thermal Decompositons of 1,1,1-Trifluoroethane and Pentafluoroethane in a Turbulent Flow Reactor. *Combust. Sci. Technol.* **2007**, *179*, 1417–1432. https://doi.org/10.1080/00102200601181962.

(36) Koppel, I.A.; Molder, U.H.; Pikver, R. J. Photoelectron Spectra of Molecules. I. Alcohols. **1983**, *20* (45).

(37) Dareah Thomas, T. X-Ray Photoelectron Spectroscopy of Carbon Monoxide. *J. Chem. Phys.* **1970**, *53* (5), 1744–1749. https://doi.org/10.1063/1.1674252.

(38) Razmus, W. O.; Prlj, A.; Seifert, N. A.; Bonanomi, M.; Callegari, C.; Danailov, M.; Decleva, P.; Demidovich, A.; De Ninno, G.; Devetta, M.; Faccialà, D.; Feifel, R.; Giannessi, L.; Piteša, T.; Powis, I.; Raimondi, L.; Reid, K. L.; Ribič, P. R.; Spezzani, C.; Squibb, R. J.; Thompson, J. O. F.; Plekan, O.; Vozzi, C.; Warne, E. M.; Zangrando, M.; Prince, K. C.; Di Fraia, M.; Holland, D. M. P.; Minns, R. S.; Došlić, N.; Pratt, S. T. Time-Resolved Vacuum-Ultraviolet Photoelectron Spectroscopy of the A˜ 1Au State of Acetylene. *J. Chem. Phys.* **2025**, *162* (5), 054310. https://doi.org/10.1063/5.0241392.

(39) Sauvageau, P.; Doucet, J.; Gilbert, R.; Sandorfy, C. Vacuum Ultraviolet and Photoelectron Spectra of Fluoroethanes. *J. Chem. Phys.* **1974**, *61* (1), 391–395. https://doi.org/10.1063/1.1681649.

(40) Zhou, W.; Collins, D. .; Chim, R. Y. .; Seccombe, D. P.; Tuckett, R. . Threshold Photoelectron Photoion Coincidence Study of the Fragmentation of Valence States of CF3–CH3+ and CHF2–CH2F+ in the Range 12–24 EV. *Phys. Chem. Chem. Phys* **2004**, *6*, 3081–3091. https://doi.org/10.1039/B404604H.

(41) Takahashi, K.; Harada, A.; Horigome, S.; Cho, R.; Inomata, T. Thermal Decompositons of 1 , 1 , 1-Trifluoroethane and Pentafluoroethane in a Turbulent Flow Reactor. **2007**, No. 16560194, 1417–1432. https://doi.org/10.1080/00102200601181962.

(42) Locht, R.; Leyh, B.; Hoxha, A.; Dehareng, D.; Jochims, H. W.; Baumgärtel, H. About the Vacuum UV Photoabsorption Spectrum of Methyl Fluoride (CH3F): The Fine Structure and Its Vibrational Analysis. *Chem. Phys.* **2000**, *257* (2–3), 283–299. https://doi.org/10.1016/S0301-0104(00)00167-1.

(43) Keller, P. R.; Taylor, J. W.; Grimm, F. A.; Carlson, T. A. Angle-Resolved Photoelectron

Spectroscopy of Formaldehyde and Methanol. *Chem. Phys.* **1984**, *90* (1–2), 147–153. https://doi.org/10.1016/0301-0104(84)85090-9.

4.8. Supplementary Information

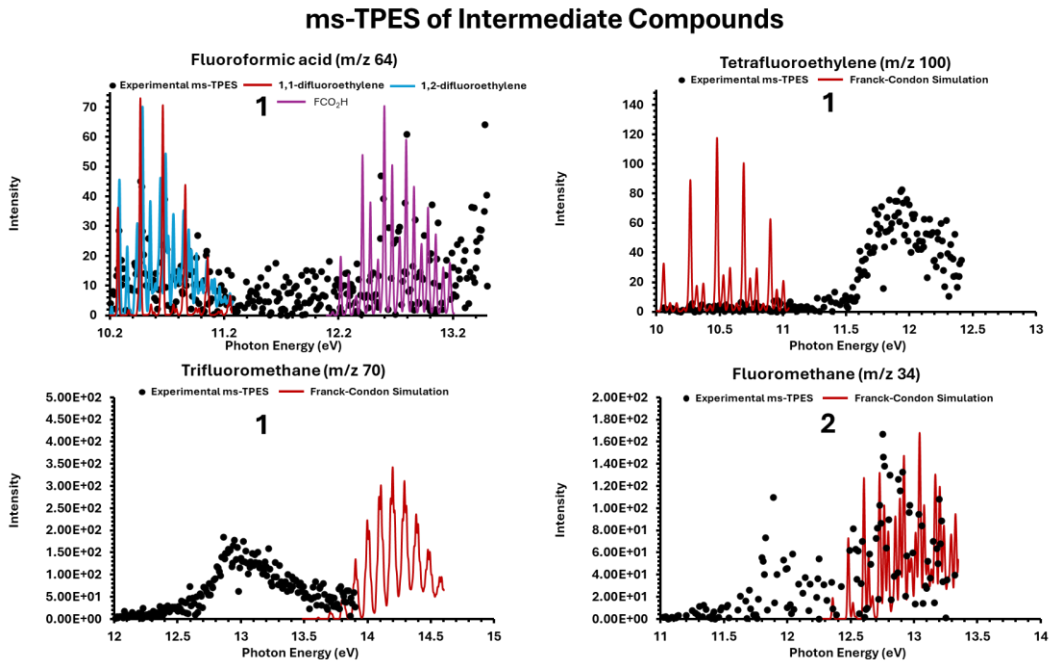

Figure S 1: ms-TPES for m/z 64, 100, 70 and 34, together with FC-simulations for fluoroformic acid, tetrafluoroethylene, trifluoromethane, fluoromethane.

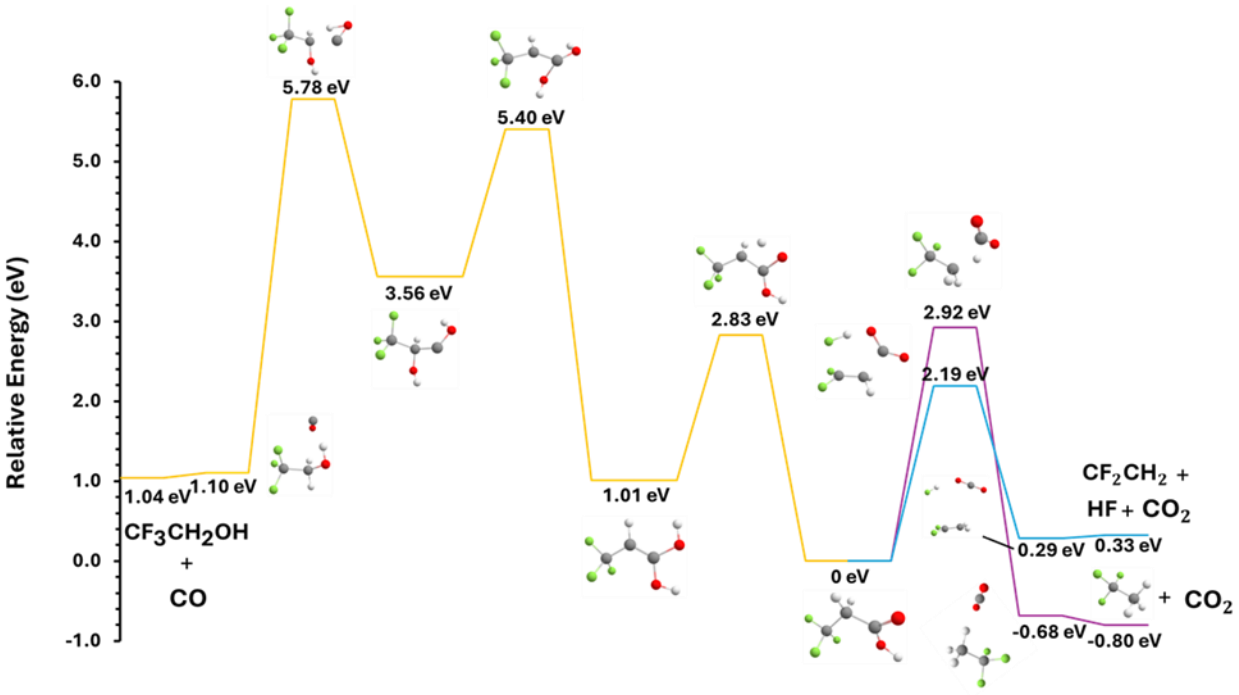

Figure S 2: MERP of **2** showing the formation of CO, CF_3CH_2OH, CO_2, HF, and CF_2CH_2.

Table S 1: Literature and experimental ionization energies of all compounds and their observed products.

Molecule	Literature Ionization Energy (eV)	CBS-QB3 Ionization Energy (eV)
$CF_3CF_2CO_2H$[a]	11.60	11.06
CF_2CH_2[b]	10.29	10.07
CFHCFH[b]	10.21	9.87
CF_2[c]	11.42	11.28
CO_2[d]	13.78	13.68
H_2CO[d]	10.88	10.70
CF_3CF	N.A.	10.28
FCO_2H	N.A.	11.82
$CF_3CH_2CO_2H$[a]	11.12	10.59
CF_3CH_2OH[e]	11.49	10.75
CO[d]	14.10	14.14
C_2H_2[d]	11.40	11.22
CF_3H[f]	13.90	13.37
CF_3CH_3[g]	13.30	12.14
CF_3CF_2H	N.A.	11.74
$CF_3CF_2CH_2OH$[a]	11.10	10.52
CF_2CFH[b]	10.14	9.84
CFH_2CO_2H	N.A.	10.64
C_2F_4[b]	10.14	9.80
CFH_3[d]	12.45	12.19
HF[b]	16.06	15.80
CF_2CFCO_2	N.A.	11.04

(a) Mayer, P. et al. *Can. J. Chem.* **2026**, https://doi.org/10.1139/cjc-2025-0242.

(b) Bieri, G. et al. *Chem. Phys.* **1981**, *60* (1), 61–79.

(c) Dyke, J.M. et al. *J. Chem. Soc. Faraday Trans. 2* **1974**, *70*, 1828–1836.

(d) Kimura, K. et al. Japan Scientific Soc. Press: Tokyo, 1981.

(e) Koppel, I.A et al. *Org. React. Tartu* **1983**, *20*, 45.

(f) Novak, I. et al. *J. Phys. B* **1985**, *18* (8), 1581.

(g) Simmie, J.M. et al. *Int. J. Mass Spectrom. Ion Phys.* **1971**, *7* (1), 41–45.

Table S 2: Estimated branching ratios (%) for the observed products based on referenced photoionization cross-sections.

	CO_2 [a]	CO[b]	CH_2O[c]	CF_2 [d]	$C_2H_2F_2$ [e]	C_2H_2 [f]	CF_3CH_2OH [g]	C_2F_3H [e]
1	70			3	7			
2	40	41		0.4	5	0.6	11	
3			56	4	26			14

[a] A. P. Hitchcock, et al., Chem. Phys. 1980, 45 (3), 461-478.

[b] G. R. Wight, et al., J. Phys. B 1976, 9 (4), 675-689

[c] G. Cooper, et al., Chem. Phys. 1996, 209 (1), 61-77.

[d] A S Santos et al 2009 J. Phys.: Conf. Ser. 194 022078

[e] assumed to be the same as C_2H_4 : D. M. P. Holland, et al., Chem. Phys. 1997, 219 (1), 91-116.

[f] J. C. Person, et al., J. Chem. Phys. 1970, 53 (5), 1767-1774.

[g] Estimated PICS of 0.5 Mb

Conclusions

PFAS were designed specifically for use in products due to their unique properties, but unfortunately, these same properties make them resistant to degradation and persistent in the environment. PFAS have also been shown to be toxic and harmful to humans and animals, and are present in different environmental matrices.

There are many studies aimed at extracting PFAS from environmental matrices and analyzing them using chromatography combined with mass spectrometry. One research paper used high-resolution mass spectrometry to discover new PFAS using a variety of identification methods, such as mass defect, homologous series, and characteristic fragmentation patterns.[1] With the emergence of new short-chain PFAS, our CID results will help researchers to better identify them with our fragmentation results.

There have also been many techniques tested for removing PFAS, but most of the feasible ones don't completely remove PFAS. It has been recently reported that organic waste that has been contaminated with PFAS usually undergoes incineration or is sent to the landfill, but this results in PFAS being released. More research is now being done to remove PFAS from waste, such as using dry pyrolysis. This method resulted in greater than about 97% removal, but residual PFAS were left in the waste, including short chain PFAS byproducts and even long-chain PFAS.[2] I believe my research can fill in the gap and demonstrate the products being produced from pyrolysis, and aid researchers in identifying if these products should be further researched to determine their toxicity and persistence.

In this research, five short-chain PFAS were studied to determine their breakdown products using CID triple quadrupole mass spectrometry and pyrolysis. In the CID MS study, it was found that

four oxygenated PFAS anions **1**-**4** exhibited the reactions of CO_2, HF, and CH_2O loss. There was qualitative agreement between the observed E_{com} onset energies for fragmentation of the ions and the corresponding calculated energy requirements. For the acids, increasing hydrogen content increased the number of competing reactions beyond simple CO_2 loss. This was also true for the alcohols, with the pentafluorinated **3** primarily losing formaldehyde, whereas the trifluorinated **4** exhibited two major dissociation channels, producing HF and water. Thus, it may be possible to gain insight into thermal degradation processes and products of PFAS by examining the tandem mass spectra of the corresponding anions.

The pyrolysis of three short-chain PFCs, 2,2,3,3,3-pentafluoropropionic acid (**1**), 3,3,3-trifluoropropionic acid (**2**), and 2,2,3,3,3-pentafluoro-1-propanol (**3**), was explored using iPEPICO and the products were determined by their mass-selected TPES. The two acids initially decompose by CO_2 loss to form a halogenated ethane, which can then go on to form fluorinated ethenes and ultimately CF_2 in sequential reactions.. **3** initially loses formaldehyde to form the trifluoroethane. All three compounds also lose HF in these processes as well to make fluorinated ethenes and CO_2. So, it was found that incomplete degradation occurred with these shorter chain PFAS, and the C-F bond remained.

Overall, similar degradation products were observed in the ion and neutral chemistry. For example, CO_2, HF, CH_2O, FCO_2, and ethenes. In both cases, though, the CF bond persisted, which highlights its resistance to degradation. Therefore, more research is needed to determine a way to effectively remove PFAS from the environment while also destroying them completely.

References

(1) Strynar, M.; Mccord, J.; Newton, S.; Washington, J.; Barzen-hanson, K.; Trier, X.; Liu, Y.; Dimzon, I. K.; Bugsel, B.; Zwiener, C.; Munoz, G. Practical Application Guide for the Discovery of Novel PFAS in Environmental Samples Using High Resolution Mass Spectrometry. *J. Expo. Environ. Epidemiol.* **2023**, *33*, 578–588. https://doi.org/10.1038/s41370-023-00578-2.

(2) Sørmo, E.; Castro, G.; Hubert, M.; Licul-Kucera, V.; Quintanilla, M.; Asimakopoulos, A. G.; Cornelissen, G.; Arp, H. P. H. The Decomposition and Emission Factors of a Wide Range of PFAS in Diverse, Contaminated Organic Waste Fractions Undergoing Dry Pyrolysis. *J. Hazard. Mater.* **2023**, *454*, 131447. https://doi.org/10.1016/j.jhazmat.2023.131447.